JAEA-Review
2008-004

JAEA-Review

Progress Report Neutron Science

(April 1, 2006 - March 31, 2007)

Quantum Beam Science Directorate
Advanced Science Research Center

March 2008

Japan Atomic Energy Agency

日本原子力研究開発機構

本レポートは日本原子力研究開発機構が不定期に発行する成果報告書です。
本レポートの入手並びに著作権利用に関するお問い合わせは、下記あてにお問い合わせ下さい。
なお、本レポートの全文は日本原子力研究開発機構ホームページ（http://www.jaea.go.jp/index.shtml）より発信されています。このほか財団法人原子力弘済会資料センター*では実費による複写頒布を行っております。

〒319-1195　茨城県那珂郡東海村白方白根 2 番地 4
日本原子力研究開発機構　研究技術情報部　研究技術情報課
電話 029-282-6387, Fax 029-282-5920

*〒319-1195　茨城県那珂郡東海村白方白根 2 番地 4　日本原子力研究開発機構内

This report is issued irregularly by Japan Atomic Energy Agency
Inquiries about availability and/or copyright of this report should be addressed to
Intellectual Resources Section, Intellectual Resources Department,
Japan Atomic Energy Agency
2-4 Shirakata Shirane, Tokai-mura, Naka-gun, Ibaraki-ken 319-1195 Japan
Tel +81-29-282-6387, Fax　+81-29-282-5920

© Japan Atomic Energy Agency, 2008

JAEA-Review 2008-004

Progress Report on Neutron Science
(April 1, 2006 - March 31, 2007)

Quantum Beam Science Directorate [+1~+3]
and
Advanced Science Research Center [*1~*2]

Japan Atomic Energy Agency
Tokai-mura, Naka-gun, Ibaraki-ken

(Received January 11, 2008)

There are 13 research groups in neutron science and technology in the Quantum Beam Science Directorate (QuBS) and Advanced Science Research Center (ASRC) of Japan Atomic Research Agency (JAEA). A wide variety of research is performed by these group: neutron scattering (condensed matter physics, polymer science, biology, and residual stress analysis), prompt gamma-ray analysis, neutron radiography, neutron optics, and development of a neutron spectrometer, neutron beam handling device and neutron detector. This issue summarizes research progress in neutron science and technology including activities of the Nuclear Science and Engineering Directorate of JAEA, and of the COMMON USE PROGRAM of JAEA utilizing the research reactor JRR-3 during the period between April 1, 2006 and March 31, 2007. This report contains highlights of research by these 13 neutron research groups of QuBS and ASRC, introducing 68 experimental reports.

Keywords: Neutron Science, Neutron Technology, JRR-3

(Eds.) Masayasu TAKEDA[+1], Takashi OHHARA[+2], and Atsushi MORIAI[+3]
Quantum Beam Science Directorate Neutron
+1: Neutron Materials Research Center
+2: Neutron Biology Research Center
+3: Neutron Technology R & D Center

*1: Information Transmittance among Hierarchical Structures in Strong Correlated Supramolecular Systems Group
*2: Spin-Orbital Complex Dynamics of f-electron Many-body Systems Group

JAEA-Review　2008-004

中性子科学研究成果報告集
（2006年度年次報告）

日本原子力研究開発機構
量子ビーム応用研究部門[+1～+3]
先端基礎研究センター[*1～*2]

（2008年 1月 11日 受理）

日本原子力研究開発機構には、量子ビーム応用研究部門および先端基礎研究センター、合わせて13の中性子科学関連グループがあり、研究用原子炉JRR-3を利用した研究を行っている。分野は中性子散乱（固体物性、高分子、生物、残留応力）、即発ガンマ線分析、中性子ラジオグラフィ、中性子光学、装置・検出器・デバイス開発と多岐にわたる。

本報告書は、これらのグループの活動報告に加え、2006年4月から2007年3月までの期間に、日本原子力研究開発機構の独自枠による中性子科学研究、機構外との共同研究、JRR-3の施設供用利用で得られた成果として68編の研究報告を収録する。

〒319-1195　茨城県那珂郡東海村白方白根2-4

編集者：武田　全康[+1]・大原　高志[+2]・盛合　敦[+3]
量子ビーム応用研究部門（中性子ユニット）
+1: 中性子物質科学研究ユニット
+2: 中性子生命科学研究ユニット
+3: 中性子産業利用技術研究ユニット

先端基礎研究センター
*1: 強相関超分子系の構築と階層間情報伝達機構の解明グループ
*2: f電子多体系のスピン・軌道複合ダイナミックスの解明グループ

Contents

Neutron Science Relations in JAEA 1
List of JAEA Instruments 3

1.Highlights in Research at JAEA 5

1.1 X-ray and Neutron Crystallography for Structure Determination of Biological Macromolecules 7
Molecular Structural Biology Group R. Kuroki

1.2 DNA Deformability and Hydration Studied by Molecular Dynamics Simulation 8
Computational Biology Group H. Kono

1.3 Protein Dynamics Studied by Neutron Scattering 9
Neutron Biophysics Group M. Kataoka

1.4 Investigation of Condensed Matter Magnetism by Polarized Neutron Scattering 10
Polarized Neutron Magnetism Group K. Kakurai

1.5 Functional Materials Studied by Neutron Diffraction 11
Nanomaterials Synthesis Group S. Shamoto

1.6 Neutron Scattering Studies on Advanced Energy-Related Materials 12
Advanced Materials for Energy Group K. Kakurai

1.7 Diverse Studies on Neutron Imaging 13
Neutron Imaging and Activation Analysis M. Matsubayashi

1.8 Residual Stress Analysis and Advanced Research in Materials Science 14
Neutron Residual Stress Analysis Group K. Akita

1.9 Development and Construction of Pulsed-Neutron Scattering Instruments for J-PARC 15
Pulsed Neutron Instrumentation Group M. Arai

1.10 Development of Neutron Detectors and Neutron Optical Devices 16
Neutron Detectors and Optical Devices R&D Group K. Soyama

1.11 Development and Application of Neutron Optics 17
Neutron Optics Group J. Suzuki

1.12 Investigation of Hierarchical Structures by Ultra-Small-Angle Neutron Scattering: a Bridge between Material Science and Life Science 18
Information Transmittance among Hierarchical Structures in Strong Correlated Supramolecular Systems Group
S. Koizumi and T. Hashimoto

1.13 Precise Single Crystal Neutron Diffraction Investigation on *Rattling* in Cage Compounds 19
Spin-Orbital Complex Dynamics of f-electron Many-body Systems Group
K. Kaneko

2.Research Reports 21

2.1 Biology 21
Structure and Mechanism

2.1.1 Defect Study of Protein Crystals by Neutron Topography 23
H. Koizumi, N. Ohya, M. Koishi, N. Kitajima, Y. Mukohbayashi, M. Tachibana, K. Kojima, K. Kurihara and R. Kuroki

2.1.2 A Neutron Crystallographic Analysis of 2Zn-Insulin 24
W. Iwai, T. Yamada, Y. Ohnishi, Y. Kobayashi, I. Tanaka, K. Kurihara, R. Kuroki and N. Niimura

2.1.3 The State of Cryptobiosis of Larvae of *Polypedilum Vandezplanki* Studied by Incoherent Inelastic Neutron Scattering 25
H. Nakagawa, T. Okuda, Y. Joti and M. Kataoka

2.1.4 Hydration Water Dynamics at Protein Dynamical Transition by Quasi-Elastic Neutron Scattering 26
H. Nakagawa and M. Kataoka

2.1.5 Neutron Diffraction Study of Porcine Pancreatic Elastase with Its Inhibitor 27
T. Kinoshita, T. Tamada, T. Ohhara, K. Kurihara, T. Tada and R. Kuroki

2.1.6 Single Crystal Neutron Structure Analysis of a [NiFe]hydrogenase Model Complex 28
S. Ogo, R. Kabe, K. Uehara, B. Kure, T. Nishimura, S. C. Menon, R. Harada, S. Fukuzumi, Y. Higuchi, T. Ohhara, T. Tamada and R. Kuroki

2.1.7 Contrast Variation Measurements of Hen Egg White Lysozyme Amyloid Protofilaments 29
S. Fujiwara, F. Matsumoto and H. Nakagawa

2.1.8 Hierarchical Structure for Red Blood Cells Observed by Small-Angle Neutron Scattering with Solvent Contrast Variation 30
H. Iwase and S. Koizumi

2.1.9 The Structure of 4-Repeat Tau and 3-Repeat Tau Monomer and their Self-Assembled Clusters 31
S. Naito, H. Mochizuki, T. Yasuda, Y. Mizuno, M. Furusaka, S. Ikeda, M. H. Shimizu, J. Suzuki and S. Fujiwara

2.2 Soft Matter 33
Polymer Glasses, Gel and Phase Separation

2.2.1 *In-situ* and *Real-time* Observation of Simultaneous Living Anionic Copolymerization Process and Polymerization-Induced Self-Assembly by SANS, UV-vis, GPC and NMR 35
Y. Zhao, N. Miyamoto, S. Koizumi and T. Hashimoto

2.2.2 *In Situ* Observation of the Formation of Actin and Polycation Complexes ... 36

T. Masui, K. Shikinaka, H. J. Kwon, S. Koizumi, T. Hashimoto, H. Iwase, A. Kakugo and J. P. Gong

2.2.3 Wide-q Observation of the Self-Assembled Fractal Porous Silica by Ultra-small-angle Neutron Scattering ... 37

D. Yamaguchi, H. Mayama, S. Koizumi, K. Tsujii and T. Hashimoto

2.3 Strongly Correlated Electron Systems and Superconductivity ... 39
U-compounds, Ce-compounds and Transition-metal Oxides

2.3.1 Polarized Neutron Inelastic Scattering Study of Spin Fluctuation in $La_{2-x}(Sr,Ba)_xCuO_4$ ... 41

S. Wakimoto, K. Kakurai, M. Takeda, M. Matsuda, M. Fujita, K. Yamada and J.M. Tranquada

2.3.2 Successive Phase Transitions of $LuBaCo_4O_7$ with Kagome and Triangular Lattices ... 42

M. Soda, T. Moyoshi, Y. Yasui, M. Sato and K. Kakurai

2.3.3 Magnetic Excitations in Lightly-Doped $La_{2-x}Sr_xCuO_4$ ... 43

M. Matsuda, S. Wakimoto, M. Fujita, K. Yamada and J. M. Tranquada

2.3.4 New-Type Phase Transition of Honeycomb Lattice System Li_2RuO_3 ... 44

Y. Miura, Y. Yasui, M. Sato, N. Igawa and K. Kakurai

2.3.5 Direct Observation of the Pressure-Induced Ferromagnetic Order in Valence Transition Material $YbInCu_4$ ... 45

T. Osakabe, K. Kojima and K. Hiraoka

2.3.6 Magnetic Structure of $TbRhIn_5$ ... 46

T. Sugai, F. Mizuno, N. Metoki, Y. Haga, N. V. Hieu, T.Takeuchi, K. Sugiyama, R.Settai and Y. Onuki

2.3.7 Magnetic Structure of $TbMnO_3$ Studied with Spherical Neutron Polarimetry ... 47

R. Kajimoto, M. Matsuda, M. Takeda, K. Kakurai, Y. Mitsui, H. Yoshizawa, T. Kimura and Y. Tokura

2.3.8 Unusual Magnetic Structure and the Successive Transition in $NpFeGa_5$ ... 48

N. Metoki, F. Honda, S. Jonen, K. Kaneko, T. Sugai, F. Mizuno, G. H. Lander, D. Aoki, Y. Homma and Y. Shiokawa

2.3.9 Coulomb Interaction in $NpCoGa_5$ Probing through Phonon Spectroscopy ... 49

K. Kaneko, N. Metoki, S. Raymond, J.-P. Sanchez, P. Piekarz, K. Parlinski, A. M. Oleś, D. Aoki, Y. Homma, Y. Shiokawa, S. Ikeda, T. D. Matsuda, Y. Haga, Y. Ōnuki and G. H. Lander

2.4 Magnetism and Low Temperature Physics ... 51
Low Dimension, Frustration, Magnetic Transitions and Quantum Liquids

2.4.1 Magnetic Excitation in the Spin-1/2 Trimer Chain Compound $Cu_3(P_2O_6OD)_2$ 53
M. Hase, M. Matsuda, K. Kakurai, K. Ozawa, H. Kitazawa, N. Tsujii, A. Dönni, M. Kohno and X. Hu

2.4.2 Polarized Neutron Inelastic Scattering Study of Central Mode in $TlCoCl_3$ 54
A. Oosawa, K. Kakurai, Y. Nishiwaki and T. Kato

2.4.3 Softening of Magnetic Excitations Leading to Pressure-Induced Quantum Phase Transition in Gapped Spin System $KCuCl_3$ 55
K. Goto, T. Osakabe, K. Kakurai, Y. Uwatoko, A. Oosawa and H. Tanaka

2.4.4 Neutron Elastic Scattering in Quantum Spin System NH_4CuCl_3 56
T. Ono, K. Goto, Y. Kubota, H. Tanaka, N. Metoki, F. Honda and K. Kakurai

2.4.5 Magnetic Structure of $Co_2TeO_3Cl_2$ 57
T. Kashi, Y. Yasui, T. Moyoshi, M. Sato, N. Igawa and K. Kakurai

2.4.6 Spherical Polarization Analysis of Artificially Confined Spin-Density Waves in Cr/Sn Multilayers 58
M. Takeda, M. Nakamura, K. Kakurai, K. Mibu and E. Lelièvre-Berna

2.4.7 Magnetic Microstructure of $LaMnO_{3+\delta}$ Nanocrystals in Mesoporous Silica 59
H. Kira, H. Tamura, Y. Murakami, T. Shinohara and J. Suzuki

2.4.8 Neutron Scattering Study of Metamagnetic Phase Transition in $HoRhIn_5$ Compounds 60
N.V. Hieu, S. Jonen, T. Takeuchi, K. Sugiyama, R. Settai, Y. Ōnuki, T.D. Matsuda, Y. Haga and N. Metoki

2.4.9 Measurements of the Magnetic form Fators of α-Fe and CoFe Powder by Polarized Neutron Deffractometry 61
S. Oitani, Y. Ishii, M. Takeda, K. Kakurai, Y. Sasaki, M. Kishimoto and Y. Nishihara

2.4.10 Magnetic-field Induced Magnetic Phase Transitions in Multiferroic Compound of $ErMn_2O_5$ 62
H. Kimura, S. Wakimoto, Y. Noda, K. Kaneko, N. Metoki, K. Kakurai and K. Kohn

2.4.11 Temperature and Electric Field Dependences of Spin Chirality in Multiferroic Compound of $HoMn_2O_5$ 63
H. Kimura, S. Wakimoto, K. Nishihata, Y. Noda, M. Takeda, K. Kakurai and K. Kohn

2.4.12 Small Angle Neutron Scattering Study of Interface Nanostructure in Sintered Nd-Fe-B Magnets Processed Under High Magnetic Fields 64
T. Akiya, H. Kato, M. Takeda, J. Suzuki, D. Yamaguchi, S. Koizumi, M. Sagawa and K. Koyama

2.4.13 Magnetic Structure and Phase Diagram of $NpIn_3$ Studied by Neutron Scattering under Magnetic Field 65
F. Mizuno, T. Sugai, N. Metoki, Y. Haga, D. Aoki, Y. Homma and Y. Siokawa

2.4.14 Magnetic Ordering Process in the Layered Triangular Lattice System $LuFe_2O_4$ in Applied Field 66
K. Kakurai, M. Matsuda, K. Yoshii, N. Ikeda, Y. Ishii, H. Kito and Y. Yamada

2.5 Structural Physics 67
Ionic Conductivity, Phase Transition and Dynamics

2.5.1 Crystal Structure Analysis of $LiGa_5O_8$ by Neutron Powder Diffraction 69
H. Yamauchi, T. Suzuki and Y. Ohishi

2.5.2 Neutron Diffraction Study on Successive Structural Phase Transitions of $TlCoCl_3$ 70
Y. Nishiwaki, A. Oosawa, K. Kakurai and T. Kato

2.5.3 Location of Deuterium Atoms in $BaSn_{0.5}In_{0.5}O_{2.75}$ by Neutron Powder Diffraction at 77-473 K 71
T. Nagasaki, T. Ito, K. Iwasaki, M. Yoshino, N. Igawa and Y. Ishii

2.5.4 Observation of CO_2 Molecule in Clathrate Hydrate by Maximum Entropy Method 72
N. Igawa, T. Taguchi, H. Fukazawa, H. Yamauchi and Y. Ishii

2.5.5 Neutron Study Suggests Ferroelectric Ice in the Universe 73
H. Fukazawa, H. Yamauchi, N. Igawa and Y. Ishii

2.6 Materials Science and Industrial Applications 75
Microstructure and Residual Stress

2.6.1 Analysis of Crystal $LiMn_2O_4$ Size in Composite Sample by Neutron Scattering 77
K. Basar, Xianglian, S. Siagian, K. Ohara, T. Sakuma, H. Takahashi, O. Abe, N. Igawa and Y. Ishii

2.6.2 Magnetic Structures in $Mn_3Cu_{1-x}Ge_xN$: Evidence for the Close Relationship with Magneto-volume Effect 78
S. Iikubo, K. Kodama, K. Takenaka, H. Takagi and S. Shamoto

2.6.3 Standardization of Residual Stress Measurement Method of Weld Section 79
T. Kurimura, S. Okido and H. Suzuki

2.6.4 Ferroelectric Phonon Mode in Relaxor $K_{1-x}Li_xTaO_3$ 80
S. Wakimoto, G. A. Samara, R. K. Grubbs, E. L. Venturini, L. A. Boatner, G. Xu and G. Shirane

2.6.5 Intergranular Strain Pole Figure Measurement for ECAPed Al by Neutron Diffraction 81
T. Suzuki, T. Ishibashi, Y. Tomota, H. Suzuki, T. Saito and S. Ryufuku

2.6.6 Assessment of Vanadium Alloys 82
A. Hoshikawa, S. Kakei, H. Yoshinaga, T. Ishigaki and T. Kamiyama

2.6.7 Detection of Hydrogen Trapped by Nano-scale Carbide by SANS 83
M. Ohnuma, F.G. Wei, K. Tsuzaki and J. Suzuki

2.6.8 Measurement of Inclusions in Steel by Small Angle Neutron Scattering 84
S. Morooka, Y. Tomota, J. Suzuki, M. Ohnuma, K. Kikuchi and T. Shiraga

2.6.9 Evaluation of Magnetization on $Fe_{16}N_2$ Nanoparticles by Polarized Neutrons Diffraction 85
Y. Ishii, M. Takeda, K. Kakurai, T. Kikuchi, T. Shinohara, T. Oku, J. Suzuki, Y. Sasaki, M. Kishimoto, M. Yokoyama and Y. Nishihara

2.6.10 Magnetic Structure of Fe-N Nanoparticles for Magnetic Recording Tape Studied by Small-angle Polarized Neutron Scattering 86
T. Kikuchi, T. Oku, T. Shinohara, J. Suzuki, Y. Ishii, M. Takeda, K. Kakurai, Y. Sasaki, M. Kishimoto, M. Yokoyama and Y. Nishihara

2.6.11 Quantitative Evaluations of Microstructural Factors by Neutron Diffraction for Cold Rolled austenitic Stainless Steels 87
H. Suzuki, T. Saito, J. Y. Tomota, T. Suzuki, P.-G. Xu and S. Ryufuku

2.7 Fundamental Physics 89
Interferometry

2.7.1 A Development of the Neutron Beta Decay Experiment with Superconducting Tunnel Junction (STJ)s 91
K. Mishima, H. Sato, S. Yamada, T. Shinohara, T. Oku, J. Suzuki and H. M. Shimizu

2.8 Instrumentation and Methods 93
Extreme Conditions, Beam Handling, Detectors and Data Treatments

2.8.1 Development of High Performance Neutron Supermirrors with Ion Beam Sputtering Technique 95
R. Maruyama, D. Yamazaki, T. Ebisawa, M. Hino and K. Soyama

2.8.2 Feasibility Tests on the Pressure-transmitting Media for Single-crystal Magnetic Neutron Diffraction Experiments 96
T. Osakabe

2.8.3 Performance Test of Neutron Detector for Engineering Diffractometer in J-PARC 97
K. Sakasai, T. Nakamura, M. Katagiri, A. Birumachi, T. Hosoya, K. Soyama, S. Satoh, E. Shooneveld and N. Rhodes

2.8.4 Measurement of Energy Spectrum of Neutron Beam at MUSASI Port 98
K. Sakasai, N. Metoki and H. Matsue

2.8.5 Development of High Quality Neutron Mirrors with Upgrading Cold Neutron Bender System 99
I. Tamura, D. Yamazaki, R. Maruyama, K. Yamamoto, K. Nakamura and K. Soyama

2.8.6 Upgrading Cold Neutron Bender System 100
I. Tamura, R. Maruyama, K. Yamamoto, K. Nakamura, K. Aizawa and K. Soyama

2.8.7 Attempt of Residual Stress Measurements in Multi-Purpose Thermal Neutron Application and Science (MUSASI) 101
S. Machiya, A. Moriai, H. Suzuki, N. Metoki, Y. Akiniwa and Y. Morii

2.8.8 Performance Test of Radial Collimator Basic Performance Test 102
S. Harjo, S. Torii, A. Moriai and K. Shirakihara

2.8.9 Performance Test of Radial Collimator Application Test on PSZ Material ..104
K. Shirakihara, S. Harjo and A. Moriai

2.8.10 Test of Prototype ^{3}He PSDs and Related Electronics for New Spectrometers at J-PARC 106
K. Nakajima, T. Yokoo, S. Satoh, M. Nakamura, N. Kaneko, Y. Kobayashi and R. Kajimoto

2.8.11 Development of a Neutron Polarizing Device Based on a Quadrupole Magnet and Evaluation of Its Polarizing Power 107
T. Oku, S. Yamada, T. Shinohara, J. Suzuki and H. M. Shimizu

2.8.12 Profile of a Neutron Reflectometer SUIREN at C2-2, JRR-3 109
D. Yamazaki, A. Moriai, I. Tamura, R. Maruyama, T. Ebisawa, K. Soyama, M. Takeda and M. Hino

2.9 Neutron Radiography 111

2.9.1 Neutron Tomography Analysis of Metal Hydride Canister with/without Hydrogen Charging and Discharging Cycle 113
Y. Fujita, T. Ebisawa, H. Iikura and M. Matsubayashi

2.9.2 Development of Neutron Imaging Techniques for PEM Fuel Cells (II) 114
M. Matsubayashi, H. Iikura and R. Yasuda

2.9.3 Evaluation Research for Long Term Stability of Metal 115
M. Matsubayashi, H. Iikura and H. Yishikawa

2.10 Prompt Gamma-ray Analysis 117

2.10.1 Determination of Cadmium in Polymer Samples by MPGA 119
Y. Toh, M. Oshima, M. Koizumi, A. Kimura, K. Sushida and M. Sato

Appendix A 123

Program Committee for Neutron Beam Utilization in the JFY 2006
of the Advisory Council for JAEA's Research Facilities

Appendix B 124

Publication List in the Period of the JFY 2006

JRR-3 Beam Experimental Facilities

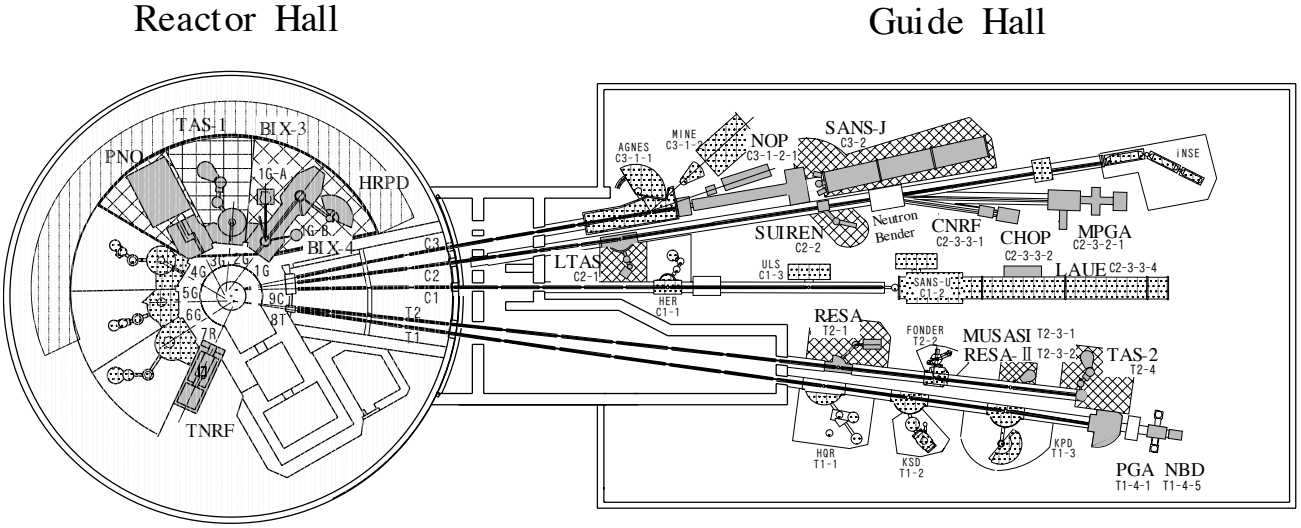

This is a blank page

Neutron Science Relations in JAEA

April, 2006- March, 2007

Organization Structure of JAEA

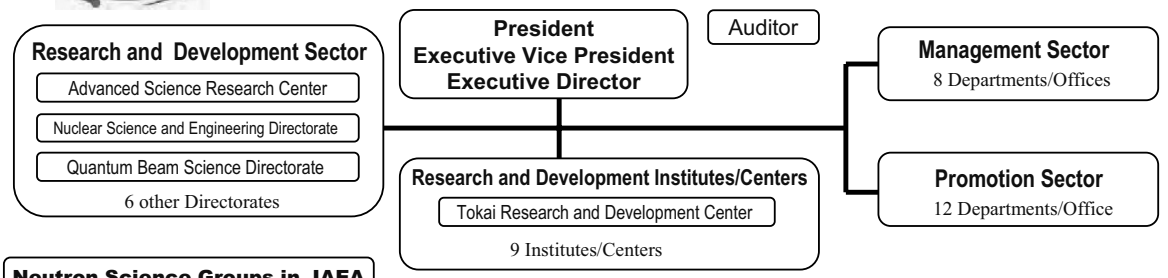

Neutron Science Groups in JAEA

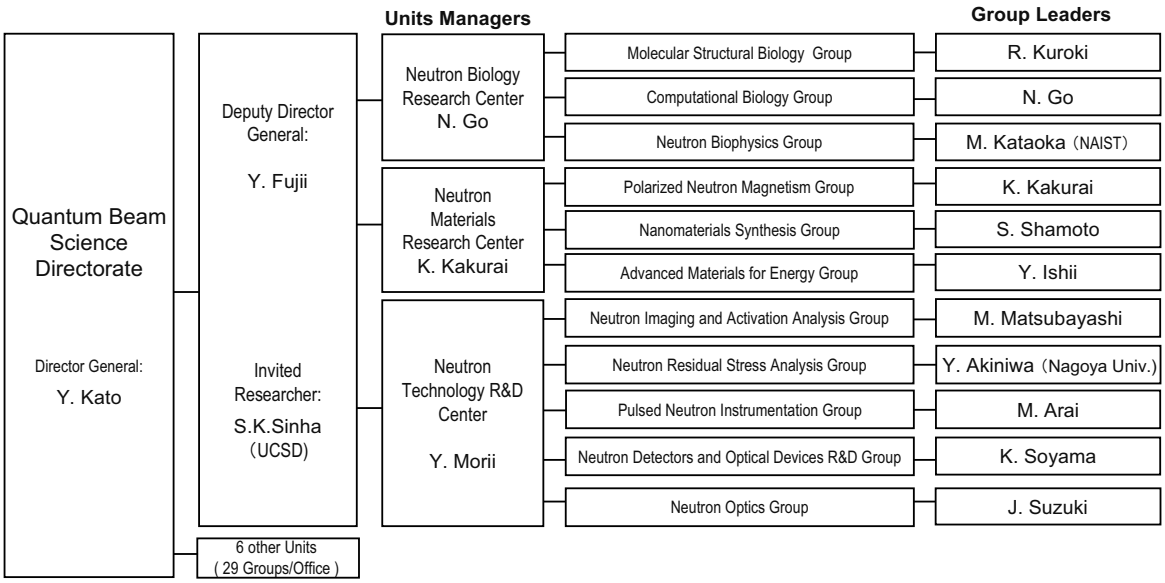

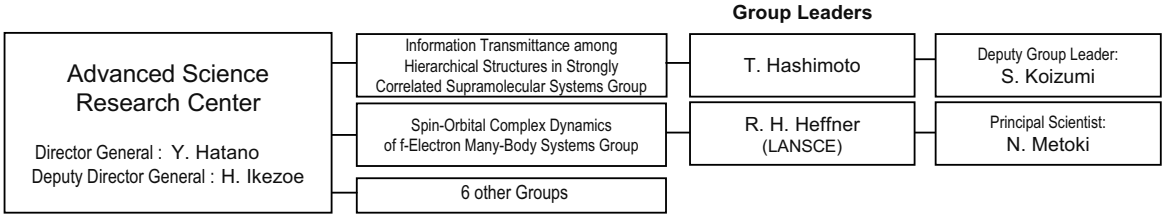

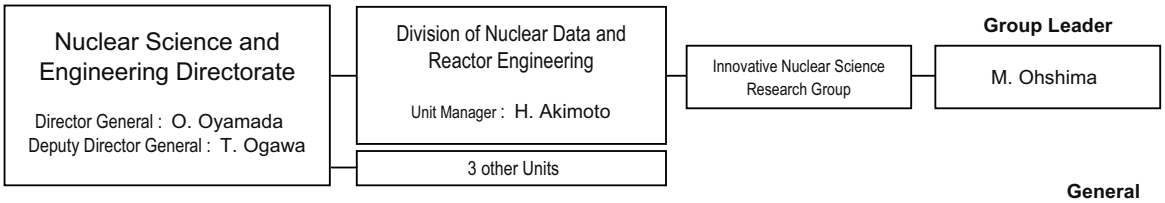

*1 January 2007 ～ *2 ～ December 2006 , January 2007 ～ K. Yamashita *3 ～ December 2006

Neutron Science Relations in JAEA

April, 2007-

Organization Structure of JAEA

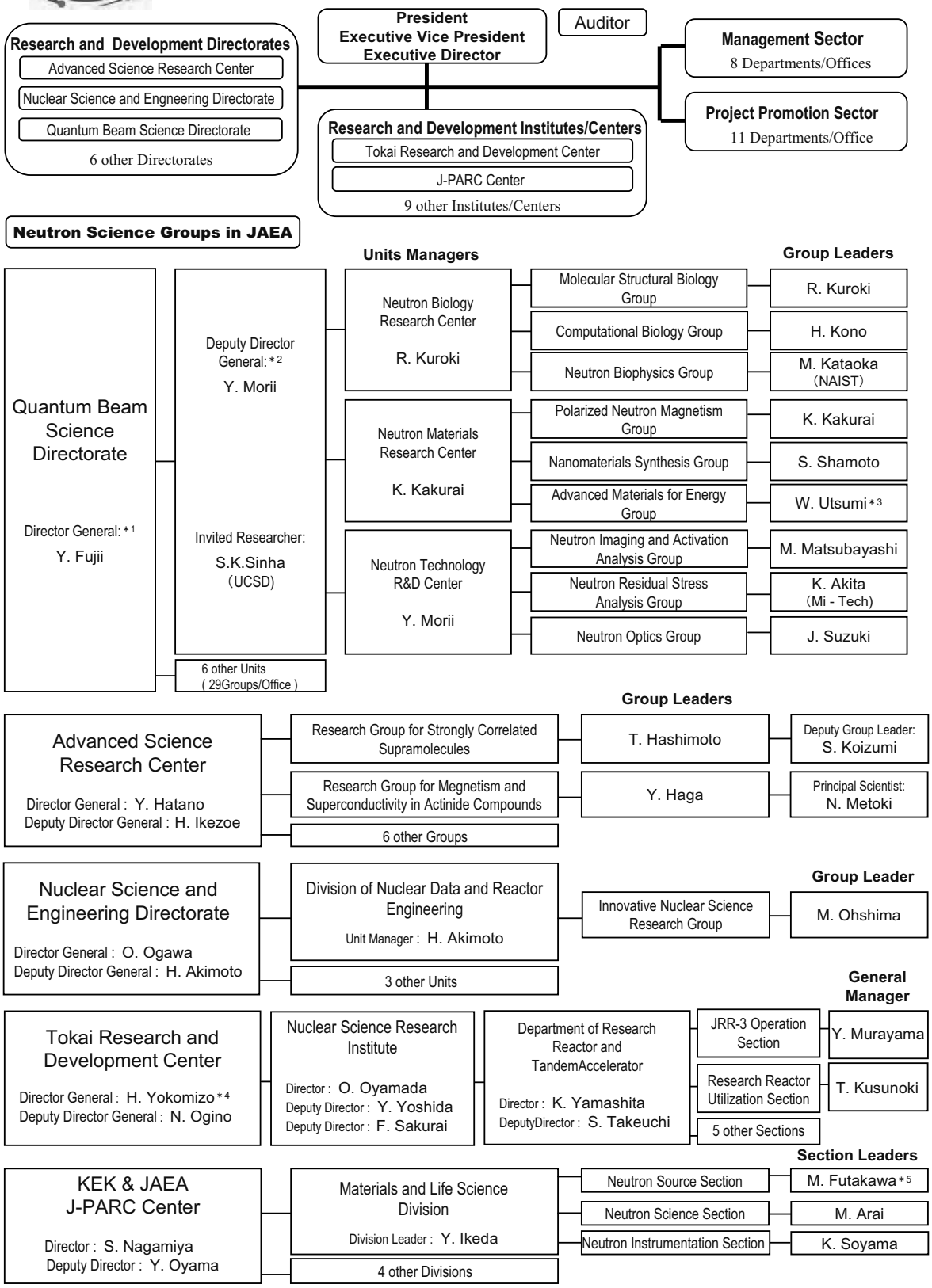

*1 ～ September 2007. Y.Kato *2 ～ September 2007. Y. Fujii *3 ～ September 2007. K. Kakurai *4 ～ September 2007. Y. Suzuki
*5 ～ September 2007. T. Kato

List of JAEA Instruments

A. Neutron Scattering Instruments

Beam Port	Instrument	Moderator	Instrument Staff
1G	High Resolution Powder Diffractometer (HRPD)	Thermal (H_2O)	Naoki Igawa, Hiroshi Fukazawa
1G-A	Diffratometer for Biological Crystallography-III (BIX-3)	Thermal (H_2O)	Taro Tamada, Takashi Ohhara
1G-B	Single Crystal Diffractometer for Biological Macromolecules (BIX-4)	Thermal (H_2O)	Kazuo Kurihara, Takashi Ohhara
2G	Triple-Axis Spectrometer (TAS-1)	Thermal (H_2O)	Kazuhisa Kakurai, Masayasu Takeda
3G	Apparatus for Precise Neutron Optics and Neutron Diffraction Topography (PNO)	Thermal (H_2O)	Satoshi Koizumi, Kazuya Aizawa
7R C2-3-3-1	Thermal Neutron Radiography Facility (TNRF) Cold Neutron Radiography Facility (CNRF)	Thermal (H_2O) Cold (Liquid H_2)	Masahito Matsubayashi, Hiroshi Iikura
T1-4-1	Prompt Gamma-ray Analysis System (PGA)	Thermal (H_2O)	Hideaki Matsue
T1-4-5	Apparatus for Neutron Beta Decay Measurement (NBD)	Thermal (H_2O)	Jun-ichi Suzuki
T2-1 T2-3-2	Diffractometer for the Residual Stress Analysis (RESA) (RESA-Ⅱ)	Thermal (H_2O)	Hiroshi Suzuki, Atsushi Moriai
T2-3-1	Multi-Purpose Thermal Neutron Application and Science (MUSASI)	Thermal (H_2O)	Naoto Metoki
T2-4	Triple-Axis Spectrometer (TAS-2)	Thermal (H_2O)	Masaaki Matsuda, Shuichi Wakimoto
C2-1	Low energy Triple-Axis Spectrometer (LTAS)	Cold (Liquid H_2)	Koji Kaneko
C2-2	Apparatus for Surface and Interface Investigations with Reflection of Neutrons (SUIREN)	Cold (Liquid H_2)	Kazuhiko Soyama, Dai Yamazaki
C2-3-2-1	Multiple Prompt Gamma-ray Analysis (MPGA)	Cold (Liquid H_2)	Masumi Ohshima, Yosuke Tou
C2-3-3-2 C2-3-3-4	(CHOP) (LAUE)	Cold (Liquid H_2)	Kazuya Aizawa, Kentaro Suzuya
C3-1-2-1	Apparatus for Neutron Optics (NOP)	Cold (Liquid H_2)	Takayuki Oku, Jun-ichi Suzuki
C3-2	Small-Angle Neutron Scattering Instrument (SANS-J)	Cold (Liquid H_2)	Satoshi Koizumi, Jun-ichi Suzuki

B-1. Cryostats, Magnets and Furnaces

Accessory	Number	Performance	Instrument Staff
Dilution Refrigerator	1	T_{min} = 10 mK, H_{max} = 5 T (Vertical)	Naoto Metoki
Dilution Refrigerator (Lquid-^{4}He-Free)	2	T_{min} = 50 mK	Naoto Metoki
10T Magnet (Liquid-^{4}He-Free)	1	T_{min} = 100 mK, H_{max} = 10 T (Vertical)	Naoto Metoki
Orange Cryostat	1	T_{min} = 1.5 K	Toyotaka Osakabe
Horizontal Magnet	1	T_{min} = 1.5 K, H_{max} = 5 T (Horizontal)	Jun-ichi Suzuki
4 K Cryostat	2	T_{min} = 4 K	Yutaka Shimojo
10 K Cryostat	6	T_{min} = 10 K	Yutaka Shimojo
Furnace for Soft Matter	1	T = 0 – 300 ºC	Satoshi Koizumi
800 K Displex	1	T = 5 – 800 K	Masaaki Matsuda
Furnace	2	T_{max} = 1100 K	Yutaka Shimojo
Furnace	1	T_{max} = 2000 K	Yutaka Shimojo

B-2. Pressure Devices

McWhan Cell	3	P_{max} = 2.7 GPa Cell Size : 100 mmΦ× 140 mm Sample Size : 5 mmΦ× 6 mm	Toyotaka Osakabe
Hybrid Anvil Cell	1	P_{max} = 6.5 GPa Cell Size : 45 mmΦ× 77 mm Sample Size : 1 mmΦ× 0.25 mm	Toyotaka Osakabe
Cu-Be Cell	1	P_{max} = 1.0 GPa Sample Size : 3 mmΦ× 18 mm (The cell is used with a standard orange cryostat. Pressure is chngeable from the outside of the cryostat.)	Toyotaka Osakabe
Uniaxial-Stress Cell	1	L_{max} = 2.0 ton Sample Size : 10 mmΦ× 10 mm (The cell is used with a standard orange cryostat. Load is changeable from the outside of the cryostat.)	Toyotaka Osakabe
Oscillatory Shear Machine	1	T = RT – 200 ºC, Amplitude = 0.01 - 2 mm, Frequency = 0.1 - 100 Hz	Satoshi Koizumi
Stress Rig	1	Tensil Speed = 0 - 0.01 mm/sec, Range of Load = 50 - 1000 kgf ± 1%	Atsushi Moriai, Hiroshi Suzuki

B-3. Detectors

Neutron Imaging Plate	several	Resolution = 100 μm	Ryota Kuroki

1. Highlights in Research at JAEA

This is a blank page

1.1 X-ray and Neutron Crystallography for Structure Determination of Biological Macromolecules

Molecular Structural Biology Group
R. Kuroki

Increasing the number of protein whose structures have been determined will enable us to understand the protein function and also create new molecules. Neutron crystallography is a powerful tool for determining the location of hydrogen atoms, and also enables us to obtain information about the ionization status of amino acids and the structure of hydrating waters. Here, we introduce the latest developments in protein crystallization techniques and structural determination using neutron diffraction.

In an attempt to crystallize a protein, we introduced a leucine zipper-like hydrophobic interface (comprising four leucine residues) into a helical region (helix 2) of the human pancreatic ribonuclease 1 (RNase 1). This mutant RNase 1 was successfully crystallized and its structure was determined[1]. This example shows that a crystal interface can be artificially created by protein engineering. We also succeeded in determination of the neutron crystal structure of porcine pancreatic elastase (PPE) (EC 3.4.21.36) that is classified in the chymotrypsin family, and this structure has been used as a model for structure based drug design (SBDD). Previously, we succeeded in collecting neutron diffraction data of PPE with its inhibitor to 2.3 Å resolution[2]. After improvement of the size of PPE crystal, we succeeded in collection of neutron diffraction data to 1.75 Å resolution, and the PPE structure was refined to a crystallographic R-factor of 21.2 % (free R-factor = 29.6 %) including the inhibitor, two ions (calcium and sulfate), and 141 deuterated waters. Protonation of histidine at an active site was clearly confirmed by measurement of its nuclear densities (Figure 1). Moreover, in collaboration with Prof. Ogo (Kyushu Univ), we succeeded in determination of the crystal structure of Ni(μ-H)Ru complex $[(Ni^{II}L)(H_2O)(\mu\text{-}H)Ru^{II}(\eta^6\text{-}C_6Me_6)](NO_3\}\{[2](NO_3)\}$, where L = N,N'-dimethyl-N,N'-bis(2-mercaptoethyl)-1,3-propanediamine by single crystal neutron diffraction. A Ni(μ-S)2(μ-H)Fe species is one of the candidates for mimicing the active form of the [NiFe]hydrogenase, which catalyzes the activation of H_2 into two protons(H^+) and two electrons (e^-).

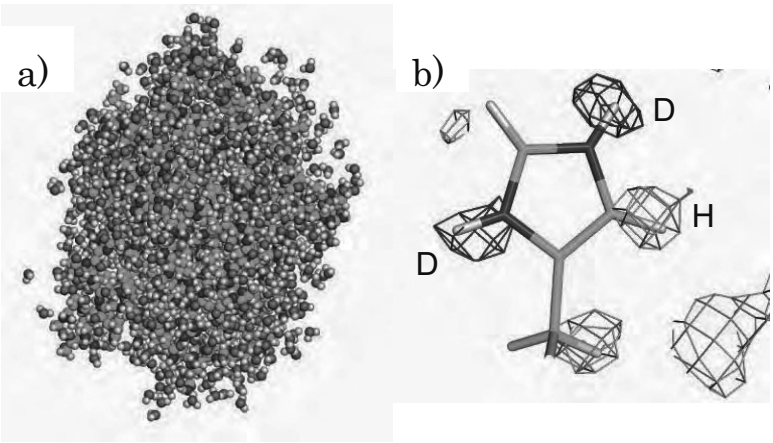

Figure 1: Tertiary structure of Porcine Pancreatic Elastase determined by neutron crystallography. (a) Overall structure of PPE including hydrogens and hydrating waters. (b) Nuclear density of active site histidine residue. PPE structure includes carbon, oxygen, nitrogen, sulfate and hydrogen and deutreium.

References

1) H. Yamada *et al*.: Protein Science, 16, p. 2458 (2007).
2) T. Kinoshita *et al*.: Acta Crystallographica Ser. F, 63, p. 315 (2007).
3) S. Ogo *et al*.:Science, 316, p. 585 (2007).

1.2 DNA Deformability and Hydration Studied by Molecular Dynamics Simulation

Computational Biology Group
H. Kono

DNA conformation and deformability depend on sequence composition. The variability in DNA conformation and deformability is believed to be one of the most important factors in specific recognition of DNA sequence by regulatory proteins. To investigate the differences in DNA conformation and deformability among distinct DNA sequences, we have carried out molecular dynamics simulations and found that AATT sequence is the most rigid and TTAA is the most flexible among all possible 136 tetramer sequences[1]. To elucidate the causes for such mechanism, we analyzed the hydration patterns of the two sequences[2].

The probabilities of observing a water molecule in a minor groove of the sequences AATT and TTAA are significantly different. In AATT, a water bridge is found with a high probability throughout the simulation. On the other hand, in the TTAA case, the bridge-forming rate is relatively low, and in particular, bridge formation at the central site is very rare. This tendency is in accordance with a previous experimental observation made by Mack *et al*[3].

The above difference in bridge-forming rate can be explained in terms of the distance between two acceptor atoms. At the central site of AATT with a high probability of bridge formation, the average distance between acceptor atoms is 3.64 ± 0.35Å (one standard deviation) which is a suitable distance for the bridge formation when considering the geometry of hydrogen bonds participating in the bridge. On the other hand, this distance in TTAA is 5.74 ± 1.19 Å, which is too long to make bridge-constructing hydrogen bonds. We can clearly see such characteristics in the figure where regions having three times higher density than bulk water are shown by green meshes. In AATT, the high density regions are aligned along the minor groove. On the other hand, in the TTAA minor groove, there are no high density regions indicating the bridge water sites.

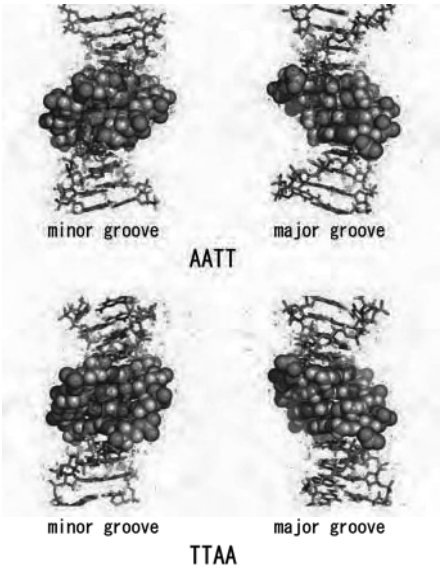

This study indicates that the conformational characteristics of DNA are highly correlated with its hydration pattern. Our results are not sufficient to thoroughly explain the relationship between DNA hydration and deformability, but this will be elucidated through further systematic investigation of various sequences.

References

1) M. J.Arouzo-Bravo *et al.*: J. Am. Chem. Soc. 127, pp. 16074-16089 (2005).
2) Y. Yonetani *et al.*: Molecular Simulation 33, pp. 103-107 (2007).
3) D. R. Mack *et al.*: J. Mol. Biol. 312, pp. 1037-1049 (2001).

1.3 Protein Dynamics Studied by Neutron Scattering

Neutron Biophysics Group
M. Kataoka

When a protein functions, its structural changes inevitably occur. The structural changes of the protein are possible because of structural fluctuations in the protein. Characterization of protein structure dynamics is therefore of central importance in understanding the functions of the protein. Aiming at the elucidation of the dynamics-structure-function relationship, we have been studying the dynamics and the structures of the proteins by various methodologies of neutron scattering. Two examples, which focus on the protein dynamics, from recent studies are described here.

Dynamics of hydration water around a protein

Thermal fluctuations, or internal dynamics, of a protein are closely related to the dynamics of the water molecules hydrated to the protein. To characterize the hydration water dynamics, incoherent elastic neutron scattering experiments were performed on powder samples of the protein, Staphylococcal nuclease (SNase), hydrated with H_2O or D_2O. The scattering from the hydration water was extracted by subtracting the scattering profile of the D_2O-hydrated sample from that of the H_2O-hydrated sample. Figure 1 shows the temperature dependence of the mean-square displacement (MSD) of SNase and the hydration water at the hydration ratios, h, of 0.27 (g water/g protein) and 0.37, estimated from the scattering profiles of the protein and the hydration water. At h=0.27 the MSD's of the protein and the hydration water behave similarly. On the other hand, the MSD of the hydration water at h=0.37 is significantly larger than that of the protein above the dynamical transition observed at ~240K. The dynamical behavior of the hydration water is coupled with the protein dynamics via the hydrogen-bond network at the protein-water interface, thereby driving the protein dynamical transition.

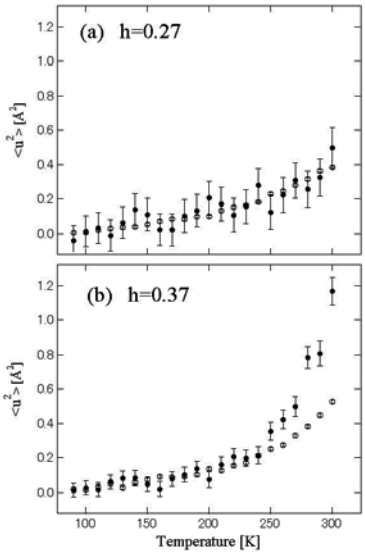

Figure 1: Mean-square displacements of hydrated protein (●) and its hydration water (○) at (a) h=0.27 hydration level and (b) h=0.37 hydration level.

Internal dynamics of actin

Actin is one of the most abundant proteins in a cell; it plays crucial roles in various aspects of cell motility. The actin monomers (G-actin) polymerize into a helical polymer (F-actin). Flexibility of this F-actin has been suggested to be important for such a variety of functions. To provide a basis for elucidating the origin of the flexibility of F-actin, we carried out elastic incoherent neutron scattering experiments on hydrated powders of F-actin and G-actin and characterized their internal dynamics. Temperature dependence of the MSD estimated from the experiments showed that F-actin and G-actin have different behavior. Analysis of the results showed that two dynamical transitions occur at about 150K and about 245K, that G-actin is "softer" than F-actin, and that the different behavior observed can be ascribed to the differences in the dynamical heterogeneity of F-actin and G-actin.

1.4 Investigation of Condensed Matter Magnetism by Polarized Neutron Scattering

Polarized Neutron Magnetism Group
K. Kakurai

The research objectives of the Polarized Neutron Magnetism Group are the development of novel polarization analysis methods and the utilization of both unpolarized and polarized neutrons for the investigation of condensed matter magnetism. For this purpose we upgraded the polarized neutron capabilities of TAS-1 and installed the 3-D polarization analysis instrument, CRYOPADUM, in collaboration with French scientists from ILL and CEA-Grenoble(Takeda *et al*. in the Progress Report on Neutron Science 2006). Our research put emphasis on the investigation of correlation between spin and other degrees of freedom such as those of charge, orbital and lattice, which play important roles in explaining novel phenomena in condensed matter such as those observed in multiferroic materials (Kimura *et al*., Kajimoto *et al*.,Wakimoto *et al*., Kakurai *et al*., Nishiwaki *et al*. in this report), high-Tc superconductors(Matsuda *et al*., Wakimoto *et al*. in this report), and low-dimensional(e.g. Takeda *et al*., Oosawa *et al*. in this report), quantum (Goto *et al*., Hase *et al*., Ono *et al*. in this report), and frustrated spin systems(e.g. Soda *et al*., Kashi *et al*. and Miura *et al*. in this report). Polarized neutron diffraction experiments on ferromagnetic fine particles have been also performed (Ishii *et al*, Oitani *et al*. in this report) to evaluate the magnetization of the core ferromagnetic material. To investigate the interplay between the different degrees of freedom, a high magnetic field sample environment up to 13.5 T and a single crystal high pressure sample environment up to 6.8 GPa (Osakabe in this report)have been developed and are now in operation. (Matsuda *et al*. in the Progress Report on Neutron Science 2006 and Osakabe *et al*. in this report).

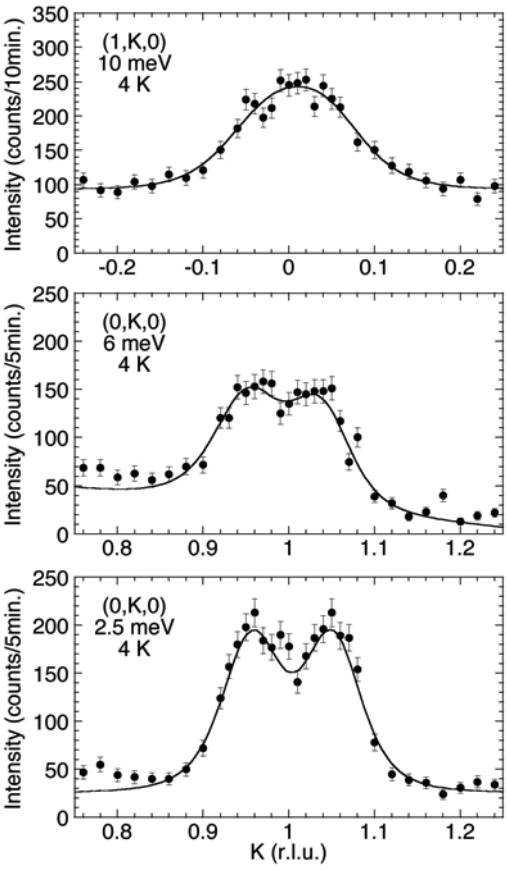

Figure 1: Typical constant-energy spectra in the diagonal incommensurate phase in lightly-doped $La_{2-x}Sr_xCuO_4$. The incommensurability decreases with increasing energy, similar to those observed in the parallel incommensurate phase compounds. For more details see Matsuda *et al*. in this report.

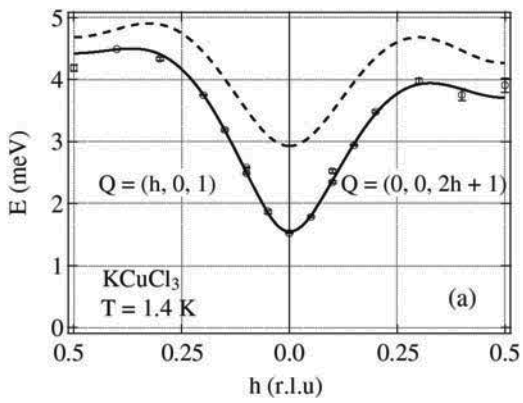

Figure 2: Softening of the dispersion relation in $KCuCl_3$ measured at P = 4.7 kbar applied pressure along (h,0,l) and (0,0,2h+1). Dashed line is the dispersion curve at ambient pressure. For more details see Goto *et al*. in this report.

1.5 Functional Materials Studied by Neutron Diffraction

Nanomaterials Synthesis Group
S. Shamoto

Physical properties of functional bulk materials depend on their crystal structures, i.e. whether they are crystalline or amorphous. As an in-between case, disorder in a crystalline material sometimes plays an important role in certain types of functionality. Recently developed high intensity quantum beams, such as pulsed neutron and synchrotron X-ray beams, provide a total scattering measurement with simultaneous high *Q*-resolution and high intensity, creating a wide *r*-range atomic pair distribution function (PDF). By using the wide *r*-range information, materials categorized between crystalline and amorphous materials can be explored in terms of their nanometer-scale local structure. Based on this concept, we have studied functional materials such as optical recording materials[1)], giant negative thermal expansion materials[2)], thermoelectric materials[3)], ferroelectric materials[4,5)], and fullerene related nanomaterials. As for the optical recording materials, two types of the optical recording crystalline material $Ge_2Sb_2Te_5$ have been studied. One is the crystalline rock-salt-type cubic-phase $Ge_2Sb_2Te_5$. The other is the nanocrystalline-phase $Ge_2Sb_2Te_5$. In the former case, a large atomic displacement of Ge atom was found by the PDF analysis. According to the electronic band structure calculation of the compound GeTe which is isoelectronic with $Ge_2Sb_2Te_5$ (Fig. 1), the electrical conductivity with holes at the valence band is only weakly affected by randomness at the cation site, whereas the thermal conductivity is significantly reduced by this randomness. For the nanocrystalline phase, the local crystal structure and the particle size distribution were obtained simultaneously by PDF analysis using a spherical-particle form factor (Fig. 2). The lattice parameter is longer than that of the crystalline phase, suggesting an composition richer in antimony ($GeSb_2Te_4$) than the matrix. This compositional deviation would be a cause of the nanoparticle formation in an amorphous matrix, resulting in nucleation-dominated crystal growth of this compound.

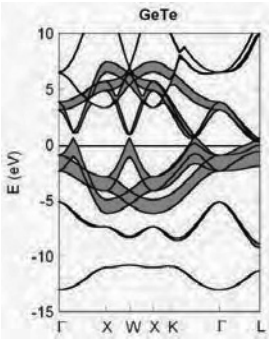

Figure 1: Electronic band structure of GeTe. The energy band broadness is proportional to the contribution of Te 5*p* orbitals.

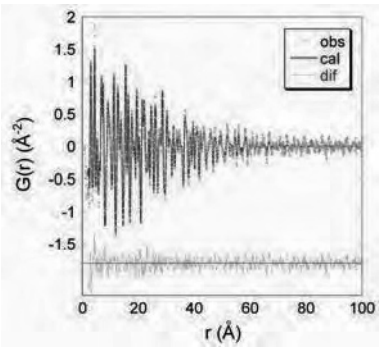

Figure 2: Observed and calculated and difference pair distribution function profiles of nano-crystalline-phase $Ge_2Sb_2Te_5$.

References

1) S. Shamoto, K. Kodama, S. Iikubo *et al.*: Jpn. J. Appl. Phys. 45-11, p. 8789 (2006).
2) S. Iikubo, K. Kodama, K. Takenaka, H. Takagi and S. Shamoto: Phys. Rev. B (Rapid Communications) in press.
3) S. Shamoto, Y. Hasegawa and T. Kajitani: Jpn. J. Appl. Phys. 45-8A, p. 6395 (2006).
4) A. A. Belik, S. Iikubo, K. Kodama *et al.*: J. Am. Chem. Soc. 128, p. 706 (2006).
5) A. A. Belik, S. Iikubo *et al*: J. Am. Chem. Soc. 129, p. 971 (2007).

1.6 Neutron Scattering Studies on Advanced Energy-Related Materials

Advanced Materials for Energy Group
K. Kakurai

The research objectives of the Advanced Materials for Energy Group are the structural and dynamical characterizations of proton-related materials, such as hydrogen clathrate (Igawa *et al*., in this report), ice (Fukazawa *et al*., in this report), and proton-conducting materials (Nagasaki *et al*. in this report), and materials with light elements, such as lithium-ion containing substances (Basar *et al*. and Yamauchi *et al*. in this report), which are often relevant as advanced energy-related materials. Neutron is the unique probe for these research subjects, being very sensitive to protons, hydrogen, deuterium and other light elements often difficult to investigate by other scattering methods. For these investigations, the group maintains the high-resolution powder diffractometer HRPD at JRR-3 and develops sample environment accessories such as a low-T, high-pressure cell and high-T furnace for powder diffraction experiments. The application of the maximum entropy method (MEM) for powder diffraction analysis is also being investigated to characterize the dynamical behavior of molecules in hydrate clathrates or deuterium atoms in proton conductors. The high- intensity wide-angle diffractometer WAND at HFIR of Oak Ridge National Laboratory, operated within the 'US-Japan Cooperative Program on Neutron Scattering', is also actively utilized to promote the investigations of ice, which recently resulted in the discovery of the conditions under which ferroelectric ice XI forms.

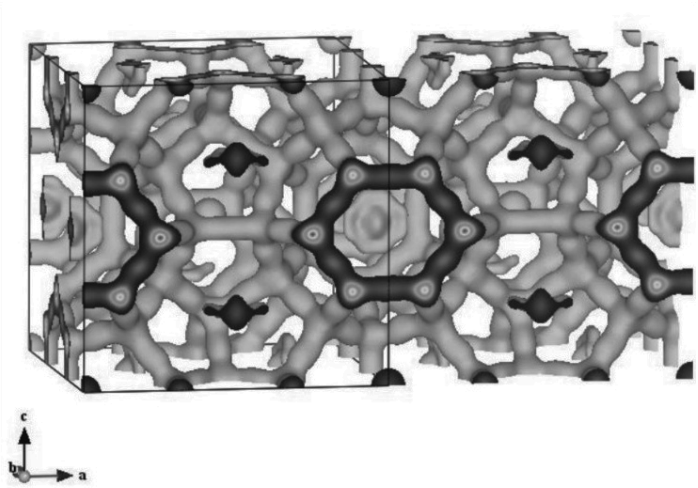

Figure1: Scattering length density map of CO_2 hydrate at 10K, as obtained by MEM. Two unit cells are shown in this figure. Small cages are located at the corner and center of the unit cell and large cages are located at the faces of the unit cell.. In the synthesized hydrate both cage types were found to be almost fully occupied with carbon dioxide molecules at 10K. For more details see Igawa *et al*. in this report.

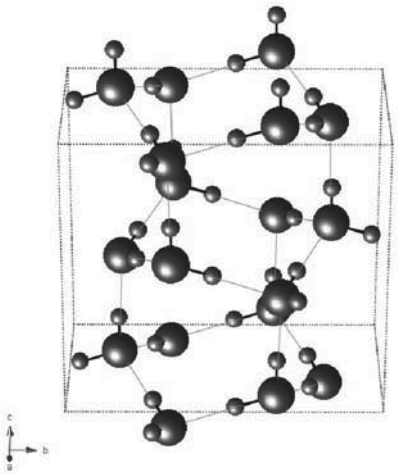

Figure 2: Ice XI with proton-ordered arrangement. Since water molecules are aligned along c-axis (vertical direction), ice XI is ferroelectric For more details see Fukazawa *et al*. in this report.

1.7 Diverse Studies on Neutron Imaging

Neutron Imaging and Activation Analysis
M. Matsubayashi

Neutron imaging is expected to be powerful non-destructive inspection technique. The following studies were conducted using the neutron radiography facility installed at JRR-3.

Projection images of the JARI (Japan Automobile Research Institute) standard type PEMFC (proton exchange membrane fuel cell) for computed tomography (CT) in three states were obtained : 1) dried, 2) anode side flow channel filled with water ("one-side wet"), 3) anode/cathode side flow channels filled with water ("both-sides wet"). Two types of reconstruction calculation were applied : 1) conventional FBP (Filtered Back Projection) method, and 2) FBP method using specialized shading images as projection images for the dried state (specialized-FBP). As clearly seen in Fig.1, the quality of the left image (specialized-FBP) is better than that of the right one (conventional-FBP).

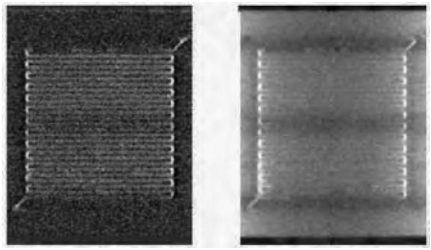

Figure 1: 2D vertical slice reconstructions of PEMFC. the left image reconstructed by specialized-FBP method, the right by conventional-FBP method.

Hydrogen is expected to be an ideal clean energy source for the future, but it is difficult to store hydrogen compactly, lightly and safely. Metal hydride (MH) is one of the practical hydrogen storage mediums, which can absorb and desorb a large amount of hydrogen in its interstitial sites at ordinary temperatures and low pressure. Two MH canisters, MH-1 and MH-2, were prepared for CT. Both canisters' rated hydrogen amount was 50 NL. Each canister contained 330 g of MH grain and six tubular glass sleeves for improving hydrogen ventilation. MH-1 had been charged with and discharged of hydrogen once. On the other hand, MH-2 had undergone 1000 cycles. Both canisters were discharged of almost all the hydrogen and filled with 0.2 MPaG argon gas. As shown in Fig. 2, tomograms carried out on MH canisters subjected to 1 cycle and 1000 cycles revealed that the filled MH itself expands in volume with the charge/discharge cycle, so that the glass sleeves for hydrogen ventilation collapsed.

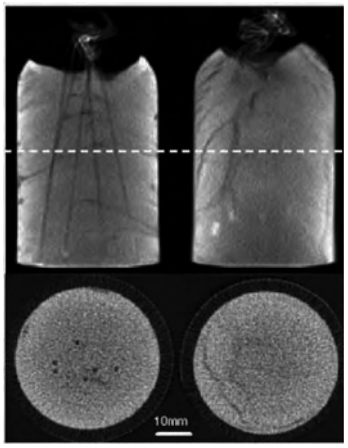

Figure 2: Neutron tomography analysis result of 1 cycled (MH-1, left) and 1000 cycled (MH-2, right) canister.

Neutron imaging technique was applied to improve estimation of the amount of corrosion in iron-artifact left underground for geologic isolation research and development. Carbon steel (SM400B, 30 × 30 × 2 mm thick) was soaked in simulated seawater under natural conditions for almost 5 years, and its surface became corroded as shown in Fig. 3, a CT image. Reduction of the base metal of the carbon steel plate was clearly observed in the computed tomograms. Experimental results show the effectiveness of neutron imaging in corrosion evaluation of carbon steel.

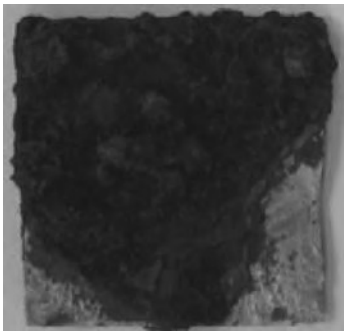

Figure 3: Corroded carbon steel sample.

1.8 Residual Stress Analysis and Advanced Research in Materials Science

Neutron Residual Stress Analysis Group
K. Akita

Neutron diffraction methods can measure residual stresses inside materials at depths on the order of centimeters nondestructively. Residual (*hkl*) lattice strains can be determined from the shifts in the diffraction peak positions from that of the stress-free condition. Residual stresses can be calculated from lattice strains measured in three orthogonal directions according to Hooke's law. The neutron stress measurement method, in general, has been utilized for evaluation of the condition of various mechanical components. Recently, it has been applied to the stress evaluation of functional and advanced materials, e.g. superconducting tapes or metallic glasses, as well.

We used this method to investigate a BSCCO Bi2223 Ag sheathed tape with the characteristics of high Ic (HIc) and high strength (HS). It is known that critical current in superconducting tapes has stress/strain dependence; hence, it is important to know the phase stresses between the Ag sheath and Bi filament. We measured the strain behavior in each phase under uniaxial tensile load using a neutron diffraction technique[1]. Figure 1 shows the stress/strain behaviors of Bi(220) and Ag(110). It was confirmed that the gradients of the Bi phase HIc and HS are quite similar and show almost linear relationships with the applied stress, while the strain behavior of Ag phase is not linear because of yielding.

This neutron diffraction method also enables us to measure microstructural factors such as texture, intergranular strain, dislocation density, and block size. The dislocation density and the block size can be evaluated by analyzing the diffraction profile. We have established a new technique which can evaluate various microstructural factors by superimposing them on the pole figure.

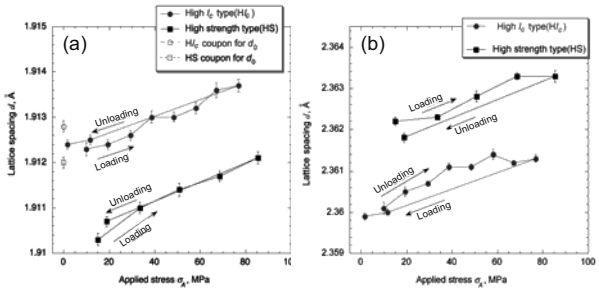

Figure 1: Changes in lattice spacing of (a) Bi(220) and (b) Ag(110) respect to the applied stress in BSCCO Bi2223 Ag-sheathed tapes.

Figure 2 shows the gradation images of dislocation density and block size pole figures superimposed on a texture contour map of 316 stainless steel with 25% cold rolling reduction. It can be seen in this figure that there is good correlation between texture and dislocation density as well as block size, which means that higher dislocation density and smaller block size are coincide with weaker intensity.

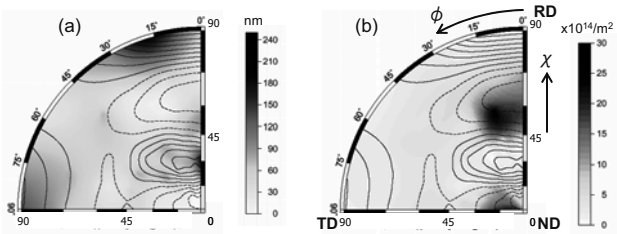

Figure 2: Pole figures of (a) block size and (b) dislocation density derived from 111 diffraction profile in 316SS with 25% reduction. Contour separation for the texture is 0.25 and dotted-lines indicate levels below 1.0.

Residual stresses and microstructural factors measured by the neutron diffraction method are very helpful in the design and the development of engineering components as well as studies in materials science.

References

1) S. Machiya *et al*.: Supercond. Sci. Technol. submitted.

1.9 Development and Construction of Pulsed-Neutron Scattering Instruments for J-PARC

Pulsed Neutron Instrumentation Group
M. Arai

We have constructed the following three pulsed-neutron scattering instruments at MLF/J-PARC.

1) The Cold Neutron Disk-Chopper Spectrometer (AMATERAS)

The Cold-Neutron Disk-Chopper Spectrometer (AMATERAS) is a direct-geometry spectrometer which will realize both high-resolution ($\Delta E/E_i < 1\%$) and high-intensity with high flexibility in the range of $E_i = 1 \sim 20$ meV, and will exhibit sufficient performance up to $E_i < 80$ meV. AMATERAS is expected to be useful in such varied scientific research areas as solid state physics, chemistry, materials science, and soft matter science. Execution design of each component of AMATERAS is in process now. Construction of the main part of the spectrometer will be finished in the middle of JFY 2008, and AMATERAS is expected to be ready for use at the end of JFY 2008.

2) Engineering Materials Diffractometer (TAKUMI)

The Engineering Materials Diffractometer (TAKUMI) will be one of the instruments in place at MLF/J-PARC when the first beam is produced in May 2008. A prototype of the radial collimator with 1mm gauge width for TAKUMI was made to clarify the design concept, and good agreement with the concept has been obtained from neutron beam tests in JRR3. The satellite building construction for TAKUMI will be completed in middle November 2007, and the installation of shieldings, neutron guides, and main parts such as the goniometer and slits is to be completed on March 2008. TAKUMI will be installed fully in 2008, and hopefully become ready for users from April 2009.

3) 4D Space-Access Neutron Spectrometer (4SEASONS)

The Fermi-type chopper spectrometer (4SEASONS) is specially dedicated to the elucidation of the mechanism of high-Tc superconductivity. The instrument design of 4SEASONS realizes high neutron flux at the sample position by utilizing novel neutron optic devices, the wide incident energy range 5 meV $< E_i <$ 300 meV, and moderate energy resolution ($\Delta E/E_i$ = 5 % at elastic scattering). Construction of 4SEASONS is now at its peak. A lot of equipment, such as the guide tube system, main shielding, chopper system and long (2.5 m) ^{3}He position sensitive detectors, are in the process of production and will be installed by the end of JFY2007. A 22 m^3 vacuum scattering chamber has been already completed and delivered to the MLF experimental hall as shown in Fig. 1. 4SEASONS will be operated in May 2008 as a day one instrument of MLF/J-PARC. After some commissioning tests, 4SEASONS will be ready for advanced scientific exploration. The construction of 4SEASONS is supported by a Grant-in-Aid for Specially Promoted Research, MEXT, Japan (No. 17001001).

Figure 1: Vacuum scattering chamber for 4SEASONS.

1.10 Development of Neutron Detectors and Neutron Optical Devices

Neutron Detectors and Optical Devices R&D Group
K. Soyama

We have developed neutron detectors for neutron scattering experiments using high-intensity pulsed neutron sources. A prototype linear scintillation detector originally developed at RAL was fabricated for the engineering diffractometer in J-PARC. The fabricated detector was designed to have small detection pixels with a spatial resolution of 3 mm. The detector had 120 pixels in order to establish a large neutron-sensitive area. Scattered neutrons were detected based on the nuclear reaction of ^{6}Li(n, α) in ZnS/LiF scintillators in the pixel. Figure 1 shows the detector head with photomultiplier tubes. A spatial resolution of approximately 3 mm and the linearity of the neutron count of the fabricated detector were confirmed.

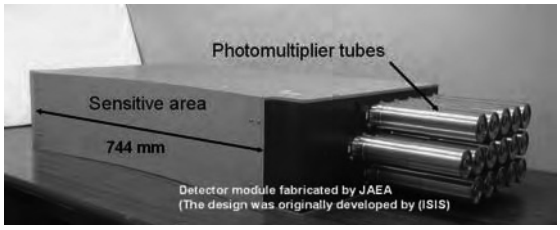

Figure 1: 1-D ZnS:Ag/^{6}LiF Scintillator Detector (ISIS type).

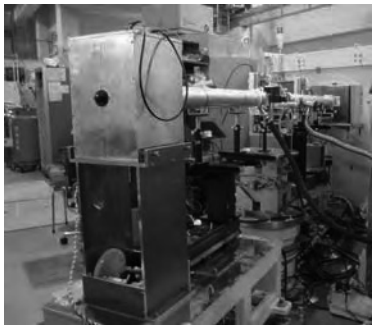

Figure 2: The new cold neutron reflectometer "SUIREN" at JRR-3 of JAEA.

The operation of a new cold neutron reflectometer "SUIREN", which will be utilized for studying the surfaces and interfaces of thin film optical devices, started at the C2-2 port of the JRR-3 in 2006. JAEA accepts requests from academic and industrial researchers to use SUIREN. JAEA has already provided 26 days of use to external researchers in 2006 and will provide 60 days in 2007. This instrument has vertical-sample geometry and is going to be used for studies on supermirrors, polymers, magnetic thin films and other materials with solid surfaces. The neutron wavelength is 3.8 Å and collimated intensity is 2.3×10^{4} n/s/cm^{2}/s with $\delta\theta = \pm 0.04$ deg at the sample position. Test measurements were performed before the beginning of operation by users. Figure 1 shows specular reflectivity of a silicon wafer together with a fitting curve for a Si wafer with surface oxidization of 5 Å. It was found that there is reflectivity down to 10^{-6} (Q_z < 0.42 Å^{-1}). A measurement took 59 h. Polarization analysis will be available in 2007. A 1 T sample magnet and a refrigerator (10 K ~) will also be available in the future.

1.11 Development and Application of Neutron Optics

Neutron Optics Group
J. Suzuki

We have developed neutron optical and imaging devices[1-2] and used the devices for focusing-geometry small-angle neutron scattering (F-SANS) measurements[3-4] and neutron β-decay measurements in collaboration with the ASRC in-house research group for soft matter neutron scattering, KEK, RIKEN, NIMS, the University of Tokyo, Hokkaido University, Ibaraki University, and Keio University.

Figure 1 (left) shows a pulsed sextupole electromagnet[5] installed at the 45 MeV electron linear accelerator facility of Hokkaido University in a joint research project and (right) a system including a series sextupole permanent magnet[6] installed at NOP of JRR-3, which have been developed to focus polychromatic neutrons with a the time-of-flight method. In the former system, the gradient of magnetic field G is controlled by changing the electric current applied to the electromagnet synchronously with the neutron passage through the electromagnet, so that faster neutrons will be subjected to a stronger magnetic field gradient than slower neutrons. On the other hand, in the latter system the polarity of neutrons is controlled by a spin flipper synchronously with the neutron passage through the system, so that faster neutrons are subjected to focusing power in both sextupole magnets and slower neutrons are subjected to focusing power in the first sextupole magnet but are subjected to defocusing power in the second sextupole magnet. We have successfully demonstrated that we can focus neutrons in the finite wavelength band of 0.2 ~ 0.3 nm using these systems. The wavelength bands are narrow at present, but a technique to widen the wavelength band will be developed in the near future.

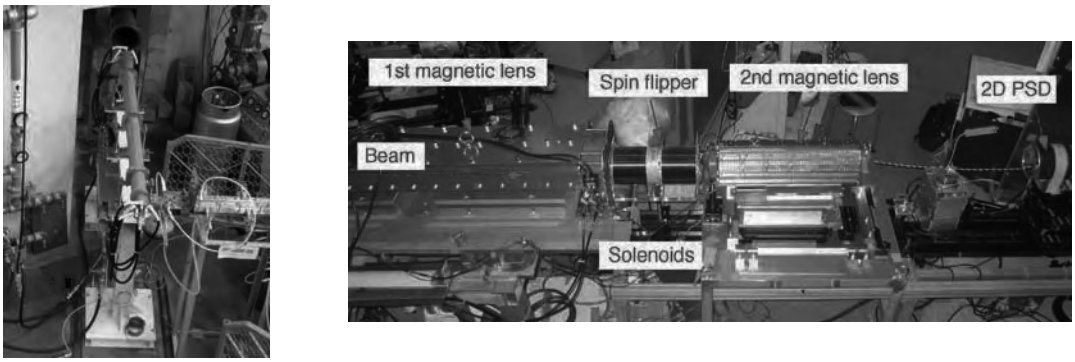

Figure 1: Pictures of (left) a pulsed sextupole electromagnet installed at the 45 MeV electron linear accelerator facility of the Hokkaido University under joint research and (right) a series sextupole permanent magnet installed at NOP of JRR-3.

References

1) J. Suzuki *et al*.: J. Appl. Crystallogr. 36, pp. 795-799 (2003).
2) T. Oku *et al*.: Proc. of the ICANS-XVI, Neuss, May 12-15, pp. 355-362 (2003).
3) T. Oku *et al*.: Physica B 385-386, pp. 1225-1228 (2006).
4) T. Oku *et al*.: J. Appl. Crystallogr. 40, pp. s408-s413 (2007).
5) J. Suzuki *et al*.: Nucl. Instrum. Meth. A 529, pp. 120-124 (2004), T. Shinohara *et al*., to be prepared.
6) J. Suzuki *et al*., to be prepared.

1.12 Investigation of Hierarchical Structures by Ultra-Small-Angle Neutron Scattering: a Bridge between Material Science and Life Science

Information Transmittance among Hierarchical Structures
in Strong Correlated Supramolecular Systems Group
S. Koizumi and T. Hashimoto

Two ultra-small-angle neutron scattering spectrometers, i.e., a focusing type (SANS-J-II)[1] and a Bonse-Hart double type crystal diffractometer (PNO), play a crucial role to detect q in the wide range of $1.0 \times 10^{-5} < q < 0.3$ Å^{-1} (see pictures), where q is the magnitude of the scattering vector ($q = 4\pi/\lambda \sin\theta$, defined by scattering angle 2θ and wavelength λ). We utilized these instruments in order to investigate hierarchical structures found in strongly correlated supramolecular systems, composed of artificially synthesized polymers and/or biopolymers. In addition to wide-q observation, advantages using neutrons as the probe include variable scattering contrast by deuteration, high permeability, and the possibility of simultaneous measurement with other probes (UV and IR). Especially for living materials or organisms, the low energy of cold neutrons is an important advantage because chemical damage is prevented.

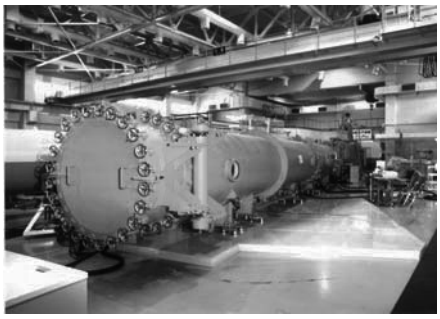

A living anionic copolymerization solution was examined by SANS, simultaneously with UV-vis, GPC and NMR (Zhao *et al.* in this report). In this way, molecular assemblies induced by living polymerization, such as microdomains, we've quantitatively understood and related to changes in monomer conversion. The hierarchical structure of two porous silica powders, obtained before and after compression during sample preparation, was compared (Yamaguchi *et al.* in this report).

A study of red blood cells has shown the possibility of quantitatively determining detailed structures in the cell, such as nucleus in cytoplasm, thickness of cell membrane, and the volume ratio of hemoglobin to water in the blood cell (Iwase *et al.* in this report). A study of an in vitro model solution of cytoskeletons, which are composed of actin and cationic polymer, was done by adding salt, which induces bundle formation by actin filaments (Masui *et al.* in this report). Thus, local concentration fluctuation of salt was found to be important to control cell motion.

References

1) S. Koizumi, H. Iwase, J. Suzuki, T. Oku, R. Motokawa, H. Sasao, H. Tanaka, D. Yamaguchi, H. M. Shimizu, and T. Hashimoto: J. Apply. Cryst. 40, s474-s479 (2007).

1.13 Precise Single Crystal Neutron Diffraction Investigation on *Rattling* in Cage Compounds

Spin-Orbital Complex Dynamics of f-electron Many-body Systems Group
K. Kaneko

Strong thermal vibration of a guest atom in an over-sized host cage, called "*rattling*", has become one of the key issues in the recent condensed matter physics. Especially, the relation of rattling with the emergence of superconductivity in skutterudite $PrOs_4Sb_{12}$[1] and β-pyrochlore AOs_2O_6[2] (A = K, Rb, Cs) has attracted considerable interest. At present, details of the rattling are still under debate, for instance with regard to possible existence of off-center potential minima. Neutron diffraction is a sensitive tool for detecting thermal vibration, since a neutron is scattered by `local' nuclear forces, whereas electrons spread around the nuclei are the scattering medium for x-rays. Recent progress in structural analysis using the maximum entropy method (MEM) offers the possibility of revealing a non-standard structure, including rattling, without any specific model. In order to obtain a detailed picture of rattling in $PrOs_4Sb_{12}$, single crystal neutron diffraction experiments were carried out on FONDER installed at JRR-3. MEM analysis and visualization of obtained data were done using the PRIMA and VESTA software, respectively.

Figure 1(a) shows the nuclear scattering length density distribution of $PrOs_4Sb_{12}$ above 1 fm/Å^3 at room temperature, obtained through MEM analysis. Reflecting the large thermal displacement of the Pr ion, a widely spread nuclear density distribution can be seen at the center of the Sb icosahedron cage. Note that the Pr distribution is anisotropic with an almost cubic shape, which is not allowed according to standard structural analysis. The Pr density extends in the maximum length toward the <111> direction, corresponding to one of the voids of the Sb icosahedron cage and pointing towards Os. Cross-sectional drawings of the Pr density along the [100] direction at 8 K and room temperature are shown in Fig. 1(b). It is clearly seen that Pr has a characteristic trapezoidal distribution at room temperature. This is far from Gaussian shape expected for a harmonic oscillator, indicating a presence of strong anharmonicity for Pr. The peak height at room temperature is much lower than that at 8 K. Note that the maximum density of Pr at 8 K is found at the central position. In addition, the distribution becomes Gaussian and isotropic at 8 K. The present results clearly show that no well-separated off-center potential minima cause the rattling in $PrOs_4Sb_{12}$. Thermal vibration of Pr exhibits strong variation in both amplitude and anisotropy with temperature, between 8 K and room temperature, which may reflect its characteristic potential shape. A detailed investigation of variation of the Pr distribution with temperature is expected to give keen insights into underlying anharmonic potential, which will help quantitative discussion and further understanding of the relation of rattling to various physical properties.

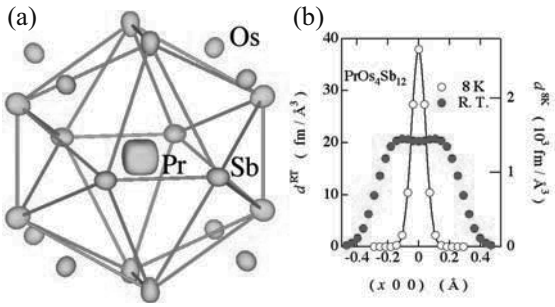

Figure 1: Nuclear density distribution of $PrOs_4Sb_{12}$ at room temperature and cross sectional nuclear density distribution of Pr along [100] at 8 K and room temperature.

References

1) T. Goto *et al.*: Phys. Rev. B, 69, p. 180511(R) (2004).
2) Z. Hiroi *et al.*: Phys. Rev. B, 76, p. 014523 (2007).

This is a blank page

2. Research Reports

2.1 Biology

Structure and Mechanism

This is a blank page

2.1.1
Defect Study of Protein Crystals by Neutron Topography

H. Koizumi, N. Ohya, M. Koishi, N. Kitajima, Y. Mukohbayashi, M. Tachibana, K. Kojima, K. Kurihara[1] and R. Kuroki[1]

International Graduate School of Arts and Sciences, Yokohama City University, Yokohama 236-0027
[1]*Japan Atomic Energy Agency (JAEA), Tokai, Ibaraki 319-1195*

In common crystals, the mosaic structure has two structure types that are a Frank network and a fine polygonization wall. Both of the structures are composed of dislocations. However, the mosaic structure of protein crystals has not been identified in terms of dislocation models yet. Thus, the characterization of defects, especially dislocations, in protein crystals is important for the understanding of their quality of crystals. The crystallization originating from dislocations has been investigated using atomic force microscopy (AFM). However, AFM is limited to only local observations of the crystal surface. It is desired that the distribution of dislocations in the whole crystal could be observed. Topographic techniques (X-ray topography and neutron topography) is one of the most powerful tools for characterization of dislocation in the crystal. Therefore, we have performed the application of X-ray topography to protein crystals[1)], and consequently, we have succeed in clear observations of the dislocation images in hen egg-white (HEW)lysozyme crystals[2)3)]. On the other hand, the application of neutron topography to protein crystals has not been carried out so far. Especially, effect of water around dislocations can be observed only using neutron topography. Therefore, to obtain the interaction between intracrystalline water and dislocations in protein crystals, we tried to perform the application of neutron topography to lysozyme crystals.

The used orthorhombic HEW lysozyme crystals were grown by a liquid-liquid interfacial precipitation technique. To avoid the high background coming from the incoherent neutron scattering of hydrogen atoms, the crystallization experiments were carried out in D_2O solution. Neutron topography was carried out using LAUE on C2-3-3-4 at JRR-3. The camera length was 21 cm. Topographs were recorded on a film instead of an imaging plate with exposure times of about 1 week.

Figure. 1 shows Laue topographs which were recorded with the incident beam almost parallel to the [110] crystallographic direction of orthorhombic HEW lysozyme crystal. This is the first photograph of neutron topography applied to protein crystals. It should be noticed that a topographic image corresponds to the shape of crystals of the lysozyme using X-ray topography. In addition, this topographic contrast attributes to dislocations observed by X-ray topography. The photo showed the lack of image of the crystal in the lower part of the crystal. This means that the quality of crystals is not sufficient to take a clear image. More detail observation using more high quality crystals should be required to obtain the fine structures.

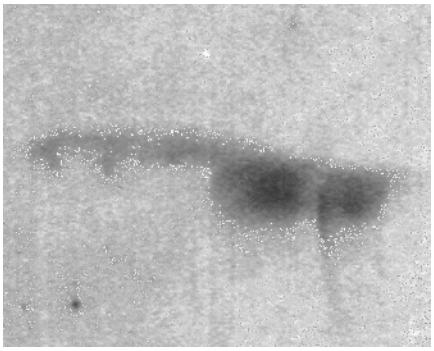

Figure 1: Topographic image of an orthorhombic HEW lysozyme crystal obtained using neutron topography.

References

1) M. Tachibana and K. Kojima, J. Synchrotron Rad., 10, 416(2003).
2) H. Koizumi, M. Tachibana, I. Yoshizaki and K. Kojima, Philosophical Magazine, 85, 3709(2005).
3) H. Koizumi, M. Shimizu, M. Tachibana and K. Kojima, Physica Status Solidi (a), (2007)(in press).

measured at depths of 2.5, 4.5, 8.5 and 12.5 mm are shown in Fig.2, in which the profiles were obtained from poled, unpoled, poled and unpoled specimen, respectively. The peak intensities of (002) reflection in the poled specimens are larger than those in the unpoled specimens, showing that the spontaneous polarization direction is parallel to the [002] direction. Therefore, the domain switching properties can be estimated from the difference between the diffraction profile of a poled specimen and that of an unpoled one. The (002) and (200) diffraction intensity distribution with respect to scattering angle and penetration depth is plotted in Fig.3. The lowest intensity (zero) is shown by black (dark) color, and the color becomes brighter with increasing the intensity. As shown, the first two layers are profiles from the poled specimen, the next four layers are those from the unpoled one followed by four layers from the poled one, and the last three layers are those from the unpoled one. The profiles were fitted by a convolution of Gauss and Lorenzt functions and integrated peak intensities of both reflections were evaluated. Domain switching properties can be estimated from the integrated peak intensity ratio between (002) and (200) reflections, i.e., I_{002}/I_{200}. Figure 4 shows the I_{002}/I_{200} value in a function of penetration depth. The I_{002}/I_{200} values are higher than 1 for the poled specimen, and approximately 0.5 for the unpoled specimen. The I_{002}/I_{200} value of the unpoled specimen is in a good agreement with the theoretical I_{002}/I_{200} value, demonstrating that the neutron diffraction results have good reliability. The I_{002}/I_{200} values are almost constant for different penetration depths. This is due to the fact that there was no treatment applied to the specimen, and then the degree of polarization in a whole specimen is almost uniform. On the contrary, the I_{002}/I_{200} values have fluctuations that may show the inhomogeneities of polarization in the specimen, induced during the polarization treatments. The results described above are difficult to measure by the means of XRD that only measure surface part. A combination of neutrons having high penetration ability and a fine radial collimator can realize this kind of measurement.

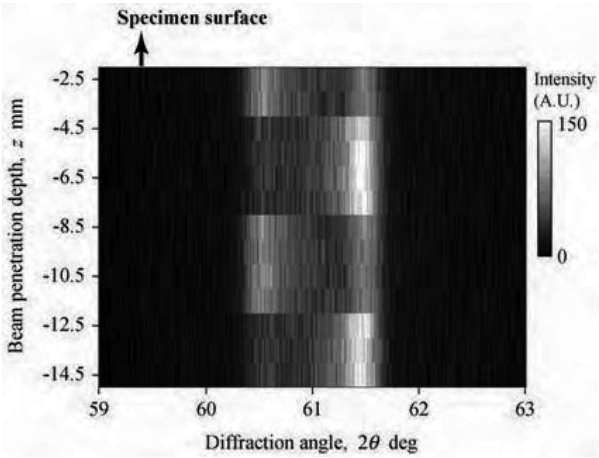

Figure 3: (002) and (200) diffraction intensity distribution with respect to scattering angle and penetration depth.

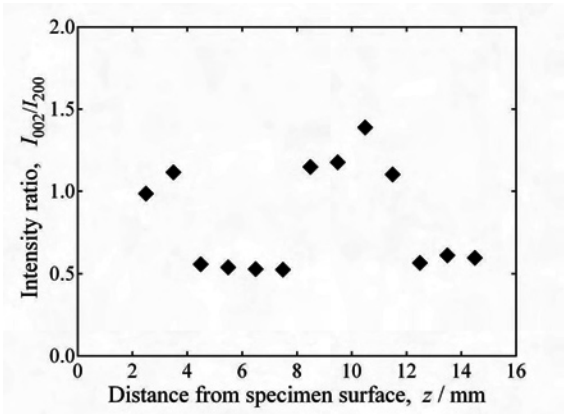

Figure 4: Integrated peak intensity ratio (I_{002}/I_{200} value) as a function of penetration depth.

References

1) S. Harjo, S. Torii, A. Moriai and K. Shirakihara, JAEA-Review (2.8.8 in this reports).

measured at depths of 2.5, 4.5, 8.5 and 12.5 mm are shown in Fig.2, in which the profiles were obtained from poled, unpoled, poled and unpoled specimen, respectively. The peak intensities of (002) reflection in the poled specimens are larger than those in the unpoled specimens, showing that the spontaneous polarization direction is parallel to the [002] direction. Therefore, the domain switching properties can be estimated from the difference between the diffraction profile of a poled specimen and that of an unpoled one. The (002) and (200) diffraction intensity distribution with respect to scattering angle and penetration depth is plotted in Fig.3. The lowest intensity (zero) is shown by black (dark) color, and the color becomes brighter with increasing the intensity. As shown, the first two layers are profiles from the poled specimen, the next four layers are those from the unpoled one followed by four layers from the poled one, and the last three layers are those from the unpoled one. The profiles were fitted by a convolution of Gauss and Lorenzt functions and integrated peak intensities of both reflections were evaluated. Domain switching properties can be estimated from the integrated peak intensity ratio between (002) and (200) reflections, i.e., I_{002}/I_{200}. Figure 4 shows the I_{002}/I_{200} value in a function of penetration depth. The I_{002}/I_{200} values are higher than 1 for the poled specimen, and approximately 0.5 for the unpoled specimen. The I_{002}/I_{200} value of the unpoled specimen is in a good agreement with the theoretical I_{002}/I_{200} value, demonstrating that the neutron diffraction results have good reliability. The I_{002}/I_{200} values are almost constant for different penetration depths. This is due to the fact that there was no treatment applied to the specimen, and then the degree of polarization in a whole specimen is almost uniform. On the contrary, the I_{002}/I_{200} values have fluctuations that may show the inhomogeneities of polarization in the specimen, induced during the polarization treatments. The results described above are difficult to measure by the means of XRD that only measure surface part. A combination of neutrons having high penetration ability and a fine radial collimator can realize this kind of measurement.

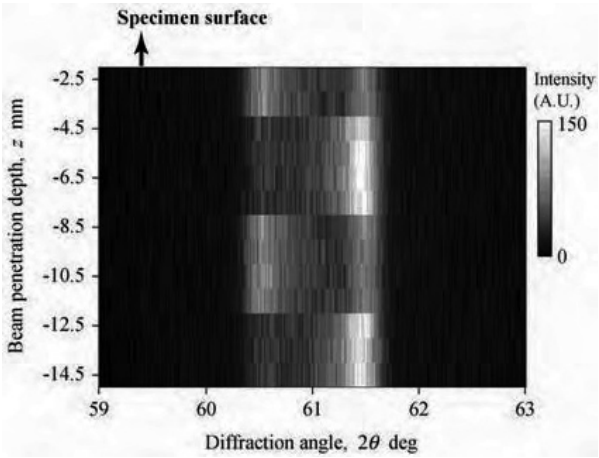

Figure 3: (002) and (200) diffraction intensity distribution with respect to scattering angle and penetration depth.

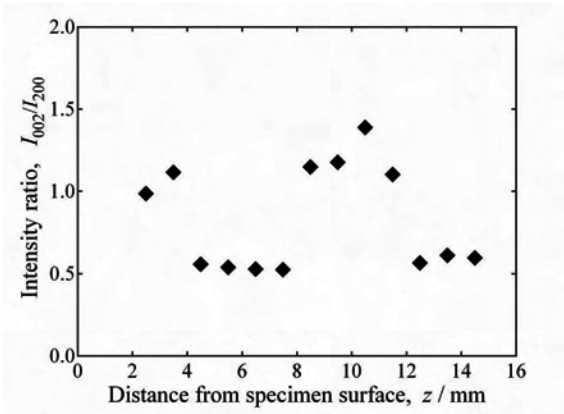

Figure 4: Integrated peak intensity ratio (I_{002}/I_{200} value) as a function of penetration depth.

References

1) S. Harjo, S. Torii, A. Moriai and K. Shirakihara, JAEA-Review (2.8.8 in this reports).

measured at depths of 2.5, 4.5, 8.5 and 12.5 mm are shown in Fig.2, in which the profiles were obtained from poled, unpoled, poled and unpoled specimen, respectively. The peak intensities of (002) reflection in the poled specimens are larger than those in the unpoled specimens, showing that the spontaneous polarization direction is parallel to the [002] direction. Therefore, the domain switching properties can be estimated from the difference between the diffraction profile of a poled specimen and that of an unpoled one. The (002) and (200) diffraction intensity distribution with respect to scattering angle and penetration depth is plotted in Fig.3. The lowest intensity (zero) is shown by black (dark) color, and the color becomes brighter with increasing the intensity. As shown, the first two layers are profiles from the poled specimen, the next four layers are those from the unpoled one followed by four layers from the poled one, and the last three layers are those from the unpoled one. The profiles were fitted by a convolution of Gauss and Lorenzt functions and integrated peak intensities of both reflections were evaluated. Domain switching properties can be estimated from the integrated peak intensity ratio between (002) and (200) reflections, i.e., I_{002}/I_{200}. Figure 4 shows the I_{002}/I_{200} value in a function of penetration depth. The I_{002}/I_{200} values are higher than 1 for the poled specimen, and approximately 0.5 for the unpoled specimen. The I_{002}/I_{200} value of the unpoled specimen is in a good agreement with the theoretical I_{002}/I_{200} value, demonstrating that the neutron diffraction results have good reliability. The I_{002}/I_{200} values are almost constant for different penetration depths. This is due to the fact that there was no treatment applied to the specimen, and then the degree of polarization in a whole specimen is almost uniform. On the contrary, the I_{002}/I_{200} values have fluctuations that may show the inhomogeneities of polarization in the specimen, induced during the polarization treatments. The results described above are difficult to measure by the means of XRD that only measure surface part. A combination of neutrons having high penetration ability and a fine radial collimator can realize this kind of measurement.

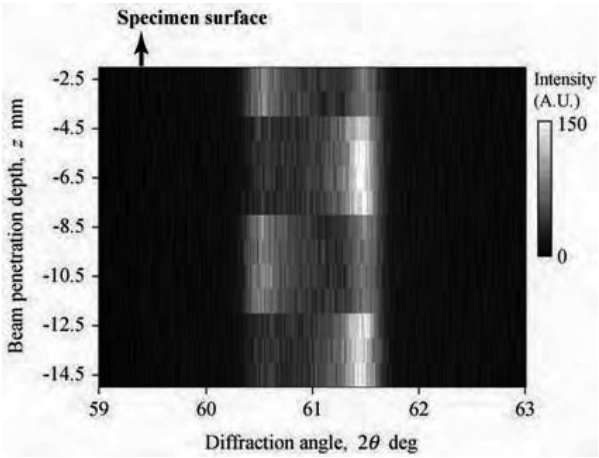

Figure 3: (002) and (200) diffraction intensity distribution with respect to scattering angle and penetration depth.

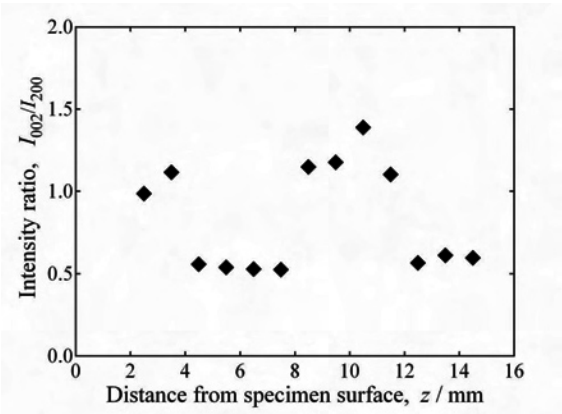

Figure 4: Integrated peak intensity ratio (I_{002}/I_{200} value) as a function of penetration depth.

References

1) S. Harjo, S. Torii, A. Moriai and K. Shirakihara, JAEA-Review (2.8.8 in this reports).

2.1.5
Neutron Diffraction Study of Porcine Pancreatic Elastase with Its Inhibitor

T. Kinoshita, T. Tamada[1], T. Ohhara[1], K. Kurihara[1], T. Tada and R. Kuroki[1]

Graduate School of Science, Osaka Prefecture University, Sakai, Osaka 599-8531
[1]*Quantum Beam Science Directorate, JAEA, Tokai, Ibaraki 319-1195*

Porcine pancreatic elastase (PPE) is a serine protease classified in the chymotrypsin family that is possibly the most destructive enzymes having the ability to degrade virtually all of the connective components in the body. Uncontrolled proteolytic degradation by pancreatic elastase (EC 3.4.21.36) causes the fatal disease pancreatitis. Inhibitor for PPE is typical subject of development by structure based drug design (SBDD) because some elastases have similar structures of active sites. Nevertheless, many inhibitors designed by SBDD using X-ray structures still have side effects. A more detailed structure including hydrogen and hydration information is useful to develop highly selective inhibitors. Neutron structure analysis is the only method to determine hydrogen and hydration of protein structures. Last fiscal year, we collected the 2.3 Åneutron data using a crystal with a size of 1.6 mm^3.[1)] Here we report the collection of higher resolution data using a larger crystal of PPE with its inhibitor.

A macro-seeding procedure was repeatedly performed during four months by adding the PPE-inhibitor complex in a deuterated buffer to a seed crystal. Finally, a seed crystal was grown to a size of 3.3 mm^3. Diffraction data were collected at room temperature using a monochromatic neutron beam (λ = 2.9 Å) and recorded on a neutron imaging plate on BIX-3 diffractometer at JRR-3 in JAEA. Full data set from a rotation about two independent axes was merged to enhance completeness. A total rotation range of 166.8° was covered by 556 oscillation images with an exposure time of 4 h/image by a rotation angle of 0.3°. The data were processed with the programs DENZO and SCALEPACK. Full data set was integrated and scaled to 1.75 Åresolution. The number of observed reflections was 69,089, which were merged into 21,103 unique reflections with an R_{merge} of 0.095 and a completeness of 91.9 %. Crystallographic refinement using by the program CNS is now in progress. The present model, including PPE, inhibitor, two ions (calcium and sulfate), and 238 deuterated waters, which were refined to a crystallographic R-factor of 23.7 % (free R-factor = 33.9 %) to 1.75 Å resolution. Refinement statistics are summarized in Table 1. Protonation of histidine at active site was clearly confirmed on nuclear densities (Fig.1).

Table 1: Summary of refinment

R_{cryst}	0.237
R_{free} (5 % random)	0.339
No. of atoms	
total	4,372
H and D	2,271
mean B value (Å^2)	12.4
r.m.s. deviations	
bond lengths (Å)	0.012
bond angles (°)	4.5

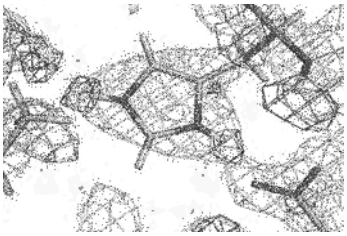

Figure 1: Nuclear densities at active sites. light: 2Fo-Fc map (+1σ), deep: Fo-Fc map (+2σ).

References

1) T. Kinoshita, T. Tamada, K. Imai, K. Kurihara, T. Ohhara, T. Tada and R. Kuroki, Acta Crystallogr. Sect. F, 63, 315(2007).

2.1.6
Single Crystal Neutron Structure Analysis of a [NiFe]hydrogenase Model Complex

S. Ogo[1], R. Kabe[1,2], K. Uehara[2], B. Kure[1,2], T. Nishimura[2], S. C. Menon[2], R. Harada[1], S. Fukuzumi[2],Y. Higuchi[3], T. Ohhara[4], T. Tamada[4] and R. Kuroki[4]

[1] *Center for Future Chemistry, Kyushu University, Fukuoka, Fukuoka 819-0395*
[2] *Department of Material and Life Science, Osaka University, Suita, Osaka 565-0871*
[3] *Department of Life Science, University of Hyogo, Kamigori, Hyogo 678-1297*
[4] *Quantum Beam Science Directorate, JAEA, Tokai, Ibaraki 319-1195*

[NiFe]hydrogenase is a bacterial enzyme that catalyzes the activation of H_2 into two protons (H^+) and two electrons (e^-). Many synthetic modeling efforts have been devoted to elucidating the core structure of the active form of the [NiFe]hydrogenase. A Ni(μ-S)$_2$(μ-H)Fe species is one of the candidates for the active form. However, ^{10}M(μ-S)$_2$(μ-H)^{8}M complexes [where ^{10}M = group 10 metals (Ni, Pd and Pt) and ^{8}M = group 8 metals (Fe, Ru and Os)] as models for the active form of the [NiFe]hydrogenase have not been reported yet.

Here, we report the successful determination of the crystal structure of Ni(μ-H)Ru complex [(Ni^{II}L)(H$_2$O)(μ-H)Ru^{II}(η^6-C$_6$Me$_6$)](NO$_3$) {[2](NO$_3$)}, where L = *N,N'*-dimethyl-*N,N'*-bis(2-mercaptoethyl)-1,3-propanediamine by single crystal neutron diffraction.

We obtained dark-red crystals of [2](NO$_3$) crystals by the reaction of NiRu aqua complex [(Ni^{II} L)Ru^{II}(H$_2$O)(η^6-C$_6$Me$_6$)](NO$_3$)$_2$ {[1](NO$_3$)$_2$} with H_2 in water under ambient comditions (20°C and 0.1 MPa)(Fig.1). Since this reaction is similar to the enzymatic reaction of [NiFe]hydrogenase, [2](NO$_3$) is thought to be a model complex of [NiFe]hydrogenase. A single crystal neutron diffraction measurement of [2](NO$_3$) was carried out using a 3.0 × 2.0 × 0.2 mm^3 crystal with the BIX-3 diffractometer at the JRR-3 reactor in JAEA. The measurement was performed using an incident neutron beam of 1.51 Å wavelength for 8 days at room temperature. Finally, 9451 reflections including 3852 unique reflections were observed. For the structure determination, the positions of hydrogen atoms were determined from a differential Fourier map and those of all atoms except a nitrate ion and a solvent water were refined independently. A nitrate ion and solvent water were refined with a rigid model. As a result of the structure analysis, we successfully the observed a negative peak which indicates existance of H between Ni and Ru (Fig. 2). This result clearly shows that [2](NO$_3$) has a Ni(μ-H)Ru structure, and strongly suggests that the active form of the [NiFe]hydrogenase has a Ni(μ-H)Fe core structure. A paper including this result has recently been published.[1)]

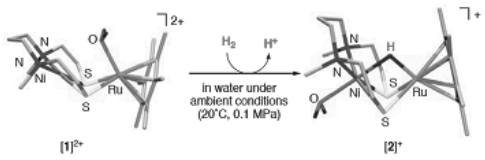

Figure 1: Formation of a Ni(μ-H)Ru complex from the reaction of a NiRu aqua complex with H_2.

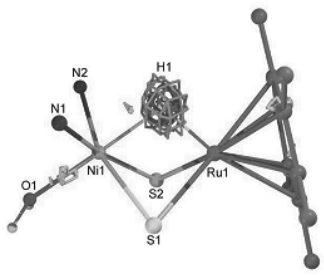

Figure 2: Fo-Fc map around the core structure of [2](NO$_3$). The mesh between Ni1 and Ru1 indicates the existance of H.

References

1) S. Ogo, et al., Science, 316, 585(2007).

2.1.7

Contrast Variation Measurements of Hen Egg White Lysozyme Amyloid Protofilaments

S. Fujiwara, F. Matsumoto and H. Nakagawa

Quantum Beam Science Directorate, JAEA, Tokai, Ibaraki 319-1195

Amyloid fibrils are filamentous protein aggregates found in a wide variety of proteins including disease-related proteins. An understanding the mechanism of the amyloid fibril formation is not only important for the development of therapeutic strategies against amyloid diseases but also of considerable help to gain an insight into the generic properties of proteins related to the mechanisms of folding and stability. It was found recently that hen egg white lysozyme (HEWL) forms the amyloid fibrils in a highly concentrated ethanol solution[1]. The HEWL-water-ethanol system is suitable to study the general mechanism of the amyloid fibril formation. From small-angle X-ray and neutron scattering (SAXS and SANS) measurements, we showed that a pathway of the amyloid fibril formation of HEWL consists of three stages; the formation of the dimers, the formation of the protofilaments, and the formation of the amyloid fibrils via a lateral association of the protofilaments[2,3].

In order to understand more in detail the mechanism by which the amyloid fibril formation occurs, it is important to obtain more detailed information on the structures of the dimers, the protofilaments, and the amyloid fibrils. In this study, as a first step towards this goal, we performed SANS experiments of the protofilaments of HEWL using the contrast variation technique. HEWL solutions, the concentration of HEWL in which was 2 mg/ml, were prepared in 90% ethanol, the condition under which the protofilaments were formed, in various fractions of the deuterated solvent. SANS curves of these solutions of HEWL were measured with SANS-J at the guide hall of the reactor JRR-3 in JAEA. The cross-sectional Guinier analysis of the curves obtained was done to estimate the cross-sectional radius of gyration at each contrast.

The dependence of the cross-sectional radius of gyration on the contrast was analyzed by the Stuhrmann plot[4], i.e., the plot of the square of the cross-sectional radius of gyration against a reciprocal of the contrast. Figure 1 shows the Stuhrmann plot of the protofilaments of HEWL. A negative slope of a linear fit to the data implies that a region of high density is located near the center of the filament.

Detailed analysis with aid of model calculation is currecntly underway.

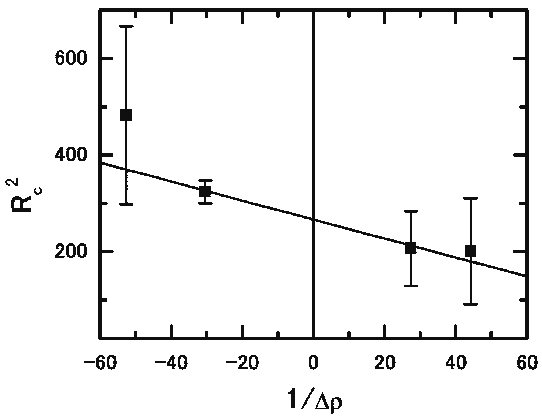

Figure 1: The Stuhrmann plot of the cross-section of the amyloid protofilament of HEWL.

References

1) S. Goda, et al., Protein Sci, 9, 369(2000).
2) Y. Yonezawa, et al., J. Mol. Biol, 323, 237(2002).
3) S. Fujiwara, et al., J. Mol. Biol, 331, 21(2003).
4) H. B. Stuhrmann, J. Appl. Cryst, 7, 173(1974).

2.1.8
Hierarchical Structure for Red Blood Cells Observed by Small-Angle Neutron Scattering with Solvent Contrast Variation

H. Iwase and S. Koizumi

Advanced Science Research Center, JAEA, Tokai, Ibaraki 319-1195

Red blood cells (RBCs) have a disk shape with an average thickness of 3 μm and an average diameter of 10 μm and are composed of hemoglobin, cell membranes, cytoskeletons, and glycocalyx. Except mammals, the RBC has a nucleus. The length scale of the above constituent elements widely.

Ranges from 1 nm to 10 μm. It is well-known that the hierarchical structure of RBCs has a close relation with biological functions and diseases. To reveal the correlation between the hierarchical structure and biological functions, we have investigated the hierarchical structure of the RBCs by using combined three small-angle neutron scattering (SANS) techniques; conventional pinhole SANS, focusing ultra small-angle neutron scattering (USANS) and double-crystal USANS.

In this study, we presented the results of SANS and USANS with solvent contrast variation. The solvent contrast variation method is applied in order to selectively extract the structural information of mainly components of RBC.

Chicken bloods were purchased from Nippon Biotest Laboratories Inc. The RBCs were isolated by centrifugation at 100 G for 20 min at 4 °C and washed by resuspending in 20 mM phosphate buffer containing 9 mg/ml NaCl (pH 7.2) and by centrifuging for five times at 2000 G for 10 min at 4 °C.

SANS measurements were performed on focusing USANS spectrometer SANS-J-II and on double crystal USANS on PNO at JRR-3 reactor of Japan Atomic Energy Agency, Tokai, Japan. The covered Q range is 3×10^{-5} - 3×10^{-1} Å^{-1}. SANS and USANS measurements were performed at room temperature.

Figure 1 shows scattering profiles for chicken RBC suspension in four different

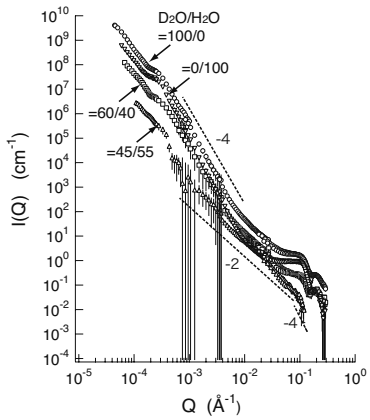

Figure 1: Scattering profiles for chicken red blood cells in 20 mM Phosphate buffer containg 9 mg/ml NaCl at pH 7.2 (D_2O/H_2O[v/v] = 100/0, 60/40, 45/55, 0/100, respectively).

D_2O/H_2O fractions (D_2O/H_2O [v/v] = 100/0, 60/40, 45/55 and 0/100, respectively). The scattering profiles of D_2O/H_2O = 100/0, 60/40 and 0/100 showed Q^{-4} behavior in the Q range from 2×10^{-4} to 1×10^{-2} Å^{-1}, which is due to interface scattering between the RBCs and solvents. The scattering profile of D_2O/H_2O = 45/55, on the other hand, has an evidently different future in comparison with these for other D_2O/H_2O fractions. The scattering profiles showed Q^{-2} behavior in the Q range from 3×10^{-4} to 8×10^{-2} Å^{-1} and obeys the power law of Q^{-4} above $Q = 8 \times 10^{-2}$ Å^{-1}. This becomes same as that of the unilamellar vesicles of lipids, because D_2O/H_2O = 45/55 is a contrast matching point of hemoglobin. All the scattering profiles were analyzed by fitting with a triple-shell disk model coupled with results obtained by optical microscopy. We were able to quantitatively determine the size of a nucleus in cytoplasm, the thickness of a cell membrane and the ratio of volume fraction between the hemoglobin and the water in the cytoplasm.

2.1.9
The Structure of 4-Repeat Tau and 3-Repeat Tau Monomer and their Self-Assembled Clusters

S. Naito[1,2], H. Mochizuki[2], T. Yasuda[2], Y. Mizuno[2], M. Furusaka[3], S. Ikeda[1], M. H. Shimizu[1], J. Suzuki[4] and S. Fujiwara[4]

[1]*KEK, Tsukuba, Ibaraki 305-0801*
[2]*Dept. of Neurol., Juntendo Univ. Sch. of Med.*
[3]*Dept. of Mech. Intell. Eng., Grad. School of Eng., Hokkaido Univ., Kita 13, Nishi 8, Kita-ku, Sapporo 060-8628*
[4]*QuBS Japan Atomic Energy Agency, Ibaraki 319-1195*

Tau is one of the microtubule-associated proteins. Mainly, 4-repeat tau (4Rtau) containing two cysteine residues and 3-repeat tau (3Rtau) lacking one repetition domain containing one cysteine residue are expressed in normal brain (Fig.1). The abnormal aggregation of tau often observed in Alzheimer ' s disease brain causes cellular degeneration and death.

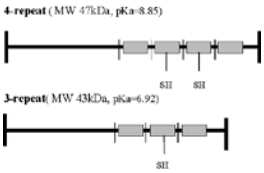

Figure 1: Diagram of 4-repeat tau and 3-repeat tau.

We prepared a tau aqueous solution suggesting the monomeric dispersion[1)] by DLS and confirmed that the conformation was unchanged if reductive atmosphere was maintained. The 4Rtau monomer and the 3Rtau one are not stable and immediately self-assemble to form huge clusters comprising several thousands of molecules. Under an oxidative environment, the cluster size of 3Rtau increased by the formation of intermolecular cystein crosslinkages.[2)] The size and shape of 4Rtau monomer and 3Rtau one are estimated from the R_h values obtained by a dynamic light scattering analysis (Table 1).
4Rtau presented a intermediary structure between globular form and random coil. 3Rtau presented almost random coil. The size and shape of 4Rtau and 3Rtau clusters are determined by SANS-J [wavelength ($\lambda = 1.14$ nm), sample distance ($L = 10$ m)] and by SWAN at KEK.

Table 1: The size and shape of 4Rtau and 3Rtau monomer

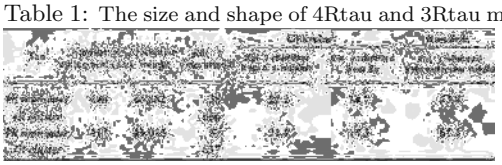

a) Radius of gyration of globular protein comprising of n amino acids , R_g, $R_g = 2.9*n^{(1/3)}$ [3)]
b) Relation between R_g and R_h (hydrodynamic radius), $R_g = 1.51*R_h$ [4)]
c) R_h of molecular weight , M, $\log(R_h) = 0.533*\log(M) - 0.682$ [5)]

4Rtau may form a rod-like rotating ellipsoid ($R_g = 850$ Å, long axis, $a = 1895$ Å and short axis, $b = c = 105.3$ Å). 3Rtau may form random coil (*slope* = -2) and the R_g was estimated to be 962 Å.

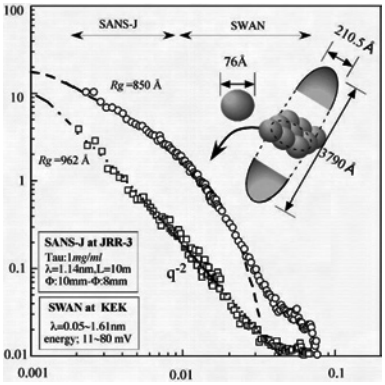

Figure 2: SANS profiles of 4Rtau and 3Rtau.

Figure 2 shows the SANS profiles of 4Rtau and 3Rtau below a concentration of C^*.

References

1) S. Naito, et al., JAERI-Review, 2005-045, 56(2005).
2) S. Naito, et al., JAEA-Review, 2007-004, 24(2007).
3) A. Gast, et al., Biochemistry, 34, 13211(1955).
4) G. Damaschun, et al., B. B. A., 1078, 289(1991).
5) Uversky. V. N., Biochemistry, 32, 13288(1993).

This is a blank page

2.2 Soft Matter

Polymer Glasses, Gel and Phase Separation

This is a blank page

2.2.1

In-situ and *Real-time* Observation of Simultaneous Living Anionic Copolymerization Process and Polymerization-Induced Self-Assembly by SANS, UV-vis, GPC and NMR

Y. Zhao, N. Miyamoto, S. Koizumi and T. Hashimoto

Advanced Science Research Center, JAEA, Tokai, Ibaraki 319-1195

We proceeded a typical simultaneous living anionic polymerization of isoprene (I) and styrene-d_8 (S) in benzene-d_6 as a solvent, with sec-buthyllithium as an initiator, into a block copolymer polyisoprene-β-polystyrene-d_8.[1] The difference of reactivity between two monomers produced the block copolymer. A specially designed combination of four techniques, including time-resolved small angle neutron scattering (SANS), UV-vis spectroscopy, gel permission chromatography (GPC) and nuclear magnetic resonance (NMR) were employed in a single batch, which enabled us to observe the real-time polymerization process and the polymerization-induced self-assembling structures during the reaction. Our results revealed three time regions, as shown in Fig.1. (I) Region 1: On one hand, the intensity of the SANS profiles keeps as a constant and no scattering peak appears, however, the molecular weight keeps increasing, it indicates that mainly homopolymerization is going on. On the other hand, UV absorbance at 450 nm, which is only sensitive to polystyryllithium living end, does not change with time, indicating that polyisoprenyllithium is dominant but that polystyryllithium is not. Therefore, in region 1, mostly polyisoprene blocks are growing. (II) Region 2: UV absorbance at 450 nm increases slowly, revealing that polystyryllithium is generated slowly with time. A broad peak shows up on the SANS profile, and the peak intensity is increasing slowly, which means that some PS segments are formed. In addition, the molecular weight of the polymer is increasing slowly. All the data demonstrates that the living chain ends start to gradually change from isoprenyllithium to styryllithium. Further NMR analysis offers reliable monomer conversions of both isoprene and styrene. The tapered structures are confirmed. (III) Region 3: All of UV absorbance, peak intensity of SANS profile and molecular weight increase significantly, denoting that PS blocks are growing rapidly. With the volume fraction of a PS block increases, polymerization-induced microphase separation is possibly occurring. Time-resolved SANS enables us to follow the morphology change as shown in Figure 2.

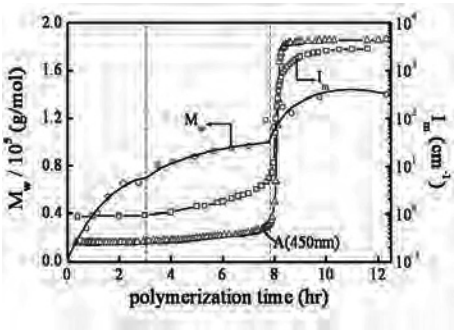

Figure 1: Three time regions defined by SANS, UV-vis and GPC.

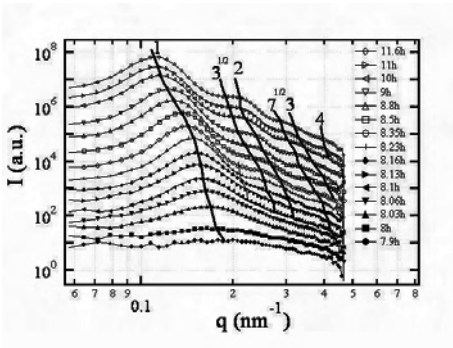

Figure 2: SANS profiles in Region 3.

References

1) K. Yamauchi, T. Hashimoto, et al., Macromolecules, 39, 4531(2006).

2.2.2
In Situ Observation of the Formation of Actin and Polycation Complexes

T. Masui[1], K. Shikinaka[2], H. J. Kwon[2], S. Koizumi[1], T. Hashimoto[1], H. Iwase[1], A. Kakugo[2] and J. P. Gong[2]

[1] *Advanced Science Research Center, JAEA, Tokai, Ibaraki 319-1195*
[2] *Graduate School of Science, Hokkaido University, Sapporo, Hokkaido 060-0810*

Actin is one of the most abundant cytoskeleton proteins in eucaryotic cell. They play a crucial role in cell motility by polymerizing monomeric globular G-actin into polymeric filamentous actin (F-actin). With actin-binding proteins (ABPs), they form higher order structures such as linear bundles, two-dimensional networks and three-dimensional gels. It has been considered that these structures are controlled by ABPs. However, a recent study has shown that the only one kind of artificial cationic polymer can form variety of structures depending its concentration and salt concentration.[1)] This system is a good model to elucidate the mechanism of regulation of actin and ABPs complex structure. Based on these backgrounds, we have investigated the effects of salt concentration on the stability and structure of actin-polycation complexes by using a small angle neutron scattering (SANS) technique.

The actin was extracted from the adductor muscle of scallops by the method of Spudich and as a model of ABPs we used an artificial cationic polymer PDMAPAA-Q. In Fig.1 we show SANS profiles from the actin and PDMAPAA-Q complexes for various KCl concentration, where the concentration of actin and polymer are kept constant. At low concentration of KCl, F-actin forms bundle structure as shown by one distinct peak at $q = 0.08$ Å^{-1}. The increase of KCl brings the peak position to lower q and sharpens its peak. By the further addition of KCl, the SANS profiles changed dramatically at KCl = 0.35 M, which means that the bundle structure disassemble to the native filamentous actin. From the first peak we estimated the repeat distance of F-actin inside the bundle d and peak width which is the measure of the orderliness of the actin alignment(Fig.2). Our result shows that the slight fluctuation of salt concentration brings dramatic change of the complex structures, which is important to regulate the motility of cell.

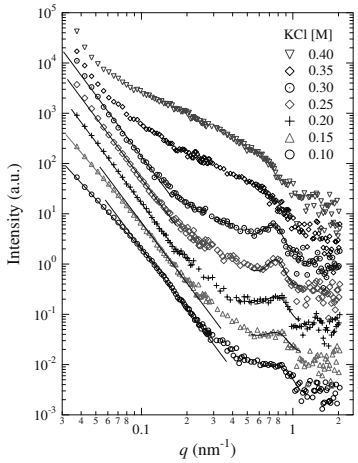

Figure 1: SANS profiles from the actin and PDMAPAA-Q complexes for various KCl concentration.

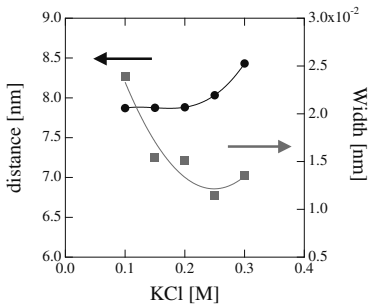

Figure 2: Repeat distance of actins inside bundles and the width of the first peak as a function of KCl concentration.

References

1) H. J. Kwon, A. Kakugo, K. Shikinaka, Y. Osada and J. P. Gong, Biomacromolecules, 6, 3005(2005).

2.2.3

Wide-q Observation of the Self-Assembled Fractal Porous Silica by Ultra-small-angle Neutron Scattering

D. Yamaguchi, H. Mayama[1], S. Koizumi, K. Tsujii[1,2] and T. Hashimoto

Advanced Science Research Center, Japan Atomic Energy Agency (JAEA), Tokai, Ibaraki 319-1195
[1]*Nanotechnology Research Center, RIES, Hokkaido University, Sapporo 001-0021*
[2]*CREST, JST, Kawaguchi, Saitama 338-8570*

The concept of fractal has been well established by the precedent studies and now we recognize that fractal structures are to be included in various natural objects, such as broccolis, branching trees, and so on. Furthermore, sometimes a fractal structure is deeply related with a specific property of the material. A super water-repellent surface made of an alkylketene dimer (AKD), which is a kind of wax, is a typically good example [1)]. When AKD forms a rough surface having a specific surface fractal dimension of $D_s = 2.3$, it shows an extremely large contact angle of 174° for water droplets as compared with the flat surface. Moreover, it is elucidated that the water-repellency largely depends on the surface dimension of D_s. Thus, to control the fractal dimension is of importance to draw favourable properties of the material.

Later on, Mayama et al. have successfully applied the self-assembled AKD particle to the synthesis of porous silica materials, which have well-controlled fractal dimensions [2)]. They utilized flaky AKD particles as a mould and formed a silica matrix by so called sol-gel method. After the solidification of the silica matrix, the original AKD mould was completely burnt away at a high temperature (650 °C) and became pores having a particular fractal dimension. The fractal dimension of the porous silica turned out to be controlled by the compression of the AKD mould at different ratios and that fact was confirmed by the real-space observation with scanning electron microscopy.

In this study, we further investigate this porous silica material by the scattering method, which brings us the following advantages: (i) to facilitate the evaluation of the fractal dimension of the materials, and (ii) to elucidate the hierarchical structure.

Two fractal porous silica specimens, which were prepared by the above sol-gel method and under different compression conditions, were employed for ultra-small-angle neutron scattering(USANS). The measurements were performed on the Bonse-Hart type double crystal diffractometer (at 3G beamport) as well as on the pinhole and focusing SANS spectrometer SANS-J-II at the research reactor JRR-3. From the resultant scattering profiles shown in Fig.1, we can discern that the different mass fractal dimensions were observed in the q-range of $q \leq 1 \times 10^{-2}$ nm^{-1} between the two specimens whose compression conditions are different.

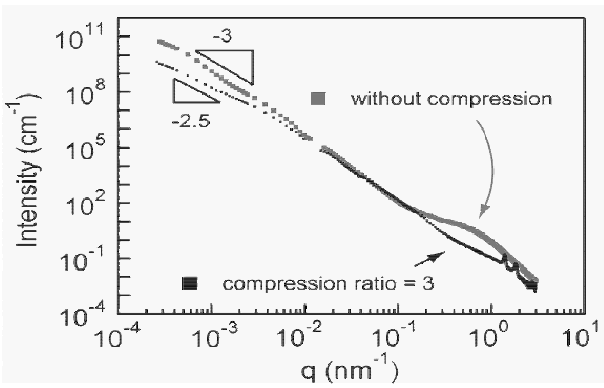

Figure 1: Wide-q scattering profiles for fractal porous silica materials.

References

1) S. Shibuichi, et al., J. Phys. Chem., 100, 19512(1996).
2) H. Mayama and K. Tsujii, J. Chem. Phys., 125, 124706(2006).

This is a blank page

2.3 Strongly Correlated Electron Systems and Superconductivity

U-compounds, Ce-compounds and Transition-metal Oxides

This is a blank page

2.3.1

Polarized Neutron Inelastic Scattering Study of Spin Fluctuation in $La_{2-x}(Sr,Ba)_xCuO_4$

S. Wakimoto, K. Kakurai, M. Takeda, M. Matsuda, M. Fujita[1], K. Yamada[1] and J.M. Tranquada[2]

Quantum Beam Science Directorate, JAEA, Tokai, Ibaraki 319-1195
[1]*Institute for Materials Research, Tohoku University, Katahira, Sendai 980-8577*
[2]*Brookhaven National Laboratory, Upton, New York 11973, USA*

The recent discovery of universal magnetic excitation in the high-T_c cuprates, which shows a novel hour-glass shape dispersion, has provided an important insight into the magnetic origin of the superconductivity. Among the several pictures proposed to explain the hour-glass dispersion, the stripe model is expected to be an important candidate. We have performed inelastic polarized neutron scattering on stripe-ordered $La_{1.875}Ba_{0.125}CuO_4$(LBCO 1/8) and compared the results with those of $La_{1.92}Sr_{0.08}CuO_4$(LSCO 8 %) which has no stripe order. The purpose of this experiment is to understand the effects of the stripe order on the low energy magnetic excitations and hence have an insight into the origin of the universal magnetic excitation.

The experiments have been performed at the TAS-1 triple axis spectrometer operated in a uniaxial polarization mode. Vertically and horizontally focused Heusler monochromator and analyzer were used. Inelastic measurements were done with a fixed final neutron energy of 14.7 meV, and a spin-flipper and a PG filter were placed after the sample.

Figure 1 shows profiles observed at the energy transfer 4 meV in the vertical-field (VF) spin-flip (SF) and the horizontal-field (HF) SF channels along the A-C trajectories shown in the bottom figure. Remarkably, it is shown that for LSCO 8 % the HF-SF signal is almost double of the VF-SF signal indicating isotropic spin fluctuations, whereas for LBCO 1/8 both the channels show comparable cross sections indicating anisotropic spin fluctuations where those along the c-axis are suppressed. We have also confirmed by the polarized neutron diffraction that the Cu spins are confined in the CuO_2 plane, that is, the $a-b$ plane, in the stripe-ordered state.

These results demonstrate that the polarization of the low energy spin fluctuation is different between the samples with and without the stripe order. A possible explanation is that the in-plane gap of the excitation which is observed in the non-doped La_2CuO_4 is recovered in the stripe-ordered sample. Further polarized and unpolarized neutron experiments are in progress to confirm this.

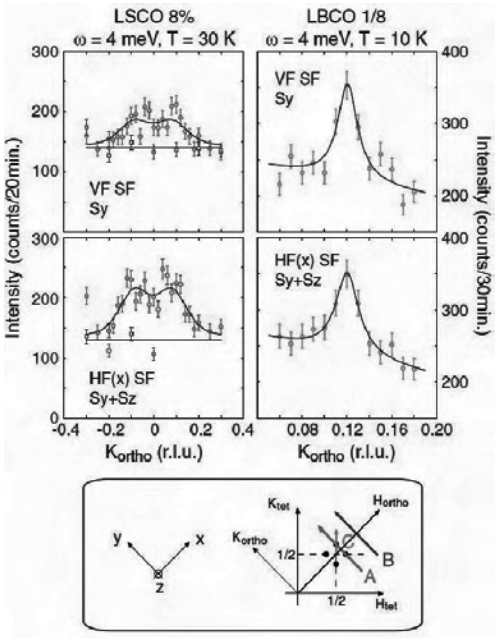

Figure 1: Polarized neutron scattering cross section at the energy transfer of 4 meV observed in the VF-SF and HF-SF channels. The data for LSCO 8 % are measured along the A (circles) and B (squares) trajectories, while those of LBCO 1/8 are measured along the C trajectory. The bottom figures show the scan trajectories in the momentum space and the definition of the polarization axes.

2.3.2
Successive Phase Transitions of $LuBaCo_4O_7$ with Kagome and Triangular Lattices

M. Soda, T. Moyoshi, Y. Yasui, M. Sato and K. Kakurai[1]

Department of Physics, Nagoya University, Furo-cho, Chikusa-ku, Nagoya 464-8602
[1]*Quantum Beam Science Directorate, JAEA, Tokai, Ibaraki 319-1195*

Spin systems on the pyrochlore, triangular and kagome lattices are well-known examples of geometrically frustrated systems and expected to exhibit various interesting properties induced by strong magnetic fluctuations. $RBaCo_4O_7$ (R = Ca, Y and rare-earth elements) is one of typical examples of such systems, because it has both triangular and kagome lattices of Co spins.[1–3)]

Magnetic, thermal and neutron diffraction measurements have been carried out on single-crystal samples of $LuBaCo_4O_7$. Anomalies of the magnetic susceptibility have been found at temperatures $T_{a1} \sim 70$ K and $T_{a2} \sim 50$ K. We have also found a second-order structural transition at $T_{c1} \sim 165$ K and a first-order structural transition at $T_{c2} \sim 105$ K (T_{c2}' ~ 80 K) with increasing (decreasing) temperature.

We have observed reflections at $\boldsymbol{Q}$-points (h'/20l) and (h'/2h'/2l) (h' = odd; *group A*) below T_{c1}, and additionally at the $\boldsymbol{Q}$-points (h"/3$\pm\delta h$"/3$\pm\delta l$) (h"/3 = noninteger number; *group B*) below T_{c2}, in the reciprocal space of the hexagonal unit cell ($a = b \sim 6.27$ Å, $c \sim 10.24$ Å). We have found that at $T < T_{c2}$, the line shapes of the reflections at the $\boldsymbol{Q}$-points of *group A* can be described by Lorentzian-type ones, while at $T_{c2} < T < T_{c1}$, they have Gaussian-type ones. From the $|\boldsymbol{Q}|$-dependence of the integrated intensities, the Gaussian and Lorentzian components can be regarded as nuclear and magnetic origins, respectively. The magnetic (Lorentzian) component is dominant below T_{c2} and only the nuclear (Gaussian) component exists at T between T_{c2} and T_{c1}. For the reflections at the $\boldsymbol{Q}$-points of *group B*, the δ value is T-dependent. These reflections have broad Lorentzian profiles and can be considered to be magnetic.

Below T_{c2}, we can easily find that the intensities of the nuclear superlattice reflections are almost zero and the intensities of the magnetic reflections increase gradually with decreasing T. The profile shape of the magnetic peaks indicates that the magnetic correlation is not long-ranged even at 10 K, and the magnetic correlation length is estimated to be $\xi \sim 100$ Å. From the magnetic structure analyses, the magnetic reflections at the $\boldsymbol{Q}$-points of *groups A* and *B* can be considered to originate from the moments on the kagome and triangular lattices, respectively.

For both $YBaCo_4O_7$ and $LuBaCo_4O_7$ systems, the Co moments of the kagome and triangular lattices exhibit short-range orders with different magnetic periods.[2)] However, several differences have been found between the behaviors of the magnetic reflections of $YBaCo_4O_7$ and $LuBaCo_4O_7$. In $YBaCo_4O_7$, the growth of the magnetic correlation and a similar structural distortion were found to appear simultaneously at its T_{c1} (~ 105 K) with decreasing T, whereas in $LuBaCo_4O_7$, the short-range magnetic correlation grows only below T_{c2}. The periods of the magnetic modulation of the triangular lattice are also different between these two systems. At low temperatures, the structural distortion of $LuBaCo_4O_7$ system is different from that of $YBaCo_4O_7$, which induces the significant differences in the magnetic properties between these two systems.

References

1) M. Valldor, et al., Solid State Sci., 4, 923 (2002).
2) M. Soda, et al., JPSJ., 75, 054707(2006).
3) M. Soda, et al., JPSJ., 76, 084701(2007).

2.3.3

Magnetic Excitations in Lightly-Doped $La_{2-x}Sr_xCuO_4$

M. Matsuda, S. Wakimoto, M. Fujita[1], K. Yamada[1] and J. M. Tranquada[2]

Quantum Beam Science Directorate, Japan Atomic Energy Agency, Tokai, Ibaraki 319-1195
[1] *Institute for Materials Research, Tohoku University, Sendai 980-8577*
[2] *Physics Department, Brookhaven National Laboratory, Upton, NY 11973, USA.*

Recently, detailed inelastic neutron scattering studies have been performed up to high energies in various systems such as $YBa_2Cu_3O_{6.6}$,[1] $La_{1.875}Ba_{0.125}CuO_4$[2] and $La_{1.84}Sr_{0.16}CuO_4$.[3] All of them show hourglass-shaped magnetic excitations with the parallel incommensurate correlations at low energies. On the other hand, there are few studies of magnetic excitations in the diagonal incommensurate phase in lightly-doped $La_{2-x}Sr_xCuO_4$, although conventional spin wave excitations were reported in the diagonal stripe phase of $La_{2-x}Sr_xNiO_4$.[4] We previously tried to measure magnetic excitations in the diagonal incommensurate phase using a twinned crystal of $La_{1.976}Sr_{0.024}CuO_4$.[5] The results suggest that the magnetic correlations change from being incommensurate to commensurate at $\sim$ 7 meV and $\sim$ 70 K. However, since some the assumptions are needed to analyze the data in twinned crystal, information was limited. It is important to compare the magnetic excitatons in both the parallel and diagonal incommensurate phases in detail to clarify what is the intrinsic magnetic properties in the superconducting phase.

We performed inelastic neutron scattering measurements on TAS-2 and LTAS using an almost untwinned crystal of $La_{2-x}Sr_xCuO_4$ ($x \sim 0.04$), in which elastic magnetic peaks are observed at $(1, \pm\delta, 0)_{\rm ortho}$ or $(0, 1\pm\delta, 0)_{\rm ortho}$, to observe magnetic excitations in the diagonal incommensurate phase. We observed energy and temperature dependences of magnetic excitations in the range of $0 \leq \omega \leq 12$ meV and $4 \leq$ T ≤ 290 K. The results show that the incommensurability (δ) decreases gradually with increasing energy up to 12 meV, as shown in Fig. 1. This is qualitatively consistent with the behavior in the parallel incommensurate phase. The temperature dependence of the magnetic excitations shows that the incommensurability gradually decreases with increasing temperature and becomes almost commensurate below 12 meV at room temperature.

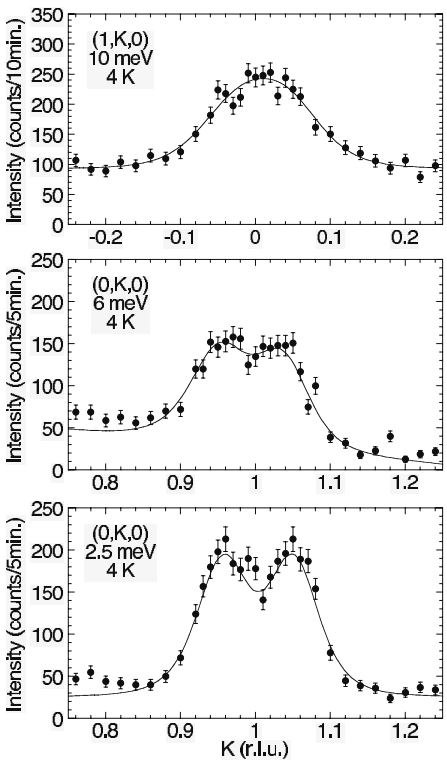

Figure 1: Typical consant-energy spectra at $T = 4$ K in $La_{2-x}Sr_xCuO_4$ ($x \sim 0.04$). The diagonal incommensurate peaks are observed at $(1, \pm\delta, 0)$ or $(0, 1\pm\delta, 0)$.

References

1) S. M. Hayden, et al., Nature, 429, 531(2004).
2) J. M. Tranquada, et al., Nature, 429, 534(2004).
3) S. M. Hayden, et al., Nature Phys., 3, 163(2007).
4) P. Bourges, et al., Phys. Rev. Lett., 90, 147202(2003).
5) M. Matsuda, et al., Phys. Rev. B, 62, 9148(2000).

2.3.4
New-Type Phase Transition of Honeycomb Lattice System Li_2RuO_3

Y. Miura, Y. Yasui, M. Sato, N. Igawa[1] and K. Kakurai[1]

Department of Physics, Nagoya University, Furo-cho, Chikusa-ku, Nagoya 464-8602
[1]*Quantum Beam Science Directorate, JAEA, Tokai, Ibaraki 319-1195*

Li_2RuO_3 has layers of the honeycomb lattice of edge-sharing RuO_6 octahedra with a LiO_6 octahedron at the corner of each hexagon of RuO_6. The Ru valence is +4 and the four electrons exist in the $4d$ t_{2g} orbits. Li atom layers are between the honeycomb layers. For this system, we have found a phase transition at temperature $T = T_c \sim 540$ K.[1)] With decreasing T, the electrical resistivity exhibits an anomalous increase at T_c, suggesting the "metal-to-insulator"-like transition, and the magnetic susceptibility also shows a sharp decrease.

To clarify the mechanism of the transition, powder neutron diffraction measurements were carried out at room temperature (RT) and 600 K using a high resolution powder diffractometer (HRPD) installed at JRR-3 of JAEA in Tokai, and Rietveld analyses were carried out using RIETAN-2000. Although the space group at RT was previously reported to be $C2/c$[2,3)], several superlattice peaks which cannot be explained by $C2/c$ were observed. To reproduce these reflections, we adopt the space group $P2_1/m$. The result of the Rietveld fitting with $P2_1/m$ is rather well. As the possible space group at 600 K, we have adopted $C2/m$, the minimal non-isomorphic supergroup of $P2_1/m$, because this space group allows the second-order transition at T_c. (From the experimental data, it is not easy to definitely distinguish if it is the second-order one or the first-order one.)

At 600 K, Ru atoms form an almost ideal honeycomb structure. At RT, a significant reduction (by $\sim$ 13 %) of the bond lengths was found between two of the six Ru-Ru pairs of the hexagon (figure (right panel)). To answer why such drastic changes take place, we consider the coupling of the lattice distortion with the formation of the molecular orbits of the t_{2g} electrons of Ru^{4+}-Ru^{4+} of edge sharing RuO_6 octahedra. The energy levels of the bonding and corresponding antibonding orbits are shown in the Figure 1(right), where we can see that the nonmagnetic electron configuration is realized below T_c.

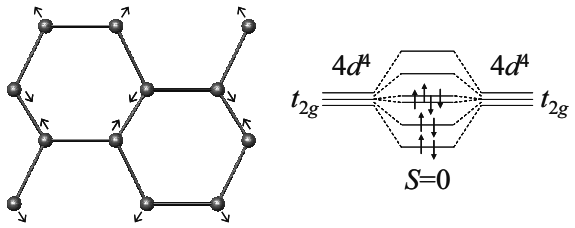

Figure 1: The distortion pattern of Ru-honeycomb skeleton at RT (left) and the energy levels of the molecular orbits of Ru^{4+}-Ru^{4+} pairs (right) below T_c. The electrons in these levels are shown by the arrows presenting the spin directions.

Although transitions accompanied with the significant anomalies of the electrical resistivity and the magnetic susceptibility similar to those of the present system have been reported for $La_4Ru_2O_{10}$ with corner-sharing RuO_6 octahedra and for $Tl_2Ru_2O_7$ with a pyrochlore structure, their microscopic mechanisms are different from that presently proposed. Li_2RuO_3 with edge-sharing RuO_6 octahedra is considered to present, as far as we know, a new type of phase transitions associated with the structural distortion induced by the molecular-orbit formation of the d electron states.

References

1) Y. Miura, et al., J. Phys. Soc. Jpn., 76, 033705 (2007).
2) J. F. Durac, C. R. Acad. Sc. Paris Ser. B, 270, 223(1970).
3) A. C. W. P. James and J. B. Goodenough, J. Solid State Chem., 74, 287(1988).

2.3.5

Direct Observation of the Pressure-Induced Ferromagnetic Order in Valence Transition Material $YbInCu_4$

T. Osakabe, K. Kojima[1] and K. Hiraoka[2]

Quantum Beam Science Directorate, JAEA, Tokai, Ibaraki 319-1195
[1] *Graduate School of Integrated Arts and Sciences, Hiroshima University, Higashi-Hiroshima 739-8571*
[2] *Graduate School of Science and Enigineering, Ehime University, Matsuyama 790-8577*

$YbInCu_4$ crystallizes in the cubic $AuBe_5$ (C15b)-type structure. At ambient pressure with decreasing temperature, the compound undergoes the first-order isomorphic valence transition at $T_V = 42$ K with the increase of the unit-cell volume of about 0.5 %. At T_V, the 4f states of Yb ions change from high temperature (HT) well-localized states of Yb^{3+} to low temperature (LT) mixed-valent states of $Yb^{2.9+}$. Recent studies under high pressures have revealed that the nonmagnetic LT phase is completely suppressed and the magnetic HT phase is stabilized in all temperature ranges above $P_C = 2.5$ GPa. Furthermore, it is suggested that the long-range magnetic order appears below $T_C = 2.4$ K at 2.5 GPa.[1] On the other hand, this compound shows the superconductivity above 0.7 GPa below 1.4 K. This pressure-induced superconductivity survives up to 4 GPa.[2] The purpose of our work is to elucidate directly and microscopically the pressure-induced magnetic order. We performed high-pressure neutron diffraction experiments using the triple-axis spectrometer TAS-1. The high-pressure was generated up to 6.2 GPa by a newly-developed hybrid-anvil device.[3] The pressure transmitted by the glycerin medium was hydrostatic even at 7.0 GPa. The sample size was about $1.0 \times 0.5 \times 0.25$ mm^3. The pressure was applied along the $[01\bar{1}]$ direction of the sample and the diffraction plane was the [100]-[011] one. We used a neutron focusing device in order to increase the effective neutron intensity at the sample position.[4]

We have successfully observed the distinct increase of the intensities only at the ferromagnetic $(\bar{1}11)$ or $(\bar{1}\bar{1}\bar{1})$ reciprocal lattice points below about $T_C = 2.5$ K at 4.0 GPa and 6.2 GPa. As an example, we show the temperature dependence of the intensities at 6.2 GPa in Fig. 1. This result indicates that the ferromagnetic order appears at least above 4.0 GPa and T_C is hardly affected by the pressure. On the other hand, the estimated magnetic moment in the ferromagnetic order is about 0.68 μ_B and 0.76 μ_B per Yb ion at 4.0 and 6.2 GPa, respectively. These values are quite large compared to the Y-diluted system $Yb_{0.8}Y_{0.2}InCu_4$, which shows the weak ferromagnetic order of 0.05 μ_B per Yb ion below $T_C = 1.7$ K and above 0.8 GPa.[5]

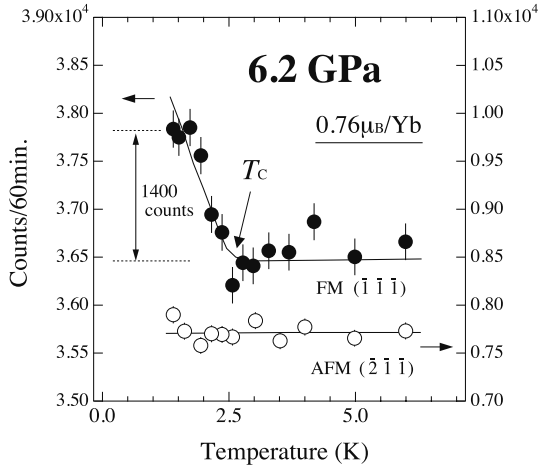

Figure 1: Temperature dependence of the intensities at the $(\bar{1}\bar{1}\bar{1})$ ferromagnetic point and at the $(\bar{2}\bar{1}\bar{1})$ antiferromagnetic point for $P = 6.2$ GPa.

References

1) T. Mito, et al., Phys. Rev. B, 67, 224409(2003).
2) M. Hedo, et al., Acta Phys. Polonica B, 34, 1193(2003).
3) T. Osakabe, et al., J. Magn. Magn. Mat., 310, 2725(2007).
4) T. Osakabe, et al., Rev. Sci. Instrum., 76, 073102(2005).
5) A. Mitsuda, et al., Phys. Rev. Lett., 88, 137204(2002).

2.3.6

Magnetic Structure of $TbRhIn_5$

T. Sugai[1,2], F. Mizuno[1,2], N. Metoki[1,2], Y. Haga[1,2], N. V. Hieu[3], T.Takeuchi[3], K. Sugiyama[3], R.Settai[3] and Y. Onuki[1,3]

[1] *Advanced Science Research Center, JAEA, Tokai, Ibaraki 319-1195*
[2] *Department of Physics, Tohoku University, Sendai 980-8587*
[3] *Graduate School of Science, Osaka University, Toyonaka 560-0043*

Intermetallic compounds ATX_5 (A: Lanthanoid or Actinide, T: Transition metal, X: In or Ga) with the tetragonal $HoCoGa_5$-type (P4/mmm) crystal structure, so called "115", attract strong interest because of the heavy fermion superconductivity in Ce-115 and Pu-115 or various magnetic structures in U-115 and Np-115. On the other hand, $RRhIn_5$ (R: Nd, Tb, Dy, Ho)[1)] are local antiferromagnets. The magnetic susceptibility shows Curie-Weiss behaviour, where the Néel temperatures are in good agreement with de Gennes factor. A similar two-step metamagnetic transition is observed in $RRhIn_5$ (R: Nd, Tb, Dy, Ho), when the magnetic field is applied along the c-axis (easy axis). We performed neutron scattering experiment in order to determine the magnetic structure of $TbRhIn_5$. We used triple-axis spectrometers LTAS and MUSASI (low angle beam port) installed in JRR-3 guide hall.

Figure.1 shows the longitudinal scan profile of the (1/2 0 1/2) antiferromagnetic reflection at 2.8 K, which disappeared at 50 K above Neel temperature. Inset shows the temperature dependence of (1/2 0 1/2) peak intensity. We estimated the Neel temperature T_N to be approximately 47.3 K. This value is consistent with the susceptibility measurement.

Figure.2 shows the magnetic structure for $TbRhIn_5$, determined from the comparison of the integrated intensity of the antiferromagnetic reflections on the (h 0 l) plane with model calculations. Tb magnetic moments are parallel to the c-axis and order with a propagating vector $Q = (1/2\ 0\ 1/2)$. The moment direction is consistent with the susceptibility study, when the c-axis is the easy axis. We also confirmed the magnetic structure for $RRhIn_5$ (R: Nd, Dy, Ho). The obtained magnetic moment $\mu = 7.7\ \mu_B$/Tb is consistent with $gJ = 9\ \mu_B$/Tb. Relatively large error is most likely due to the strong absorption of In with a large sample size with 4 mm length.

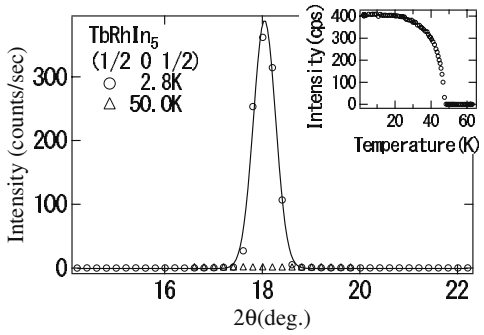

Figure 1: The (1/2 0 1/2) antiferromagnetic reflection. Inset is the temperature dependence of the peak intensity.

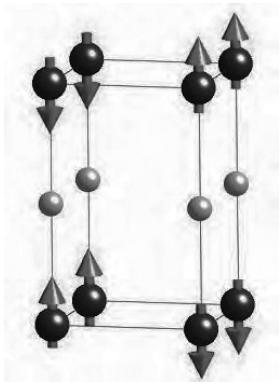

Figure 2: The magnetic structure of $TbRhIn_5$.

References

1) H. V.Hieu, et al., J. Phys. Soc. Jpn., 75, 074708(2006).

2.3.7
Magnetic Structure of $TbMnO_3$ Studied with Spherical Neutron Polarimetry

R. Kajimoto, M. Matsuda, M. Takeda, K. Kakurai, Y. Mitsui[1], H. Yoshizawa[1], T. Kimura[2] and Y. Tokura[3]

Quantum Beam Science Directorate, JAEA, Tokai, Ibaraki 319-1195
[1] *Neutron Science Laboratory, ISSP, University of Tokyo, Tokai, Ibaraki 319-1106*
[2] *Bell Laboratories, Lucent Technologies, Murray Hill, New Jersey 07974, USA*
[3] *Department of Applied Physics, University of Tokyo, Bunkyo-ku, Tokyo 113-8656*

$TbMnO_3$ shows a collinear sinusoidal spin ordering below $T_N = 42$ K, where the spins point to the b axis and modulate along the b axis with a wave number $q \sim 0.28b^*$. The spin structure is transformed into a cycloidal spiral structure below $T_C = 28$ K, where the spins rotate within the bc plane. The component along the c axis of the spiral structure is shorter than that along the b axis, which results in an elliptically distorted spiral structure[1)]. Recently, it has been found that $TbMnO_3$ as well as some other isostructural manganites shows a ferroelectric transition at T_C, and that its dielectric properties are strongly coupled with its magnetism[2)].

In the present study, we conducted a detailed study on the change in the spin structure in $TbMnO_3$ using the spherical neutron polarimetry technique, which should shed light on the origin of the ferroelectricity. Polarized neutron diffraction measurements were carried out using CRYOPAD installed on TAS-1 spectrometer with the incident neutron energies 14.7 meV and 34 meV.

Polarization of the scattered neutron beam was determined as $P_{if} = (I_{+i,+f} - I_{+i,-f})/(I_{+i,+f}+I_{+i,-f})$, where $I_{i,f}$ represents the scattering intensity with initial and final polarizations i and f, respectively. Figure 1 shows temperature (T) dependences of P_{yx}, P_{zx}, $(P_{yy}^2+P_{yz}^2)^{\frac{1}{2}}$, and $(P_{zy}^2+P_{zz}^2)^{\frac{1}{2}}$ at a magnetic Bragg point $(4, q, 1)$. In the present measurement condition, P_{yx} and P_{zx} reflect the chirality of the spiral spin structure. Because they are nearly equal to zero even at $T < T_C$, two chirality domains with clockwise and anticlockwise chiralities are distributed equally in the spiral phase.

On the other hand, $P_{yy}^2+P_{yz}^2$ and $P_{zy}^2+P_{zz}^2$ will become unity for a collinear spin structure, while it will become zero for an ideal spiral structure. In Fig. 1, they are nearly equal to unity at $T_C < T < T_N$. They gradually decrease below T_C as a function of T, but they saturate around 15 K and do not seem to reach zero at $T = 0$ K. These results indicate that the collinear spin structure in $TbMnO_3$ is transformed into a spiral structure below T_C by gradually swelling the c component with decreasing T. The transformation into the spiral structure is incomplete at the lowest temperature, resulting in the elliptical spiral structure. The T dependences of $P_{yy}^2 + P_{yz}^2$ and $P_{zy}^2 + P_{zz}^2$ bear a strong resemblance to that of the spontaneous electric polarization P_e, which develops below T_C[2)], suggesting a strong coupling between P_e and the spiral spin ordering.

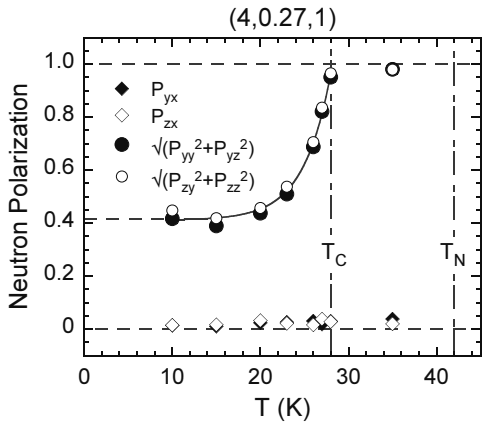

Figure 1: Temperature dependences of neutron polarizations measured at a magnetic Bragg point $(4, q, 1)$.

References

1) M. Kenzelmann, et al., Phys. Rev. Lett., 95, 087206(2005).
2) T. Kimura, et al., Nature(London), 426, 55(2003).

2.3.8
Unusual Magnetic Structure and the Successive Transition in $NpFeGa_5$

N. Metoki[1,2], F. Honda[1], S. Jonen[1], K. Kaneko[1], T. Sugai[1,2], F. Mizuno[1,2], G. H. Lander[3], D. Aoki[4], Y. Homma[4] and Y. Shiokawa[4]

[1] *Advanced Science Research Center, JAEA, Tokai, Ibaraki 319-1195*
[2] *Department of Physics, Tohoku University, Sendai 980-8578*
[3] *EC-JRC, Institute for Transuranium Elements, Postfach 2340, D-76125 Karlsruhe, Germany*
[4] *Institute for Materials Research, Tohoku University, Oarai, Ibaraki 311-1313*

$NpFeGa_5$ exhibits a successive magnetic transition at $T_{N1} = 118\,K$ and $T_{N2} = 75\,K$.[1)] Our recent study revealed the c-type antiferromagnetic order with $\boldsymbol{q} = (1/2\,1/2\,0)$ below T_{N1}. The strong and weak intensities of $(1/2\,1/2\,l)$ with l odd or even, respectively, indicate the Fe sublattice ordering with the same structure as in the Np sublattice, but the opposite moment direction in a chemical unit cell. We observed an anomaly in the temperature dependence of the antiferromagnetic intensity around T_{N2}. Spin polarization analysis has been carried out in order to clarify the double transition in $NpFeGa_5$, which is an iso-structural compound of heavy fermion superconductors Ce115 and Pu115.

Figure 1 shows the result of the temperature dependence for the spin-flip (SF) and non-spin-flip (NSF) scattering cross-section of the $(1/2\,1/2\,0)$ reflection with the c-axis of the sample and the guide field for the neutron spin state being perpendicular to the scattering plane. The magnetic moment perpendicular to the c-axis and the scattering vector $\boldsymbol{Q} = [1/2\,1/2\,0]$ provides the SF cross-section, whereas the NSF scattering cross-section represents the squared moment parallel to the c-axis. The SF scattering cross-section was observed at all temperatures below T_{N1} with a weak anomaly at T_{N2}. On the other hand, a clear NSF signal was observed only below T_{N2}. These experimental results indicate unambiguously that the magnetic moment is in the basal plane for $T_{N2} < T < T_{N1}$, while the moment is inclined for $T < T_{N2}$.

Figure 2 shows the magnetic structure of $NpFeGa_5$ both for high and low temperature phases. Our analysis revealed that $NpFeGa_5$ keeps a collinear structure with a moment inclination angle about 25 degrees from the basal plane. The result of the scattering intensity of the unpolarized diffraction experiment is well reproduced from the model calculation based on the magnetic structures in Fig.2. The magnetic moment at the base temperature would be 0.8 Bohr magneton per Np and 0.3 Bohr magneton per Fe atom, respectively.

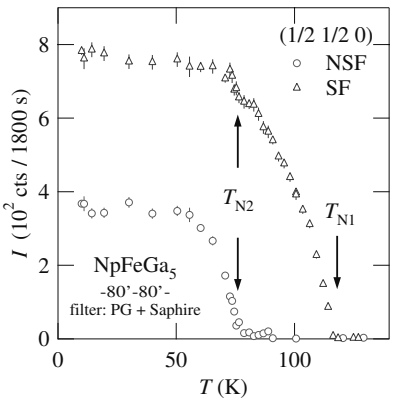

Figure 1: Temperature dependence of the spin-flip (SF) and non-spin-flip (NSF) scattering cross-section of the $(1/2\,1/2\,l)$ reflection in $NpFeGa_5$.

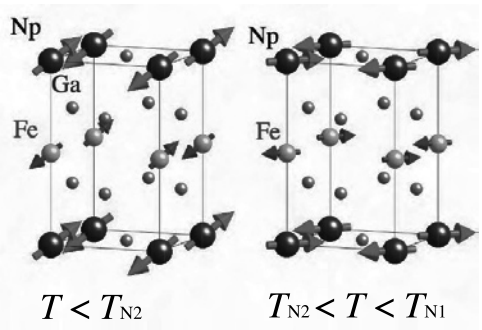

Figure 2: Magnetic structures of $NpFeGa_5$.

References

1) D. Aoki, et al., J. Phys. Soc. Jpn., 74, 2323(2005).

2.3.9
Coulomb Interaction in $NpCoGa_5$ Probing through Phonon Spectroscopy

K. Kaneko[1], N. Metoki[1,2], S. Raymond[3], J.-P. Sanchez[3], P. Piekarz[4], K. Parlinski[4], A. M. Oleś[4,5], D. Aoki[6], Y. Homma[6], Y. Shiokawa[1,6], S. Ikeda[1], T. D. Matsuda[1], Y. Haga[1,2], Y. Ōnuki[1,7] and G. H. Lander[1,8]

[1] *Advanced Science Research Center, JAEA, Tokai, Naka, Ibraki 319-1195*
[2] *Department of Physics, Tohoku University, Sendai 980-8578*
[3] *DRFMC-CEA, 38054 Grenoble, France*
[4] *Institute of Nuclear Physics, Polish Academy of Sciences, 31-342 Kraków, Poland*
[5] *Max-Planck-Institut für Festkörperforschung, Heisenbergerstrasse 1, D-70569 Stuttgart, Germany*
[6] *Institute for Materials Research, Tohoku University, Oarai, Ibaraki 311-1313*
[7] *Graduate School of Science, Osaka University, Toyonaka, Osaka 560-0043*
[8] *EC-JRC, Institute for Transuranium Elements, Postfach 2340, D-76125 Karlsruhe, Germany*

The discovery of superconductivity in the $PuTGa_5$ system attracts an considerable interest with its relatively high T_{sc}[1,2]. The overall features including the NMR studies support the idea of magnetically mediated superconductivity in $PuTGa_5$[3,4]. However, the importance of phonons on the pairing cannot be ruled out at present as in the case of high-T_c cuprate. Furthermore, the phonon spectroscopy with the *ab initio* lattice dynamics calculation offers an ability to probe electronic properties[5,6]. So far, we studied the phonons in an itinerant paramagnet $UCoGa_5$ as well as $PuCoGa_5$, and revealed that the results are compatible with the presence of a local Coulomb repulsion U between f electrons in $PuCoGa_5$ whereas a purely itinerant approach with U=0 agrees well in $UCoGa_5$[6,7]. In order to obtain the deeper understanding on the f-electron state in A-115, we measured phonons in the isostructural itinerant antiferromagnet $NpCoGa_5$.

Figure 1 shows the representative results of the neutron inelastic scattering spectra along the Γ-Z line at room temperature. Clear peaks corresponding to transverse acoustic (TA) and transverse optic (TO) phonons were observed as shown in Fig. 1(a). The obtained phonon dispersion relation along the Γ-Z line of $NpCoGa_5$ together with those of $UCoGa_5$, $PuCoGa_5$ and theoretical calculations at room temperature are summarized in Fig. 1(b). Note that the TO mode of $NpCoGa_5$ (△) shows a lower energy than that of $UCoGa_5$ (●)[7], and higher than that of

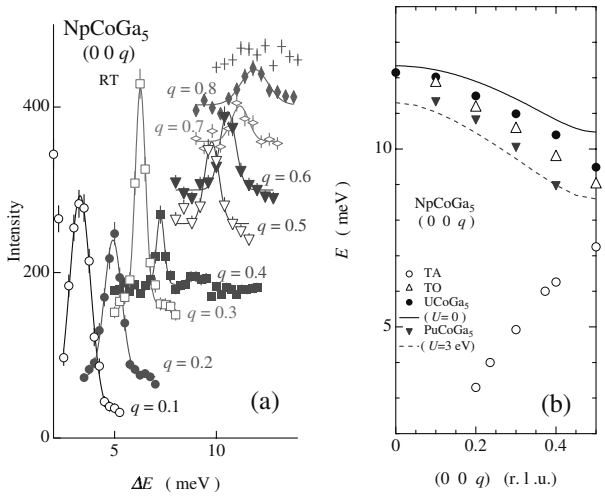

Figure 1: (a) Neutron inelastic scattering spectra of $NpCoGa_5$ at room temperature. (b) The obtained phonon dispersions of $NpCoGa_5$, $UCoGa_5$[7] and $PuCoGa_5$[6] along Γ-Z at room temperature. The lines show the result of calculation with U=0 and 3 eV for $UCoGa_5$ and $PuCoGa_5$, respectively.[6,7]

$PuCoGa_5$ (▼)[6]. This tendency qualitatively agrees with the itinerancy of 5f-electrons in an A-115 system: the strong itinerant character of U-115 and rather magnetic in Np-115. Theoretical calculation on $NpCoGa_5$ are now in progress.

References

1) J.L. Sarrao, et al., Nature (London), 420, 297(2002).
2) F. Wastin, et al., J. Phys. Condens. Matter., 15, S2279(2003).
3) N.J. Curro, et al., Nature (London), 434, 622(2005).
4) H. Sakai, et al., J. Phys. Soc. Jpn., 74, 1710(2005).
5) P. Piekarz, et al., Phys. Rev. B, 72, 014521(2005).
6) S. Raymond, et al., Phys. Rev. Lett., 96, 237003(2006).
7) N. Metoki, et al., Physica B, 378-380B, 1003(2006).

This is a blank page

2.4 Magnetism and Low Temperature Physics

Low Dimension, Frustration, Magnetic Transitions and Quantum Liquids

This is a blank page

2.4.1
Magnetic Excitation in the Spin-1/2 Trimer Chain Compound $Cu_3(P_2O_6OD)_2$ †

M. Hase, M. Matsuda[1], K. Kakurai[1], K. Ozawa, H. Kitazawa,
N. Tsujii, A. Dönni, M. Kohno and X. Hu

National Institute for Materials Science (NIMS), 1-2-1 Sengen, Tsukuba, Ibaraki 305-0047
[1]*Japan Atomic Energy Agency (JAEA), 2-4 Shirakata Shirane, Tokai, Naka, Ibaraki 319-1195*

$Cu_3(P_2O_6OH)_2$ shows a 1/3 magnetization plateau which indicates the existence of a gap in the magnetic excitation spectrum[1)]. As shown in the lower inset of Fig. 1, two Cu^{2+}ion sites (Cu1 and Cu2) exist and form a spin-1/2 trimer chain with $J_1 - J_2 - J_2$ interactions, where J_1 and J_2 denote two antiferromagnetic (AF) exchange interaction parameters. The values of J_1 and J_2 were evaluated as 95 K and 28 K, respectively, from magnetizations[1)]. The J_1 interaction is dominant. It is expected that the main origin of the gap is the singlet-triplet excitation of the AF dimer formed by the J_1 interaction. Accordingly, we performed inelastic neutron scattering (INS) measurements to study the gap in a deuterated $Cu_3(P_2O_6OD)_2$ powder sample.

We synthesized a crystalline powder of $Cu_3(P_2O_6OD)_2$ from a mixture of CuO and D_3PO_4-D_2O[2)]. INS measurements were carried out on the thermal neutron triple-axis spectrometer TAS-2 installed at JRR-3 at the Japan Atomic Energy Agency. The final neutron energy was fixed at 13.7 meV. The horizontal collimator sequence was guide-80'-sample-80'-open.

The open circles in the upper inset of Fig. 1 show a constant-Q scan spectrum taken at a scattering vector of $Q = 1.3$ Å^{-1} and a temperature of $T = 5.1$ K. A well-defined symmetric inelastic peak is observed at $\omega = 9.8$ meV. The solid line is a Gaussian curve plus a background and reproduces well the experimental spectrum. The peak position is practically independent of Q, but the intensity of the excitation decreases with increasing Q (not shown). The dotted line indicates the energy resolution profile. The observed width in $Cu_3(P_2O_6OD)_2$ is slightly larger than the experimental resolution.

The circles in Fig. 1 represent the temperature dependence of the energy-integrated intensity of the 9.8 meV (114 K) peak. On heating, the integrated intensity decreases slowly at low T and rapidly above 40 K, and levels off at higher T. We compare the experimental result with the isolated AF dimer model. The T dependence of the intensity is proportional to $1/[1 + 3\exp(-\Delta/T)]$, where Δ is a gap. The solid line in Fig. 1 indicates the calculated curve and is consistent with the experimental results. We obtained $J_1 = 111$ K and $J_2 = 30$ K, which reproduced the gap value as well as the magnetization.

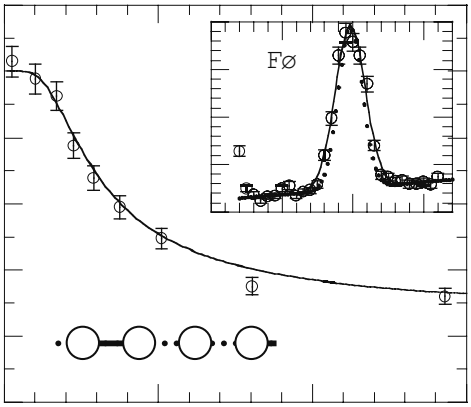

Figure 1: Temperature dependence of the integrated intensity of the 9.8 meV peak (circles). The upper and lower inset show the constant-Q scan spectrum (counts/about 5 min) and a schematic spin system, respectively.

References

1) M. Hase, et al., Phys. Rev. B, 73, 104419(2006).
2) R. Baies, et al., Inorg. chem., 44, 2376(2005).

† Common use program of JAEA

2.4.2
Polarized Neutron Inelastic Scattering Study of Central Mode in $TlCoCl_3$

A. Oosawa, K. Kakurai[1], Y. Nishiwaki[2] and T. Kato[3]

Department of Physics, Sophia University, 7-1 Kioi-cho, Chiyoda-ku, Tokyo 102-8554
[1]*Quantum Beam Science Directorate, Japan Atomic Energy Agency, Tokai, Ibaraki 319-1195*
[2]*Department of Physics, Tokyo Women's Medical University, Shinjuku-ku, Tokyo 162-8666*
[3]*Faculty of Education, Chiba University, 1-33 Yayoi-cho, Inage-ku, Chiba 273-8522*

In this study, we carried out the polarized neutron inelastic scattering experiments for the central mode using the same procedure as that in the previous experiments for the spin-wave excitation continuum performed in the previous year[1,2] in $TlCoCl_3$. In contrast to the spin-wave excitation continuum, the intensity of the central mode increases with increasing temperature because the origin of the mode is thermally excited domain walls[3]. Figure 1 shows the profile of constant-$\boldsymbol{Q}$ energy scans of $TlCoCl_3$ for non-spin-flip (NSF) scattering in the vertical field (VF) and horizontal field (HF) configurations at $\boldsymbol{Q}$ = (1.45, 1.45, 0.6) for T = 10 and 61 K. As shown in Fig. 1, we can clearly see that the intensity of the central mode in the vicinity of $E = 3$ meV increases with increasing temperature. Each polarized neutron inelastic scattering intensity in the NSF channel in the VF and HF configurations for the scattering (h, h, l)-plane is expressed as the following equations, respectively[4],

$$I_{\mathrm{NSF,VF}} = C \cdot S_{xx}(\boldsymbol{Q}, \omega) + I_{\mathrm{nonmag}}, \quad (1)$$
$$I_{\mathrm{NSF,HF}} = I_{\mathrm{nonmag}}. \quad (2)$$

where $S_{xx}(\boldsymbol{Q}, \omega)$ and I_{nonmag} are the transverse magnetic fluctuation and the non-magnetic fluctuation, respectively. Hence $S_{xx}(\boldsymbol{Q}, \omega)$ can be extracted from the difference between $I_{\mathrm{NSF,VF}}$ and $I_{\mathrm{NSF,HF}}$. As shown in Fig. 1, no remarkable difference between $I_{\mathrm{NSF,VF}}$ and $I_{\mathrm{NSF,HF}}$ at $T = 61$ K can be seen, indicating that $S_{xx}(\boldsymbol{Q}, \omega)$ is hardly included in the central mode of $TlCoCl_3$. While, significant difference between $I_{\mathrm{NSF,VF}}$ at $T = 10$ K and that at $T = 61$ K is seen. This result indicates that the non-magnetic fluctuations including the phonons are enhanced with increasing temperature. In the previous unpolarized neutron inelastic scattering experiments of $CsCoCl_3$[3], finite intensity of $S_{xx}(\boldsymbol{Q}, \omega)$ in the central mode has been concluded from the difference between the intensity at low temperature and that at high temperature. However, the present result in $TlCoCl_3$ indicates that the difference observed in the previous unpolarized experiments of $CsCoCl_3$ is not due to the existence of $S_{xx}(\boldsymbol{Q}, \omega)$ in the central mode, but the non-magnetic fluctuations such as phonons. While, for the longitudinal magnetic fluctuation $S_{zz}(\boldsymbol{Q}, \omega)$, a finite intensity was observed in the central mode of $TlCoCl_3$, the same as $CsCoCl_3$ (not shown).

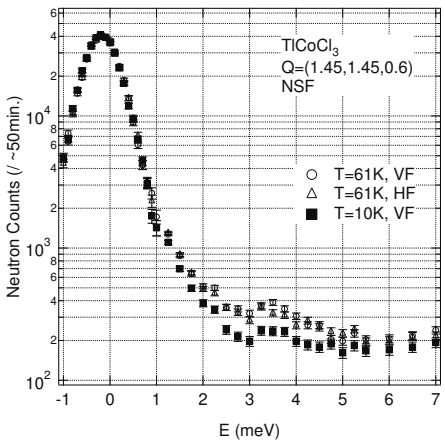

Figure 1: Profiles of constant-$\boldsymbol{Q}$ energy scans of $TlCoCl_3$ for NSF scattering in the VF and HF configurations at $\boldsymbol{Q}$ = (1.45,1.45,0.6) for T = 10 K and 61 K.

References

1) A. Oosawa, et al., JAEA-Review, 4, 61(2007).
2) A. Oosawa, et al., J. Phys. Soc. Jpn., 75, 074719(2006).
3) H. Yoshizawa, et al., Phys. Rev. B, 23, 2298(1981).
4) R. M. Moon, et al., Phys. Rev., 181, 920(1969).

2.4.3
Softening of Magnetic Excitations Leading to Pressure-Induced Quantum Phase Transition in Gapped Spin System $KCuCl_3$

K. Goto[1,4], T. Osakabe[1], K. Kakurai[1], Y. Uwatoko[2], A. Oosawa[3] and H. Tanaka[4]

[1] *Quantum Beam Science Directorate, Japan Atomic Energy Agency, Tokai, Ibaraki 319-1195*
[2] *Institute for Solid State Physics, The University of Tokyo, Kashiwanoha, Kashiwa, Chiba 277-8581*
[3] *Department of Physics, Sophia University, Kioi-cho, Chiyoda-ku, Tokyo 102-8554*
[4] *Department of Physics, Tokyo Institute of Technology, Oh-okayama, Meguro-ku, Tokyo 152-8551*

$KCuCl_3$ is an interacting spin dimer system, which has a singlet ground state with an excitation gap of $\Delta = 2.67$ meV[1]. $KCuCl_3$ undergoes a pressure-induced quantum phase transition (QPT) to an antiferromagnetic (AF) state. The critical pressure obtained through magnetization measurements is $P_c = 8.2$ kbar[2]. To investigate the pressure dependence of individual exchange interactions and the change of dispersion relations under pressure, we have performed neutron inelastic scattering experiments on $KCuCl_3$ under high hydrostatic pressure.

The experiments were performed using TAS-1 and LTAS spectrometers installed at JRR-3 in JAEA, Tokai. In general, it is difficult to carry out neutron inelastic scattering under high pressure because of the small sample space and the attenuation of the neutron beam due to the thick pressure cell. In the present study, we used a newly designed cylindrical high-pressure clamp cell made of mesoalite. The inner diameter of the sample capsule was 8.0 mm and the working height is 22 mm. A $KCuCl_3$ single crystal was shaped into a column of 7.8 mm in diameter and 14 mm in length with the central axis parallel to the crystallographic b-axis. A mixture of Fluorinert FC70 and FC77 was used as the pressure-transmitting medium. A hydrostatic pressure of $P = 4.7$ kbar was applied at helium temperatures. The pressure was determined from the lattice constants of a NaCl crystal placed in the sample space. A well-defined single excitation mode was observed.

The dispersion relations in the $a^* - c^*$ plane were obtained, as shown in Fig. 1. Softening of the triplet mode due to the applied pressure is clearly observed at all $\boldsymbol{Q}$ values. The excitation gap for $P = 4.7$ kbar corresponding to the lowest excitation energy was evaluated as $\Delta = 1.52$ meV. Using the random phase approximation, we have analyzed the dispersion relations and obtained the intradimer and effective interdimer interactions. It was found that the intradimer interaction decreases under hydrostatic pressure and the effective interactions between the nearest dimers along the a-direction and in the $(1, 0, \bar{2})$ plane increase. These pressure dependences of the exchange interactions give rise to the observed pressure-induced QPT from a gapped ground state to an AF state in $KCuCl_3$. The present result has been published elsewhere[3].

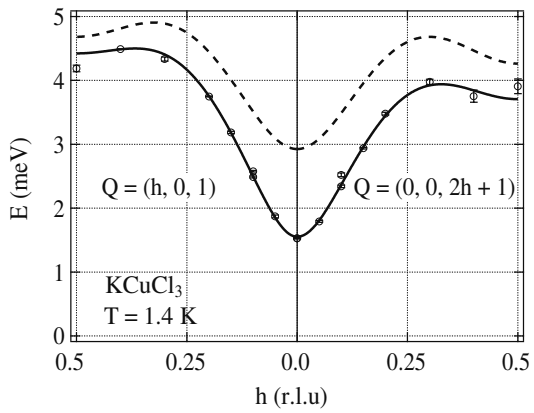

Figure 1: Dispersion relations $\omega(\boldsymbol{Q})$ in $KCuCl_3$ measured at $P = 4.7$ kbar for $\boldsymbol{Q}$ along $(h, 0, 1)$ and $(0, 0, 2h + 1)$. Dashed line is the dispersion curve at ambient pressure.

References

1) T. Kato, et al., J. Phys. Soc. Jpn., 67, 752(1998).
2) K. Goto, et al., J. Phys. Soc. Jpn., 75, 064703(2006).
3) K. Goto, et al., J. Phys. Soc. Jpn., 76, 053704(2007).

2.4.4
Neutron Elastic Scattering in Quantum Spin System NH_4CuCl_3

T. Ono[1], K. Goto[1,4], Y. Kubota[1], H. Tanaka[1], N. Metoki[2], F. Honda[2] and K. Kakurai[2]

[1] *Department of Physics, Tokyo Institute of Technology, Oh-okayama, Meguro-ku, Tokyo 152-8551*
[2] *Quantum Beam Science Directorate, Japan Atomic Energy Agency, Tokai, Ibaraki 319-1195*

NH_4CuCl_3 is a weakly coupled spin dimer system, which has the same crystal structure as $KCuCl_3$ at room temperature[1]. With decreasing temperature, NH_4CuCl_3 undergoes structural phase transitions at $T_{t1} = 156$ K and $T_{t2} = 70$ K[2]. The magnetic ground state of NH_4CuCl_3 is gapless in contrast to $KCuCl_3$[3]. NH_4CuCl_3 undergoes 3D magnetic ordering at $T_N = 1.3$ K[3]. Remarkable feature of NH_4CuCl_3 is that the magnetization curve has two plateaus at one-quarter and three-quarters of the saturation magnetization[4]. Although various models for the formation of the magnetization plateaus have been proposed[5], the mechanism leading to the magnetization plateaus has not been clarified. Recently, magnetic Bragg reflection was observed at $\boldsymbol{Q} = (0, 0, 1)$[2], and its intensity decreases with increasing external field. To investigate the magnetic structure in the ordered phase, we have performed a neutron elastic scattering experiment on NH_4CuCl_3 at zero magnetic field.

The experiment was performed using the TAS-2 spectrometer installed at JRR-3 in JAEA, Tokai. The incident neutron energy was fixed at $E_i = 14.7$ meV, and the horizontal collimation sequence was chosen as guide-80'-80'-open. A single crystal of ~ 0.25 cm^3 was used. The sample was mounted in the cryostat with its (010) plane parallel to the scattering plane, so that the reflections in the $a^* - c^*$ plane were investigated. The sample was cooled to 50 mK using a dilution refrigerator.

Magnetic Bragg peaks were observed below $T_N = 1.3$ K at $\boldsymbol{Q} = (h, 0, l)$ with the integer h and odd l. These reciprocal lattice points are equivalent to those for the magnetic-field and pressure induced ordered phases in $TlCuCl_3$[6,7]. No Bragg peak indicating superlattice structure along the a-axis was observed. Table 1 summarizes the integrated intensities of magnetic Bragg reflections normalized to the (001) reflection. It is noted that Bragg intensities for $\boldsymbol{Q} = (0, 0, 5)$, $(1, 0, 1)$ and $(1, 0, -1)$ are strong. These intensities for the magnetic-field and pressure induced ordered phases in $TlCuCl_3$ are less than 0.1. From the magnetization and excitation data[2,4], we can deduce that one-quarter of the spins are ordered below T_N and the rest of spins are in the singlet state at zero magnetic field. At present, the magnetic structure of NH_4CuCl_3 cannot be determined uniquely. Neutron elastic scattering experiments taking other scattering plane are needed.

Table 1: Integrated magnetic Bragg peak intensities observed at 50 mK. The intensities are normalized to the $(001)_M$ reflection.

$(001)_M$	$(003)_M$	$(005)_M$
1.000	0.000	0.425
$(101)_M$	$(10\bar{1})_M$	$(103)_M$
0.385	0.302	0.109
$(10\bar{3})_M$	$(201)_M$	$(20\bar{1})_M$
0.485	0.000	0.000

References

1) R. D. Willett, et al., J. Chem. Phys., 38, 2429(1963).
2) Ch. Rüegg, et al., Phys. Rev. Lett., 93, 037207(2004).
3) B. Kurniawan, et al., J. Phys.: Condens. Matter, 11, 9073(1999).
4) W. Shiramura, et al., J. Phys. Soc. Jpn., 67, 1548(1998).
5) M. Matsumoto, Phys. Rev. B, 68, 180403(R)(2003), and references therein.
6) H. Tanaka, et al., J. Phys. Soc. Jpn., 70, 939(2001).
7) A. Oosawa, et al., J. Phys. Soc. Jpn., 72, 1026(2003).

2.4.5

Magnetic Structure of $Co_2TeO_3Cl_2$

T. Kashi, Y. Yasui, T. Moyoshi, M. Sato, N. Igawa[1] and K. Kakurai[1]

Department of Physics, Nagoya University, Furo-cho, Chikusa-ku, Nagoya 464-8602
[1]*Quantum Beam Science Directorate, JAEA, Tokai, Ibaraki 319-1195*

$Co_2TeO_3Cl_2$ has so-called delta or sawtooth chains consisting of corner-sharing triangles of Co spins,[1)] and two crystallographically distinct Co^{2+} sites exist in this system. If the exchange interaction between the nearest neighbor Co spins is antiferromagnetic, a rather strong magnetic fluctuation is expected.

Measurements of the magnetic susceptibility χ and specific heat C of $Co_2TeO_3Cl_2$ have revealed that two transitions take place at temperatures $T = 73$ K (T_{N1}) and 15 K (T_{N2}). At T_{N1}, a small anomaly has been observed in the $\chi - T$ curve. A weak ferromagnetic moment shows up at T_{N2} with decreasing T. In the $C/T - T$ curve, anomalies characteristic of second-order phase transitions are observed at both transition temperatures.

For this system, we have carried out the powder neutron diffraction measurements down to 2.8 K at the high resolution powder diffractometer (HRPD) of JRR-3 of JAEA in Tokai, and carried out Rietveld analyses using RIETAN-2000 at two temperatures $T_{N2} < T < T_{N2}$ and $T < T_{N2}$.

Neutron powder patterns were taken at 85 K ($> T_{N1}$), 25 K (between T_{N2} and T_{N1}) and 2.8 K ($< T_{N2}$). At 25 K, superlattice reflections ($h/2\ k/2\ l/2$) (h, k, l = odd) were found and at 2.5 K, superlattice reflections ($h\ k\ l/2$) (h, k, l = odd) were also found. The integrated intensities and 2θ positions of the peaks appearing at 25 K have been found not to change with T from 25 to 2.8 K. By using the obtained intensities of the magnetic reflections, we have determined the magnetic structures of the ordered phases. At 25 K, only the Co(2) moments order antiferromagnetically with their spins along the b-axis, where the ordered moment is 3.6 ($\pm$0.2) μ_B.

At 2.8 K, the Co(1) moments not only order nearly parallel to the a-axis but alse cant towards the b-axis by 13.3° due to Dzyaloshinski-Moriya interaction, which causes the weak ferromagnetism observed below T_{N2}. The ordered moment is 3.3 ($\pm$0.2) μ_B. The magnetic structure of Co(2) spins and their ordered moment are unchanged when T is changed through T_{N2}. For the non-collinear magnetic structure and the nearly individual orderings of the sublattices of the Co(1) and Co(2) sites, the structural characteristics of the present system with isosceles triangles seems to be important.

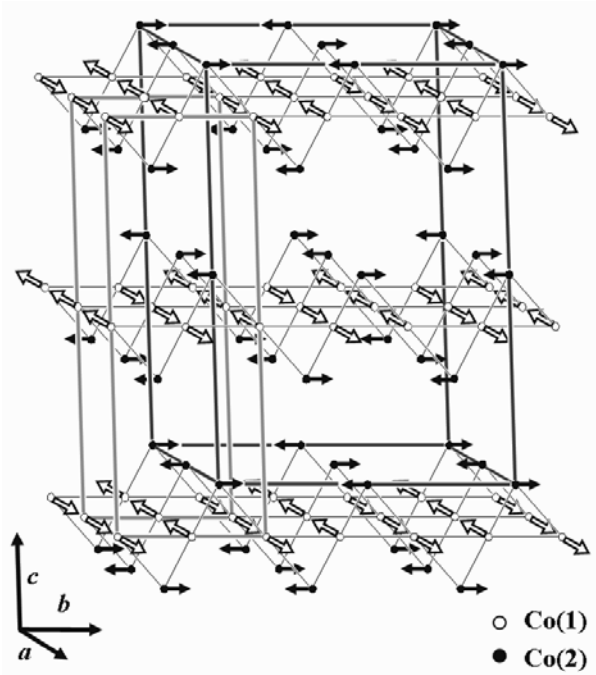

Figure 1: Magnetic structure of $Co_2TeO_3Cl_2$ at 2.8 K. The open and closed circles indicate the Co(1) and Co(2) sites, respectively. The arrows indicate the directions of magnetic moments. The Co(1) spins cant from the a-axis toward the b-axis by ~13.3°.

References

1) R. Becker, et al., J. Solid. State. Chem., 179, 836(2006).

2.4.6
Spherical Polarization Analysis of Artificially Confined Spin-Density Waves in Cr/Sn Multilayers

M. Takeda, M. Nakamura, K. Kakurai, K. Mibu[1] and E. Lelièvre-Berna[2]

Quantum Beam Science Directorate, JAEA, Tokai, Ibaraki 319-1195
[1]*Graduate School of Engineering, Nagoya Institute of Technology, Gokiso-cho, Showa-ku, Nagoya, Aichi 466-8555*
[2]*Institut Laue-Langevin, 6 rue Jules Horowitz BP 156 - 38042 Grenoble Cedex 9, France*

In Cr/Sn(001) multilayers in which monatomic Sn nonmagnetic layers are periodically embedded, spin-density waves (SDWs) are formed below the Néel temperature like that in bulk Cr. They are, however, quite different to the SDW in bulk Cr. For instance the wavelength of the SDW is defined not simply by the nesting vector of Cr but also by the artificial periodicity introduced by the Sn layers[1,2]. We performed the spherical neutron-polarization analysis of these anomalous SDW structures by using CRYOPAD(CRYOgenic Polarization Analysis Device)[3,4] on TAS-1 to get detailed magnetic structural information which could not be obtained with unpolarized neutron experiments[5].

The samples were [Cr(10.0 nm)/Sn(0.2 nm)] × 24 grown on MgO(001) substrates. The incident neutrons were polarized and monochromatized with a Cu_2MnAl polarizing monochromator. The energy of the neutrons was fixed at 14.7 meV. The scans were done through the (001) and (010) reciprocal points, where the nuclear peaks were forbidden, along the [001] (out-of-plane) and [010] (in-plane) directions.

The film had a commensurate antiferromagnetic (CAF) structure at 290 K and changed into the incommensurate SDW (ISDW) state with decreasing temperature. Several satellite peaks corresponding to the ISDW structures appeared in the scan profiles. The position of each peak can be written as (01 $\pm N\Delta$) or (00 1 $\pm N\Delta$) where $\Delta = a_{001}/\Lambda$, and Λ is the distance of artificial boundary ($t_{\mathrm{Cr}} + t_{\mathrm{Sn}} = 10.2$ nm).

The polarization matrix, P_{ij}, was measured at 270 K and 4.3 K[6]. The matrix elements are given in Ref. 5. At (010) peak the out-of-plane and in-plane component of magnetic interaction vectors, $\boldsymbol{M}(\boldsymbol{Q})$, are detected while at (001) only two in-plane components reflect in P_{ij}. The observed P_{yy} is equal to -P_{zz} for (001) at 270 K. On the other hand, $|P_{yy}|$ is larger than $|P_{zz}|$ for (010). This indicates that the sample has a multi-domain CAF structure with $\boldsymbol{M}(\boldsymbol{Q})$ mostly normal to the plane and that the distribution of the domain is isotropic in the (001) plane at 270 K.

In the ISDW phase at 4.3 K, $\boldsymbol{M}(\boldsymbol{Q})$ seems to incline towards the in-plane because $|P_{zz}| > |P_{yy}|$ for the first satellite peak of (01 Δ). Significant depolarization is observed in P_{xx} for (00 1+Δ). This would imply that this peak has both nuclear and magnetic origins. Further investigation is, however, necessary to derive a firm conclusion.

The neutron polarimetry experiments gave us much more detailed magnetic structural information on the ISDW, which could not have been obtained by the conventional unpolarized and polarized neutron diffraction measurements. Measurements of P_{ij} for the other reflections and temperature dependence of P_{ij} are expected to give a better insight into the magnetic nature of this multilayer.

References

1) K. Mibu, M. Takeda, J. Suzuki, A. Nakanishi, T. Kobayashi , Y. Endoh and T. Shinjo, Phys. Rev. Lett., 89, 287202(2002).
2) M. Takeda, K. Mibu, T. Shinjo, Y. Endoh and J. Suzuki, Phys. Rev. B, 70, 104408(2004).
3) F. Tasset, Physica B, 156-157, 627(1989).
4) M. Takeda, M. Nakamura, K. Kakurai, E. Lelièvre-Berna, F. Tasset and L. -P. Regnault, Physica B, 356, 136(2005).
5) P. J. Brown, Physica B, 297, 198(2001).
6) M. Takeda, M. Nakamura, K. Kakurai, K. Mibu and E. Lelièvre-Berna, Physica B, 397, 56(2007).

2.4.7
Magnetic Microstructure of $LaMnO_{3+\delta}$ Nanocrystals in Mesoporous Silica

H. Kira, H. Tamura, Y. Murakami, T. Shinohara[1] and J. Suzuki[1]

Department of Physics, Graduate School of Science, Tohoku University, Sendai, 980-8578
[1]*Japan Atomic Energy Agency, Tokai, Ibaraki 319-1195*

We have synthesized a perovskite-type manganite $LaMnO_{3+\delta}$ (LMO) with an average size of 20 nm to study the characteristic electronic states in nanocrystals[1,2]. The magnetization, susceptibility and neutron diffraction measurements have revealed that the ferromagnetism (FM) with T_C = 260 K coexists with the antiferromagnetism (AFM) with T_N = 90 K. It is reasonable for us to assume that LMO nanocrystals of large AFM core with a short correlation length of $\sim$ 5 nm were coated with a thin FM shell. We performed small-angle neutron scattering (SANS) measurements at SANS-J at JRR-3 so as to confirm the core-shell magnetic microstructure of the LMO nanocrystals.

We used an average wavelength (λ = 0.4 nm) with a relative wavelength spread $\Delta\lambda/\lambda$ $\sim$ 10% at sample to detector distances of 2.5 and 10 meter, respectively, to cover a magnitude of the wavevector transfer range 0.02 $nm^{-1} < q < 2$ nm^{-1}. The measured intensities were normalized by the intensities of a standard aluminum sample. The magnetic SANS intensity $I(q)$ was obtained by subtracting the nuclear scattering obtained at 300 K from the total SANS intensity obtained at 9 K with applied field of 1 T (Fig. 1).

We have found a definite ferromagnetic contribution in the magnetic SANS spectrum. A characteristic change in the slope of the scattering curve around q = 0.1 nm^{-1} is associated with the size of LMO nanocrystals, and the q^{-2} dependence in the q range $q <$ 0.1 nm^{-1} is attributed to the effect of interparticle scattering. In the high q region, $I(q)$ is generally expected to decrease according to a function of q^{-4}, which is well known as Porod's law, however, the magnetic SANS spectrum exhibits a $q^{-3.5}$ dependence in the q range 0.1 $nm^{-1} < q <$ 1 nm^{-1}. Thus it is considered that the observed magnetic SANS spectrum in this q range originates from the intra-particle contributions and the q dependence of the magnetic SANS spectrum changes into q^{-4} in $q >$ 1 nm^{-1}. Then the thickness of the FM shell is estimated to be less than 1 nm, which is consistent with our core-shell model. It is considered that the FM state occurs through the double exchange mechanism owing to the hole doping near the surface with the excessive oxygen. The hole-doped bulk LMO with a rhombohedral structure shows only ferromagnetism but no antiferromagnetism. Thus the rhombohedral AFM phase newly appeared is ascribed to the size effect.

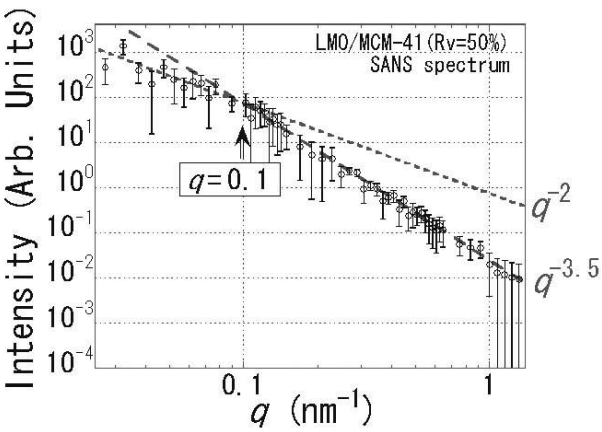

Figure 1: Ferromagnetic SANS spectrum of LMO nanocrystals in mesoporous silica.

References

1) H. Kira, et al., AIP Conference Procedings, 850, 1157(2006).
2) H. Kira, et al., J. Magnetism Magnet. Mater., 310, 2480(2007).

2.4.8
Neutron Scattering Study of Metamagnetic Phase Transition in $HoRhIn_5$ Compounds

N.V. Hieu[1], S. Jonen[2], T. Takeuchi[3], K. Sugiyama[1], R. Settai[1], Y. Ōnuki[1,2], T.D. Matsuda[2], Y. Haga[2] and N. Metoki[2]

[1] *Graduate School, Osaka University, Toyonaka, Osaka 560-0043*
[2] *Advanced Science Research Center, JAEA, Tokai, Ibaraki 319-1195*
[3] *Low Temperature Center, Osaka University, Toyonaka, Osaka 560-0043*

The metamagnetic transition of a single crystal of $HoRhIn_5$ was studied by neutron diffraction. This compound exhibits an antiferromagnetic structure with $\vec{q} = (1/2,0,1/2)$ below $T_N = 15.8$ K. The magnetization curve for $\vec{H}||[001]$ exhibits a characteristic two-step metamagnetic transition at $H_{m1} = 3.4$ T and $H_{m2} = 5.4$ T at $T = 2$ K[1]. Neutron diffraction experiments have been carried out using the TAS-2 and MUSASI spectrometers installed at the research reactor JRR-3 in JAEA. Experiments under high magnetic fields were carried out at $(hk0)$ and $(h0l)$ scattering plane with $\vec{H}||[001]$ by using a vertical or horizontal superconducting magnet.

Figure 1 shows the field dependence of the (3/2 0 5/2) antiferromagnetic peak intensity of $HoRhIn_5$. The AF1 represents the antiferromagnetic phase for $H < H_{m1}$, and AF2 for $H_{m1} < H < H_{m2}$ is the intermediate phase with the intensity roughly 25% of that for AF1. It means that the antiferromagnetic modulation in AF2 would be half that of AF1. On the other hand, the ferromagnetic moment in AF2 is a half of the saturation value, as a shown in Fig. 2. These results indicate flipping of the Ho moment. The temperature dependence of H_{m1} and H_{m2} obtained in the present work is in good agreement with the phase diagram extracted from the magnetization measurements. The magnetic structure at the intermediated phase AF2 could not been determined yet. Further experiments will be required to clarify the magnetic structure in magnetic fields.

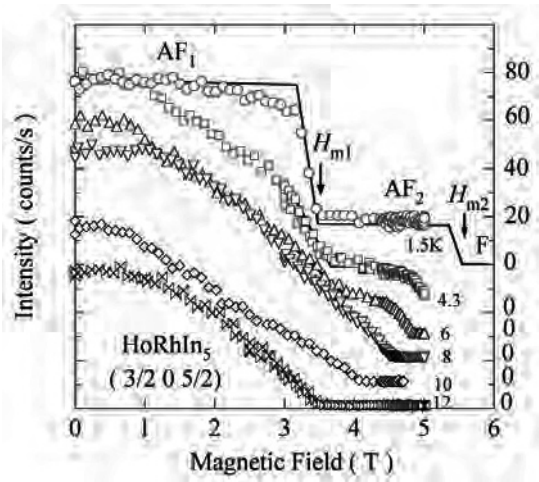

Figure 1: Field dependence of the intensity of (3/2 0 5/2) antiferromagnetic reflection for $HoRhIn_5$.

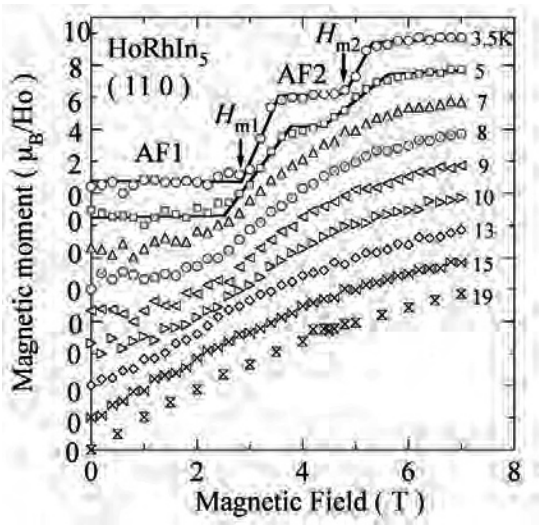

Figure 2: Magnetic field dependence of ferromagnetic moment measured at (110) reflection for $HoRhIn_5$.

References

1) N.V. Hieu, et al., J. Phys. Soc. Jpn., 75, 074708(2006).

2.4.9

Measurements of the Magnetic form Fators of α-Fe and CoFe Powder by Polarized Neutron Deffractometry

S. Oitani[1,2], Y. Ishii[1,3], M. Takeda[1], K. Kakurai[1],
Y. Sasaki[4], M. Kishimoto[4] and Y. Nishihara[3]

[1] *Quantum Beam Science Directorate, JAEA, Tokai, Ibaraki 319-1195*
[2] *Department of Physics, Ehime University, Matsuyama, Ehime 790-8577*
[3] *Department of Physics, Ibaraki University, Mito, Ibaraki 560-1234*
[4] *Development and Technology Division, Hitachi Maxell,Ltd, Ooyamazaki ,Kyoto 618-8525*

Ferromagnetic nanoparticles are attracting attention from the viewpoint of applications to magnetic recording materials. Polarized neutron diffraction measurements at ambient temperature using 80 meV neutrons were performed to estimate the value of magnetization of the nanoparticles.

The triple-axis neutron spectrometer, TAS-1, installed at JRR-3 was used to obtain the magnetic form factor. A magnetic field of 10 kOe was applied perpendicular to the scattering vector to saturate the magnetization.

In the polarized neutron diffraction measurements, Bragg peak intensities from the samples with net magnetizations depend on the neutron spin direction with respect to the magnetization direction.

The intensities are written as follows.

$$\begin{aligned} I_+ &= (\frac{d\sigma}{d\Omega})_+ \\ &= \{F_{\mathrm{N}}(Q) + \bar{F}_{\mathrm{M}}(Q)\}^2 \exp(-2W) \end{aligned} \tag{1}$$

$$\begin{aligned} I_- &= (\frac{d\sigma}{d\Omega})_- \\ &= \{F_{\mathrm{N}}(Q) - \bar{F}_{\mathrm{M}}(Q)\}^2 \exp(-2W) \end{aligned} \tag{2}$$

where $F_{\mathrm{N}}(Q)$ and $F_{\mathrm{M}}(Q)$ are nuclear and magnetic structure factors, respectively, and $\exp(-2W)$ is the Debye-Waller factor. When $F_{\mathrm{N}}(Q)$ is known, $F_{\mathrm{M}}(Q)$ can be determined from the flipping ratio (FR) as follows.

$$\begin{aligned} FR &= \frac{(\frac{d\sigma}{d\Omega})_+}{(\frac{d\sigma}{d\Omega})_-} = \left(\frac{F_{\mathrm{N}}(Q) + \bar{F}_{\mathrm{M}}(Q)}{F_{\mathrm{N}}(Q) - \bar{F}_{\mathrm{M}}(Q)}\right)^2 \\ &= \left(\frac{1+\gamma(Q)}{1-\gamma(Q)}\right)^2 \end{aligned} \tag{3}$$

$$\gamma = \frac{F_{\mathrm{M}}(Q)}{F_{\mathrm{N}}(Q)} \tag{4}$$

The magnetic moment was determined by fitting using the well-known magnetic form factor of α-Fe taking the depolarization effect into consideration. The scaled magnetic form factor using the magnitude of magnetic moments determined by the fitting procedure is shown in Fig. 1.

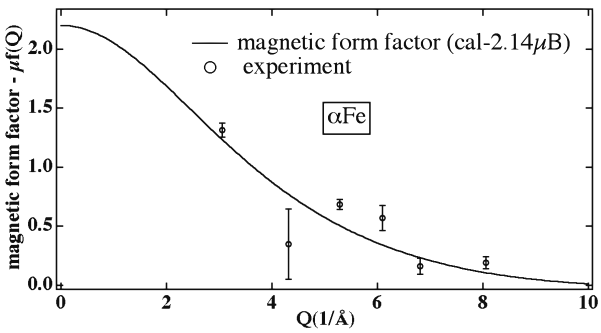

Figure 1: Scaled magnetic form factor of α-Fe

The measured magnetic moment per atom of each sample is shown in Table 1. These results show that the polarized neutron powder diffraction method is a powerful and accurate tool to microscopically determine the magnetization of ferromagnetic nanoparticles.

sample	reference	result
α-Fe (19 nm)	2.2 μ_B	2.14 ± 0.32 μ_B
CoFe (35 nm)	2.47 μ_B	2.42 ± 0.17 μ_B
CoFe (45 nm)	2.47 μ_B	2.44 ± 0.33 μ_B

Table 1: Measured magnetic moments

2.4.10
Magnetic-field Induced Magnetic Phase Transitions in Multiferroic Compound of $ErMn_2O_5$

H. Kimura, S. Wakimoto[1], Y. Noda, K. Kaneko[1], N. Metoki[1], K. Kakurai[1] and K. Kohn[2]

Institute of Multidisciplinary Research for Advanced Materials, Tohoku University, Sendai 980-8577
[1]*JAEA, Tokai, Ibaraki 319-1195*
[2]*Department of Physics, Waseda University, Tokyo 169-8555*

The recent discovery of a colossal magnetoelectric (CME) effect in manganese oxides of RMnO$_3$ and RMn$_2$O$_5$ (R = rare earth elements)[1,2] opens possibilities of new candidates for multifunctional devices such as a magnetically controlled ferroelectric memory. These systems show a multiferroic behavior where an antiferromagnetic order and a ferroelectric order coexist, which is thought to be ingredient essential for realizing the CME effect. However, microscopic mechanisms of the CME effect is not fully understood yet. We have conducted neutron diffraction measurements under high magnetic fields in the multiferroic $ErMn_2O_5$ and found unambiguous relation between the microscopic magnetism and the field-induced ferroelectricity.

Neutron diffraction measurements were performed using the thermal neutron triple-axis spectrometer TAS-2. A single crystal of $ErMn_2O_5$ was mounted on the (h 0 l) scattering plane with a horizontal-field superconducting magnet, which results in applying a field up to 5 T along the a- and c-axis. The incident and final energies of neutrons were fixed at 14.3 meV.

Figure 1 summarizes the magnetic field (H) – temperature (T) phase diagrams for magnetic phases, showing that there exists no field dependence when the magnetic field was applied along the a-axis while incommensurate – commensurate – incommensurate magnetic phase transitions are induced by applying the field along the c-axis. In this figure, the H – T phase diagram for dielectric property reported in Ref. 3 is superposed, showing that the well-defined ferroelectric state is induced only in the CM phase. This one-to-one correspondence between the magnetic phase diagram and the dielectric phase diagram under a magnetic field clearly indicates that the electric polarization is magnetically induced and the commensurate magnetic structure is indispensable to the ferroelectricity in the multiferroic RMn$_2$O$_5$ system.

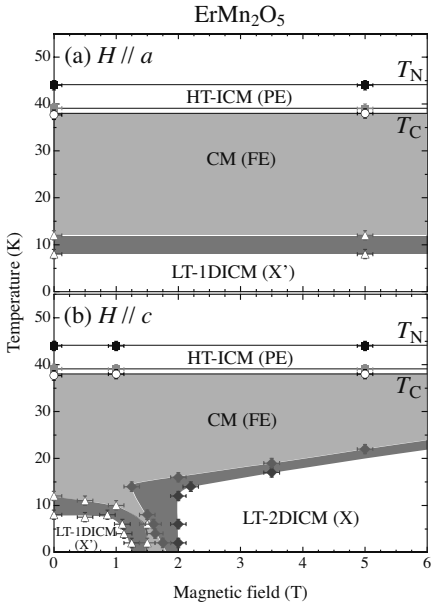

Figure 1: $H-T$ magnetic phase diagram in $ErMn_2O_5$, where magnetic field was applied along (a) a-axis and (b) c-axis. The dielectric phase diagram taken by Higashiyama et al.[3] is superposed in this figure. Abbreviations: HT-ICM; High-temperature incommensurate magnetic, CM; Commensurate magnetic, LT-1DICM; Low-temperature one dimensionally modulated incommensurate magnetic, LT-2DICM; Low-temperature two dimensionally modulated incommensurate magnetic, PE; Paraelectric, FE; Ferroelectric, X and X'; unidentified.

References

1) T. Kimura, et al., Nature (London), 426, 55 (2003).
2) N. Hur, et al., Nature (London), 429, 392 (2004).
3) D. Higashiyama, et al., Phys. Rev. B, 72, 064421 (2005).

2.4.11
Temperature and Electric Field Dependences of Spin Chirality in Multiferroic Compound of $HoMn_2O_5$

H. Kimura, S. Wakimoto[1], K. Nishihata, Y. Noda, M. Takeda[1], K. Kakurai[1] and K. Kohn[2]

Institute of Multidisciplinary Research for Advanced Materials, Tohoku University, Sendai 980-8577
[1]*JAEA, Tokai, Ibaraki 319-1195*
[2]*Department of Physics, Waseda University, Tokyo 169-8555*

It is well known that the multiferroic compounds of $HoMn_2O_5$ show a colossal magnetoelectric (ME) effect. This material has successive magnetic transition below 45 K from a high-temperature incommensurate magnetic (HT-ICM) phase to a commensurate magnetic (CM) phase, and finally to a low-temperature incommensurate magnetic (LT-ICM) phase as the temperature decreases. A recent neutron diffraction study[1)] as well as dielectric measurements[2)] under a magnetic field have established that a well-defined ferroelectricity is induced only in the CM phase. Our magnetic structure analysis also revealed that there exists spiral spin structure in the CM phase[3)], which can produce a spontaneous electric polarization by an inverse effect of Dzyaloshinski–Moriya interaction with $\mathbf{S}_i \times \mathbf{S}_j$ products. Thus, we have thus performed polarized neutron diffraction measurements under an electric field to clarify the relation between the rotation direction of the spiral component (spin chrality) and the direction of spontaneous electric polarization, which can confirm whether the transverse spiral structure yields an electric polarization.

Polarized neutron diffraction measurements were performed using the triple-axis spectrometer TAS-1 installed at JRR-3. An incident beam was unpolarized by a PG(002) monochromator while a scattered beam was polarized by a Heusler(111) monochromator. A single crystal of $HoMn_2O_5$ was mounted on the $(h\ 0\ l)$ scattering plane. The incident and final energies of neutrons were fixed at 14.7 meV.

Figure 1 shows the temperature dependences of magnetic Bragg reflections with a chiral component (filled symbols) and without a chiral component (open symbols) under an electric-field cooling with + 5 kV/mm. This result shows that there is no chiral component in the HT-ICM phase (paraelectric phase) while the chiral component arises in the CM phase (ferroelectric phase). Furthermore, in the CM phase, there is one-to-one correspondence between the electric field dependence of the amplitude of the chiral component and that of the amplitude of electric polarization, suggesting that the spin chirality yields the electric polarization. However, the relevance between the chirality component and the dielectric property in the LT-ICM phase is not clarified yet.

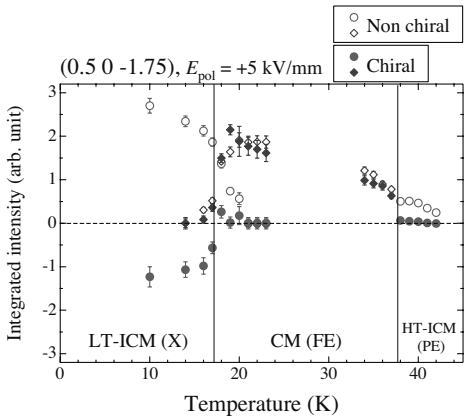

Figure 1: Temperature dependences of magnetic Bragg reflection with chiral component (filled symbols) and without chiral component (open symbols). Electric-field-cooling was performed below 50 K with + 5 kV/mm. The dielectric phase is paraelectric (PE), ferroelectric (FE), and unidentified (X) phases in HT-ICM, CM, and LT-ICM phases, respectively.

References

1) H. Kimura, et al., J. Phys. Soc. Jpn., 75, 113701(2006).
2) D. Higashiyama, et al., Phys. Rev. B, 72, 064421(2005).
3) H. Kimura, et al., J. Phys. Soc. Jpn., 76, 074706(2007).

2.4.12
Small Angle Neutron Scattering Study of Interface Nanostructure in Sintered Nd-Fe-B Magnets Processed Under High Magnetic Fields †

T. Akiya[1], H. Kato[1,2], M. Takeda[3], J. Suzuki[3], D. Yamaguchi[4], S. Koizumi[4], M. Sagawa[5] and K. Koyama[6]

[1] *Department of Applied Physics, Tohoku University, Sendai, Miyagi 980-8579*
[2] *Faculty of Engineering, Yamagata University, Yonezawa, Yamagata 992-8510*
[3] *Quantum Beam Science Directorate, JAEA, Tokai, Ibaraki 319-1195*
[4] *Advances Science Research Center, JAEA, Tokai, Ibaraki 319-1195*
[5] *Intermetallics Co., Ltd, Nishi-Kyoku, Kyoto 615-8206*
[6] *Institute for Materials Research, Tohoku University, Sendai, Miyagi 980-8577*

Sintered Nd-Fe-B magnets are the most promising materials for a driving motor of the hybrid electric vehicle (HV). In this application, a large value of coercivity H_c is required, because the operating temperature of magnets reaches beyond 450 K. As a symptomatic treatment, Nd has been replaced partly by Dy to enhance H_c. But the problem is an estimated short supply of Dy in the HV mass-production stage due to its low natural abundance. We have recently shown[1)] that H_c of Nd-Fe-B magnets can be enhanced by applying a high magnetic field during the annealing. In order to investigate the reason for the H_c increase, we started a small angle neutron scattering (SANS) study. The SANS technique has an advantage over microscopic methods. That is, we can non-destructively obtain quantitative information averaged over a bulk sample. In the present study, two kinds of Nd-Fe-B samples with and without Cu and Al additives were prepared. These samples were cut into plate-forms with the dimensions $18\times15\times1.5$ mm^3, in which the direction of the magnetization vector, corresponding to the c-axis of the tetragonal $Nd_2Fe_{14}B$ lattice, was parallel to the 15 mm side. A 99% enriched ^{11}B isotope was used to avoid the high neutron absorption of ^{10}B in natural boron. SANS experiments were performed with SANS-J and PNO apparatus equipped at JAEA in which the incident wavelength of neutrons were 0.65 and 0.2 nm, respectively.

In samples without Al and Cu additives, an intensity of scattered neutrons was proportional to the q^{-4} where q is the scattering vector. Whereas in the samples with Al and Cu additives, we observed a marked deviation from the simple relation above for $q > 0.3$ nm^{-1}, only when the scattering vector is parallel to the c-axis of the tetragonal $Nd_2Fe_{14}B$ cell. We have reproduced these experiments by calculations, assuming a structure in which a core of $Nd_2Fe_{14}B$ phase is surrounded by a Cu-rich shell with a thickness of $4 \sim 8$ nm. We already reported[1)] that the DSC measurements suggest an existence of Nd-Cu and Al-Cu eutectic phases at the grain boundary. Thus, the DSC and SANS results thus suggest that an existence of the Cu-containing liquid phase is strongly correlated with the H_c enhancement by the high field annealing.

References

1) H. Kato, T. Akiya, M. Sagawa, K. Koyama and T. Miyazaki, J. Magn. Magn. Mater., 310, 2596(2007).

† Common use program of JAEA

2.4.13
Magnetic Structure and Phase Diagram of $NpIn_3$ Studied by Neutron Scattering under Magnetic Field

F. Mizuno[1,2], T. Sugai[1,2], N. Metoki[1,2], Y. Haga[1,2], D. Aoki[3], Y. Homma[3] and Y. Siokawa[3]

[1] *Actinide compound magnetism and superconductivity research group, JAEA,Tokai,Ibaraki 319-1195*
[2] *Department of Physics, Tohoku University, Sendai, Miyagi 980-8578*
[3] *International Research Center for Nuclear Material Science, Tohoku University, Oarai, Ibaraki 311-1313*

$NpIn_3$ is a cubic compound with $AuCu_3$-type structure. The ferromagnetic order was reported in a narrow temperature region for 10 K < T_C < 14 K, while an antiferromagnetic ground state is stable below T_N = 10 K. A previous neutron diffraction study[1)] reported a longitudinal modulated magnetic order with q=(3/8 3/8 3/8) in the ground state. Two metamagnetic transitions have been reported for three principal directions, $H \parallel$ <100>, <110> and <111> from the antiferromagnetic (AF) ground state to the AF+FM phase, which is followed by the FM phase at high fields. Here the order parameter of the intermediate AF+FM phase is unknown yet.

In order to clarify the order parameter and magnetic structure, we studied $NpIn_3$ by neutron scattering under a magnetic field with a triple-axis spectrometer TAS-2 in JRR-3.

The intensity of the (0 0 1) reflection increases below 14 K then decreases rapidly at 10 K down to the background. We observes magnetic reflections, for example (3/8 3/8 5/8) (Fig.1). These results are consistent with a previous study[1)]. The intensity of the (3/8 3/8 5/8) reflection decreases rapidly under the magnetic fields above 3 T. We found the reflections (0 1/2 1/2) and (1 1/2 1/2) in the AF+FM phase. A field dependence of the (1 1/2 1/2) peak intensity for various temperature is observed(Fig.2). These data indicate that the (1 1/2 1/2) peak appears in the AF+FM phase. The critical field between the AF and the AF+FM phases is in good agreement with a magnet susceptibility[2)].

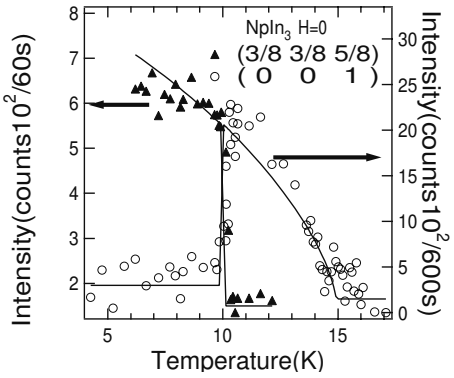

Figure 1: Temperature dependence of the (3/8 3/8 5/8) and (0 0 1) reflections intensity.

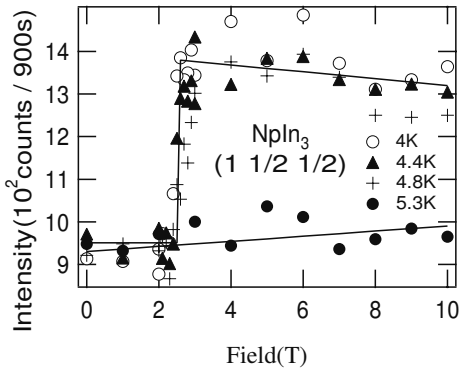

Figure 2: Field dependence of the (1 1/2 1/2) reflection intensity for various temperature.

References

1) E. Colineau, et al., Physica B, 206-207, 528(1995).
2) D. Aoki, et al., J. Phys. Soc. Jpn., 75, 084710(2006).

2.4.14
Magnetic Ordering Process in the Layered Triangular Lattice System $LuFe_2O_4$ in Applied Field

K. Kakurai, M. Matsuda, K. Yoshii[1], N. Ikeda[2], Y. Ishii, H. Kito[3] and Y. Yamada[4]

Neutron Materials Research Center, QuBS, JAEA, Tokai, Ibaraki 319-1195
[1]*Synchrotron Radiation Research Center, QuBS, JAEA, Hyogo 679-5148*
[2]*Department of Physics, Okayama Univ., Okayama 700-8530*
[3]*National Insitute of Advanced Industrial Science and Technology, Tsukuba 305-8561*
[4]*ARCSE, Waseda University, Tokyo 169-0072*

In $LuFe_2O_4$, the Fe ions are arranged to form the hexagonal double layers and stack in the sequence of (AB), (CA), (BC),... along the rhombohedral unique axis. The average valence of the Fe ions is expected to be $Fe^{+2.5}$ in these materials. More recently the evidence for ferroelectricity arising from electron correlations is found by means of resonant X-ray scattering experiment directly determining the ordering of the Fe^{+2} and Fe^{+3} ions[1)]. Furthermore, the temperature dependence of the electric polarization indicates an intimate relation between the coherence length of the charge-ordered region and the magnetic correlations. We have been studying the magnetic ordering process in zero applied field of $LuFe_2O_4$, which clearly shows charge ordering at RT. A clear sign of 3-D ferrimagnetic ordering at T_N = 242 K has been observed. But at around T_f = 177 K there is yet another characteristic temperature, where the intensity distribution among the magnetic Bragg peaks changes and the correlation along c^* direction decreases drastically[2)]. Thus the ground state in zero applied field seems to be a some type of spin frozen state. To shed some light on this anomalous spin freezing process we performed both magnetization measurements and neutron scattering experiments under an applied magnetic field along the c-axis. Figure 1 (a) depicts the temperature dependence of the Q = (1/3,1/3,0) magnetic peak in H = 1 T and 3 T applied field vertical to the scattering plane. Under the applied field of 1 T, T_N is slightly increased and T_f is decreased to about 150 K. Under the applied field of 3 T, T_N increases even more (almost to 260 K) and T_f is now completely suppressed. Figure 1 (b) shows the magnetization measurements in the corresponding magnetic field, and the ferromagnetic component shows exactly the same behaviour as the antiferromagnetic component observed by neutron scattering. These results indicate that the spin frozen ground state in zero field is suppressed by the applied field along the c-axis. A neutron scattering experiment using a horizontal field magnet will clarify the low temperature behaviour of the correlation in c^* direction in applied fields, and is planned for near future.

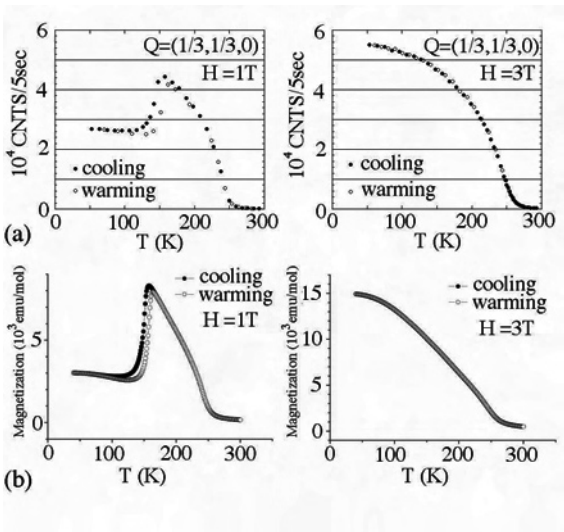

Figure 1: (a) Temperature dependence of Q = (1/3,1/3,0) magnetic peak intensity in H = 1 and 3 T applied field. (b) Temperature dependence of magnetization in H = 1 and 3 T applied field.

References

1) N. Ikeda, et al., Nature, 436, 1136(2005).
2) S. Nagai, et al., JAEA-Review, 2005-089, 82(2005).

2.5 Structural Physics

Ionic Conductivity, Phase Transition and Dynamics

This is a blank page

2.5.1
Crystal Structure Analysis of $LiGa_5O_8$ by Neutron Powder Diffraction

H. Yamauchi, T. Suzuki[1] and Y. Ohishi[1]

Quantum Beam Science Directorate, JAEA, Tokai, Ibaraki 319-1195

[1] *Optical Functional Materials Laboratory, Toyota Technological Institute, Nagoya, Aichi 468-8511*

Recently, many researchers have developed a type of glass-ceramic composites in which nanosize crystalline phase including Ni ions were frozen in the glass matrices. Transition metal-doped glasses are generally not applicable to gain media for laser and optical amplifiers, since nonradiative decay processes dominate the relaxation of the excited state in transition metals and the quantum efficiency is very low in glasses. However, transition metals can have sufficiently large quantum efficiency in single crystals, though it is very difficult to fabricate single crystal fibers. Glass-ceramics have the advantage of both crystalline and glass materials.

Nickel stably takes the divalent state in almost all the hosts and shows the broadband near-infrared emission from Ni^{2+} ions. It is expected that the Ni^{2+} ions occupy the octahedral site of spinel oxides in crystalline phases from the absorption and emission spectrum. Transparent Li_2O-Ga_2O_3-SiO_2 glass-ceramics embedding Ni-doped nanocrystals are very attractive as a host matrix for Ni-doping [1]. If Ni^{2+} ions are incorporated into the $LiGa_5O_8$ nanocrystals in glasses, high potential glass-ceramics can be synthesized. In this study we performed neutron powder diffraction experiments in order to clarify the crystal structure of $LiGa_5O_8$.

The neutron diffraction experiments were carried out on the high resolution powder diffractometer HRPD ($\lambda = 0.18229$ nm), using a powder sample synthesized by the conventional solid state reaction. The horizontal collimation was $12'$ - (monochromator) - $40'$ - (sample) - $6'$ - (detector). The crystal structure was determined by the Rietveld analysis using the program RIETAN-2000 [2].

Figure 1 shows the observed diffraction pattern (plus marks) and calculated intensity after Rietveld refinement (solid line) of $LiGa_5O_8$. The diffraction pattern was satisfactorily explained by the cubic type structure with a space group $P4_332$. This symmetry type structure has an octahedral $12d$ site like the octahedral $16d$ site in spinel oxides. Based on this result, next diffraction experiments for Ni: $LiGa_5O_8$ are under contemplation.

References

1) T. Suzuki, et al., Appl. Phys. Lett., 86, 131903(2005).
2) F. Izumi, et al., Mater. Sci. Forum, 321-324, 198(2000).

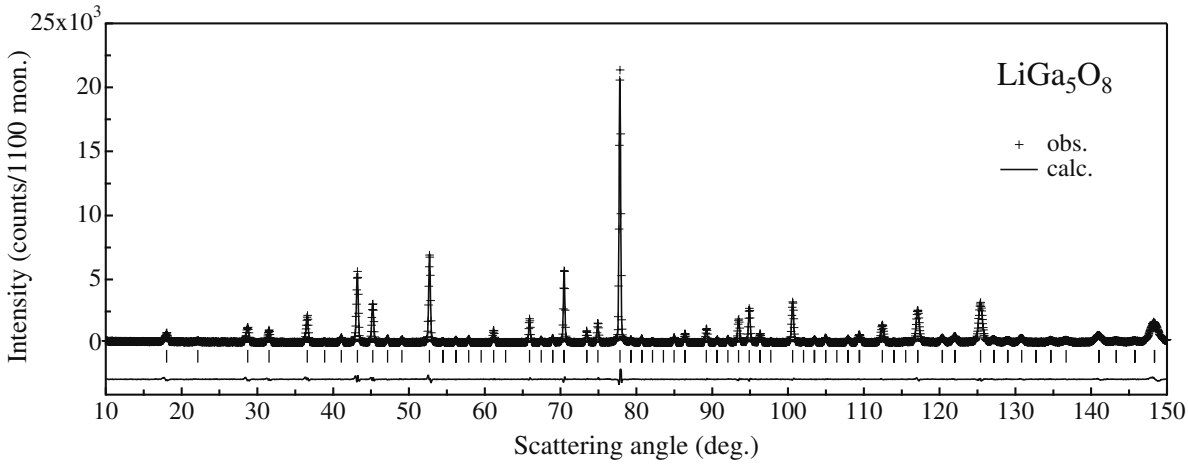

Figure 1: The high resolution neutron powder diffraction pattern of $LiGa_5O_8$ at room temperature.

2.5.2
Neutron Diffraction Study on Successive Structural Phase Transitions of $TlCoCl_3$

Y. Nishiwaki, A. Oosawa[1], K. Kakurai[2] and T. Kato[3]

Department of Physics, Tokyo Women's Medical University, Shinjuku-ku, Tokyo 162-8666
[1]*Department of Physics, Sophia University, Chiyoda-ku, Tokyo 102-8554*
[2]*Quantum Beam Science Directorate, Japan Atomic Energy Agency, Tokai, Ibaraki 319-1195*
[3]*Faculty of Education, Chiba University, Inage-ku, Chiba 273-8522*

Successive structural phase transitions of $TlCoCl_3$ are studied through single-crystal neutron diffraction measurements. The measurements were performed with the triple-axis spectrometer TAS-2. $TlCoCl_3$ is one of the $KNiCl_3$ family compounds.[1–3] The $KNiCl_3$ family compounds are distorted from the $CsNiCl_3$-type structure (space group $P6_3/mmc$) through successive structural phase transitions. Each structural phase is labeled as I, II, III, IV or V, from the high temperatures. The $CsNiCl_3$-structure has a -$NiCl_3$- chain along the c-axis, and the chains form a triangular lattice on the c-plane. The lattice deformation of the $KNiCl_3$ family compounds is characterized by upward or downward shifts of the chains along the c-axis. The crystal symmetries of phase II, III and V structures of $TlCoCl_3$ were reported to be $P6_3/mmc$, $P6_3cm$ and $Pbca$, respectively[4]. The chain shift along the c-axis of the $P6_3cm$ and $Pbca$ structures was arranged in an up-up-down and up-up-down-down manner in a unit cell, respectively. However, the phase IV structure was not determined.

Here we closely investigated q-scan profiles on the (h h 2) line of $TlCoCl_3$ and found a small but definite peak at ($\frac{1}{6}$ $\frac{1}{6}$ 2), which appeared only in phase IV (68 K< T <75 K). The representative profiles of (h h 2) from h = 0.1 to h = 0.4 at 86.4 K (phase III), 71.7 K (phase IV) and 60.0 K (phase V) are shown in Fig.1(a). The temperature dependence of the height of ($\frac{1}{6}$ $\frac{1}{6}$ 2) peak is shown in Fig. 1(b). The temperature dependence of ($\frac{1}{3}$ $\frac{1}{3}$ 2) and ($\frac{1}{4}$ $\frac{1}{4}$ 2) peaks that characterize phases III (75 K< T <165 K) and V (T <68 K), respectively, were also measured. As a result, we confirmed that the phase IV structure was characterized by the ($\frac{1}{6}$ $\frac{1}{6}$ 2) peak. We proposed possible crystal structures of phase IV with $2\sqrt{3}a \times 2\sqrt{3}a \times c$ unit cells.

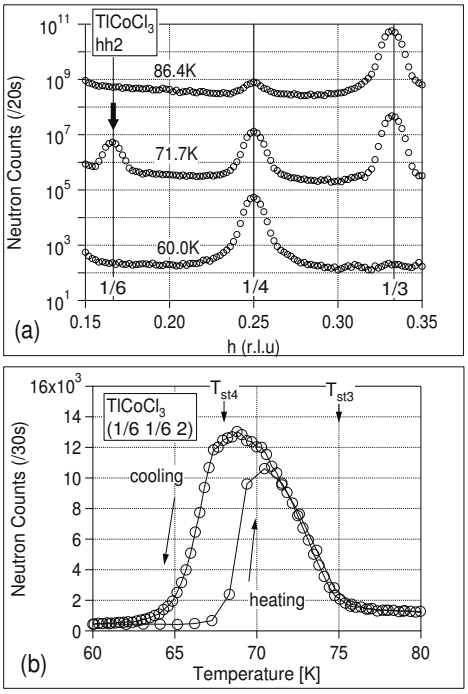

Figure 1: (a) Neutron diffraction intensities of $TlCoCl_3$ scanned parallel to (h h 2) directions at T = 86.4 K (phase III), 71.7 K (phase IV) and 60.0 K (phase V) with deliberately shifted base lines. (b) Temperature dependence of ($\frac{1}{6}$ $\frac{1}{6}$ 2) peak height.

References

1) D. Visser, G. C. Verschoor and D. J. W. Ijdo, Acta Crystallogr. B, 36, 28(1980).
2) K. Yamanaka, Y. Nishiwaki, K. Ito, T. Mitsui, T. Tojo and T. Atake, J. Therm. Anal. Calorim., 70, 371(2002).
3) Y. Nishiwaki, K. Iio and T. Mitsui, J. Phys. Soc. Jpn., 72, 2608(2003).
4) Y. Nishiwaki, T. Kato, Y. Oohara, A. Oosawa, N. Todoroki, N. Igawa, Y. Ishii and K. Ito, J. Phys. Soc. Jpn., 75, 034707(2006).

2.5.3

Location of Deuterium Atoms in $BaSn_{0.5}In_{0.5}O_{2.75}$ by Neutron Powder Diffraction at 77-473 K

T. Nagasaki[1], T. Ito[2], K. Iwasaki[2], M. Yoshino[2], N. Igawa[3] and Y. Ishii[3]

[1] *EcoTopia Science Institute, Nagoya University, Nagoya 464-8603*
[2] *Department of Materials, Physics and Energy Engineering, Graduate School of Engineering, Nagoya University, Nagoya 464-8603*
[3] *Quantum Beam Science Directorate, JAEA, Tokai, Ibaraki 319-1195*

Aliovalently-doped perovskite oxides often show significant proton conductivity in a humid atmosphere at high temperatures[1]. While several computational approaches[2] have yielded consistent results with respect to the hydrogen site in these materials, none of the neutron diffraction studies[3] had verified the results until our latest study[4] revealed that the deuterium atoms in D_2O dissolved $BaSn_{0.5}In_{0.5}O_{2.75}$ at 10 K are located at or very close to the $12h$ site of the perovskite structure (space group $Pm\bar{3}m$) with an O-D distance of 1.0 Å.

In the present study, we measure neutron diffraction patterns of $BaSn_{0.5}In_{0.5}O_{2.75}$ with and without dissolved D_2O at higher temperatures. The diffraction data, especially when analyzed by the maximum entropy method (MEM), might be able to visualize the diffusion paths of hydrogen atoms and/or dynamic disorder (momentary displacement) of other atoms associated with hydrogen diffusion.

The $BaSn_{0.5}In_{0.5}O_{2.75}$ samples with and without dissolved D_2O were prepared by the same procedure as before.[4] The deuterium concentration in the "wet" sample was evaluated to be 0.21 D/Ba by thermogravimetry. The neutron powder diffraction data (λ =1.823 Å) of the samples were collected at 77 K, room temperature and 473 K using a high resolution powder diffractometer (HRPD). The data were analyzed by the maximum entropy method (MEM, program PRIMA) as well as the Rietveld method (program RIETAN-2000)[5,6].

Figure 1 shows the distribution of neutron scattering length density in the "wet" samples obtained by the final MEM analysis after the REMEDY cycle[5,6]. The distribution attributable to deuterium atoms is almost independent of temperature and basically the same as that at 10 K[4], indicating that the deuterium atoms are located at or very close to the $12h$ site with an O-D distance of 1.0 Å at these temperatures. This is the first determination by neutron diffraction of hydrogen position in a proton-conducting oxide at elevated temperatures. On the other hand, we cannot find any features suggesting diffusion paths of deuterium atoms or disorder of other atoms in the scattering length density distributions.

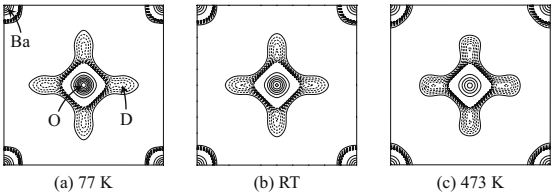

Figure 1: Scattering length density distributions on the (100) plane of D_2O-dissolved $BaSn_{0.5}In_{0.5}O_{2.75}$ at (a) 77 K, (b) RT and (c) 473 K determined by the MEM analysis[7].

References

1) H. Uchida, et al., Solid State Ionics, 34, 103(1989).
2) For example, M. Yoshino, et al., Solid State Ionics, 162-163, 127(2003).
3) For example, N. Sata, et al., Phys. Rev. B, 54 15795(1996).
4) T. Ito, T. Nagasaki, et al., Solid State Ionics, 178, 13(2007).
5) F. Izumi, et al., Mater. Sci. Forum, 321-324, 198(2000).
6) F. Izumi, et al. :"Recent Research Developments in Physics", Transworld Research Network, Vol. 3, Part II, 699(2002).
7) T. Ito, T. Nagasaki, et al., Solid State Ionics, 178, 607(2007).

2.5.4
Observation of CO_2 Molecule in Clathrate Hydrate by Maximum Entropy Method

N. Igawa, T. Taguchi, H. Fukazawa, H. Yamauchi and Y. Ishii
Quantum Beam Science Directorate, JAEA, Tokai-mura, Ibaraki-ken 319-1195

Clathrate hydrates consist of two types of cages (called "large" and "small" cages) formed by water molecules and traps encaging gas molecules inside each cage. The aim of this study is the precise crystal structural analysis of CO_2 hydrate focused on the motion behaviors of the inclusion CO_2 gas molecule in the cages. The neutron diffraction patterns of CO_2 hydrate were measured by using a high resolution powder diffractometer (HRPD) in the temperature range from 10 K to 200 K. A neutron wavelength of 0.1823 nm was used and diffraction data were collected in the 2θ range from 20° to 165° with a step-angle of approximately 0.05°. The obtained diffraction patterns were analyzed by the Rietveld method using the program "RIETAN-2000"[1]. After the Rietveld analysis, the Maximum Entropy Method (MEM) analysis was carried out using the program "PRIMA"[2].

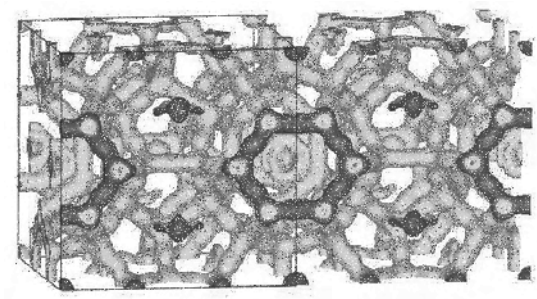

Figure 1: Scattering length density map of CO_2 hydrate at 10 K.

Figure 1 shows the scattering length density map of CO_2 hydrate at 10 K analyzed using MEM. Two unit cells are shown in this figure. The small cage is located at the corner and center of the unit cell and the large cage is located at the faces of the unit cell. Carbon of the CO_2 molecule is observed in the small cage though oxygen is not observed. It is indicated that the CO_2 molecule spins freely around its carbon atom. This behavior is independent of temperature from 10 K to 200 K. Both carbon and oxygen, however, are observed in the large cage: oxygen is distributed around the carbon on the parallel plane to the hexagonal facet of the large cage. Figure 2 shows the temperature dependence of the scattering length density map of the large cage. Although the motion of CH_4 in the large cage of methane hydrate is drastically changes from 10 to 116 K[3], the motion of CO_2 in those of CO_2 hydrate is independent of temperature.

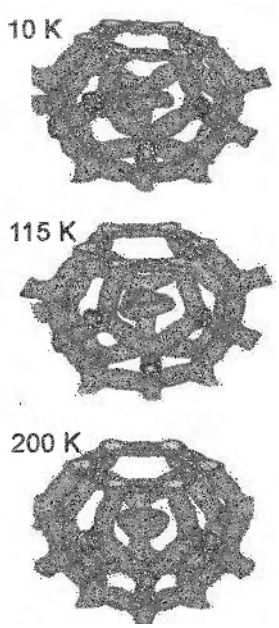

Figure 2: Temperature dependence of the scattering length density map of the large cage of CO_2 hydrate.

References

1) F. Izumi and T. Ikeda, Mater. Sci. Forum, 198, 321(2000).
2) F. Izumi and R. A. Dilanian: "Recent Research Developments in Physics", Transworld Research Network, 3, 699(2002).
3) A. Hoshikawa, N. Igawa, H. Yamauchi and Y. Ishii, J. Phys. Chem. Sol., 66, 1810(2005).

2.5.5

Neutron Study Suggests Ferroelectric Ice in the Universe

H. Fukazawa, H. Yamauchi, N. Igawa and Y. Ishii

Quantum Beam Science Directorate, JAEA, Tokai, Ibaraki 319-1195

In the Galaxy, ice is one of the major solid components in low temperature environment. Ice grains have been identified by infrared spectra in interstellar molecular clouds and in gaseous clouds around low-temperature stars. Big icy planets have been discovered beyond our solar system. Huge ice mass exists on planets and moons, such as Neptune, Uranus, Pluto and Charon, in our solar system. Small bodies like Saturn's rings and comets are also composed of icy grains.

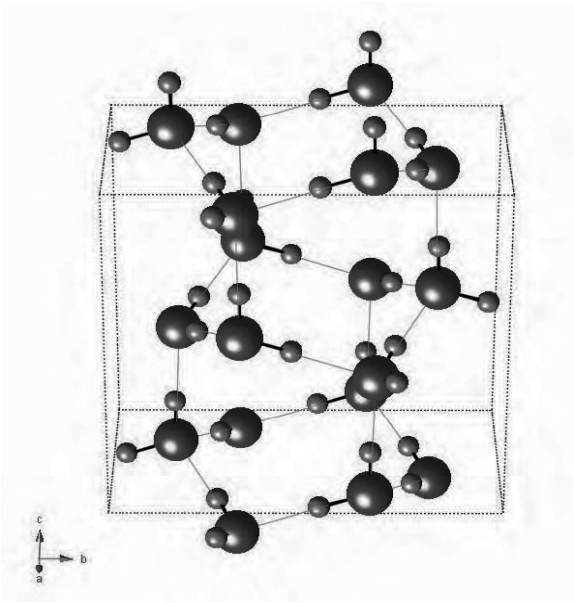

Figure 1: Ice XI with proton-ordered arrangement has small circles that show fully occupied protons. Since water molecules are aligned along c-axis (vertical direction), ice XI has ferroelectricity.

Below 200 MPa, crystalline ice becomes a structure, which named as ice I (one) or ice XI (eleven). Whether ice in the Universe exists as ice XI, is an attracted question, because ice XI is ferroelectric (Fig.1). Long-range electrostatic forces, caused by the ferroelectricity, might be an important factor for planet formation. Furthermore, the grains may play important roles in chemical evolution including the formation of prebiotic organic materials. However, in astronomical observations to identify an icy object, it is not clear whether ice XI exists or not on the surface. Features of the infrared spectrum of ice XI are unknown because of the difficulty in creating perfect ice XI in the laboratory.

We have studied the conditions required for the formation of ice XI. In 06' we measured diffraction profiles of ice with many kinds of dopants using a high resolution powder diffractometer (HRPD). We carefully created samples of ice that contained impurities, which assisted the ice XI conversion process a catalyst. The results indicate that ice with an ionized defect (OH^-) transforms to an enough ice XI after several hundred hours. We studied an irradiated ice. The gamma- and UV-irradiation also creates OH^-. The detailed analysis is in progress.

Normal ice naturally has a small amount of the defect. Thus, without adding the impurity compound, it would take 10,000 years for normal ice to transform into ice XI. While this time scale is much longer than what can be measured in a laboratory, it is not too long in the astronomical time scale. Furthermore, cosmic rays assist the formation. Thus, we expect that ice XI exists in the Universe[1]. We reported this research in the press and it was taken up by the mass media[2]. We hope that it would spur astronomers to find frerroelectric ice XI in the future.

References

1) H. Fukazawa, et al., Astrophys. J. Lett., 652, 57(2006).
2) Science, 315, 18(2007).; Physorg.com, ⟨http://physorg.com/news83862687.html⟩.; Japanese newspapers (Joyo shimbun, 1/12, (2007).; Kagaku shimbun, 1/19, (2007).; Asahi shimbun, 2/22, (2007).).

This is a blank page

2.6 Materials Science and Industrial Applications

Microstructure and Residual Stress

This is a blank page

2.6.1
Analysis of Crystal $LiMn_2O_4$ Size in Composite Sample by Neutron Scattering

K. Basar, Xianglian, S. Siagian, K. Ohara, T. Sakuma, H. Takahashi[1], O. Abe[2], N. Igawa[3] and Y. Ishii[3]

Institute of Applied Beam Science, Ibaraki University, Mito 310-8512, Japan
[1]*Institute of Applied Beam Science, Ibaraki University, Hitachi 316-8511, Japan*
[2]*Faculty of Engineering, Ibaraki University, Hitachi 316-8511, Japan*
[3]*Japan Atomic Energy Agency, Tokai 319-1195, Japan*

Lithium metal transition compounds are promising materials for cathodes in lithium-ion batteries. In this group of materials, $LiMn_2O_4$ is an attractive and important material because it is relatively cheaper and less toxic. We report the use of a neutron scattering experiment to analyze the anneal temperature effect on the crystalline size of composite $LiMn_2O_4$.

The sample was prepared by dry mixing of LiOH and MnO_2 then milled for 3 hours at frequency of 2 Hz to perform a ground product. After that, the mixture was heated at temperature 200°C for 16 hours. To analyze the anneal temperature effect on the crystalline size of $LiMn_2O_4$ in the composite samples, we divided the whole sample into three parts: sample A annealed at 400°C for 3 hours, sample B annealed at 500°C for 3 hours and sample C annealed at 800°C for 3 hours. Neutron scattering measurements at room temperature have been performed for samples A, B and C by HRPD. The data were collected in the 2θ range from 20° to 150° with step angle of 0.05°.

Figure 1 shows the neutron scattering intensity of powder $LiMn_2O_4$ composites for samples A, B and C. Rietveld analysis has been performed on the neutron scattering intensities of samples A, B and C using RIETAN-2000[1)]. The crystal of $LiMn_2O_4$ is assumed to belong to cubic type structure with a space group Fd3m[2)]. The full-width of half maximum of Bragg lines of $LiMn_2O_4$ in the samples A, B and C shows a tendency to decrease with increasing the annealing temperature. The average crystallite sizes of $LiMn_2O_4$ were calculated using Scherrer equation. The obtained average size of a crystal $LiMn_2O_4$ in the composite samples are about 5, 20 and 130 nm for samples A, B and C, respectively. In a former report of $LiNiO_2$, the temperature dependence of diffuse scattering intensity decreases drastically with increasing annealing temperature. The strong diffuse scattering intensity was related to the amount of starting material LiOH in the composite samples[3)]. However, in the case of $LiMn_2O_4$, the diffuse scattering intensity does not change so much in samples A, B and C. The amount of starting material LiOH is very small even in sample A.

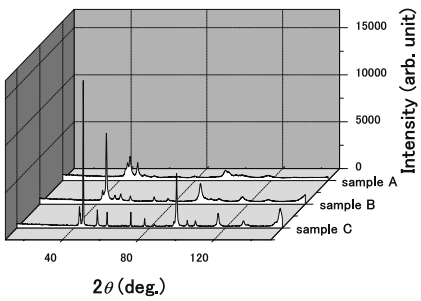

Figure 1: Neutron scattering intensities of powder $LiMn_2O_4$ composites at room temperature.

References

1) F. Izumi and T. Ikeda, Mater. Sci. Forum, 321-324, 198(2000).
2) K. S. Yoo, N. W. Cho and Y. J. Yo, Solid State Ionics 113-115, 43(1998).
3) K. Basar, Xianglian, H. Honda, T. Sakuma, H. Takahashi, O. Abe, N. Igawa and Y. Ishii: "Proceedings of the 10th Asian Conference on Solid State Ionics, Kandy, Sri Lanka 2006, eds B. V. R. Chowdari, et al.", World Scientific, 121(2006).

2.6.2
Magnetic Structures in $Mn_3Cu_{1-x}Ge_xN$: Evidence for the Close Relationship with Magneto-volume Effect

S. Iikubo[1], K. Kodama[1], K. Takenaka[2,3], H. Takagi[2,3] and S. Shamoto[1]

[1] *Quantum Beam Science Directorate, Japan Atomic Energy Agency, Tokai, Ibaraki, 319-1195, Japan*
[2] *RIKEN (The Institute of Physical and Chemical Research), Wako, Saitama 351-0198, Japan*
[3] *CREST, Japan Science and Technology Agency, Kawaguchi, Saitama 332-0012, Japan*

Recently, Takenaka and Takagi reported that the Magneto-Volume Effect (MVE) is broadened against T in $Mn_3Cu_{1-x}Ge_xN$ leading to a giant negative thermal expansion (NTE) coefficient[1)]. NTE materials have already been used in a wide area of technical applications. While the volume change is negligibly small at ferromagnetic transition T_C = 143 K in Mn_3CuN, a large first order phase transition MVE appears at $T_C \sim 100$ K at $x = 0.15$. With increasing x, the magnetic transition temperature increases and the increase in the volume is broadened in T. At $x \sim 0.5$, the large negative thermal expansion coefficient is about $\alpha \sim -2 \times 10^{-5}$/K in the temperature range of $270 \leq T \leq 350$ K, whose amplitude is one of the largest ones in all NTE materials. Basically, the volume can be expanded according to the change in the amplitude of magnetic moment. Although Fruchart and Bertaut classified the magnetic properties of Mn_3AN system by the number of valence electrons on A ion[2)], there is no simple relationship between the magnitude of MVE and the valence electron number. In order to study the microscopic magnetic properties and MVE, neutron diffraction studies have been carried out.

Polycrystalline samples of $Mn_3Cu_{1-x}Ge_xN$ were prepared by a solid state reaction[1)]. The experiments were performed on the high-resolution powder diffractometer HRPD (λ=1.8233 Å) and the triple axis spectorometer TAS-2 (λ=2.3590 Å) installed at JRR-3 of JAEA. Their collimations were open (effective value of 35')-20'-6' and 14'-40'-40'-80', respectively. Powder samples of $Mn_3Cu_{1-x}Ge_xN$ weighing ~7 g were set in vanadium holders, which were enclosed in Al cans filled with He gas. They were mounted in a closed-cycle refrigerator below room temperature and in a furnace above room temperature. The obtained results are summarized as a T-x phase diagram of crystal and magnetic structures as shown in Fig. 1. Magnetic transition temperatures determined by neutron diffraction studies and magnetization measurements are plotted by closed circles and open circles, respectively. The present neutron study revealed that cubic crystal structure and Γ^{5g} anti-ferromagnetic spin structure are key ingredients for the large magneto-volume effect in this itinerant electron system, while it is negligibly small in a tetragonal and ferromagnetic phase. This experimental result proposes the necessity of new theoretical framework on MVE, which takes account of the ordered magnetic structure[3)].

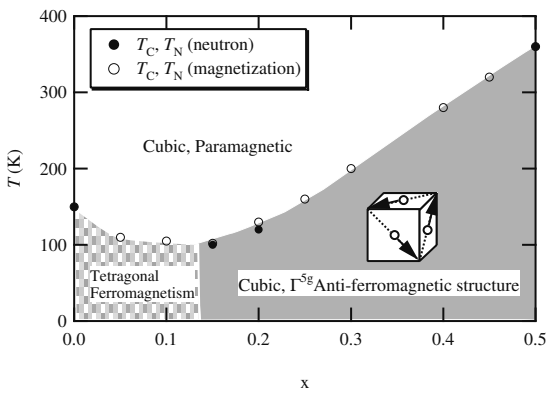

Figure 1: T-x phase diagram of crystal and magnetic structures on $Mn_3Cu_{1-x}Ge_xN$.

References

1) K. Takenaka and H. Takagi, Appl. Phys. Lett., 87, 261902(2005).
2) D. Fruchart and E. F. Bertaut, J. Phys. Soc. Jpn., 44, 781(1978) .
3) S. Iikubo, K. Kodama, K. Takenaka, H. Takagi and S. Shamoto, in preparation.

2.6.3
Standardization of Residual Stress Measurement Method of Weld Section †

T. Kurimura[1], S. Okido[2] and H. Suzuki[3]

[1] *Mitsubishi Heavy Industries, Ltd., Takasago, Hyogo 676-8686*
[2] *Hitachi, Ltd., Hitachi, Ibaraki 317-8511*
[3] *Japan Atomic Energy Agency, Tokai, Ibaraki 319-1195*

A welding structure is widely accepted in large scale structures and it is inevitable to take residual stresses into account for their life estimation. Residual stress measurement using the diffraction method is well accepted but there are some difficulties to measure the residual stress in a weld area. To establish the guidelines for the residual stress measurement in a weld area using diffraction method, butt welds SM570 and SUS304 are prepared to estimate the residual stress by neutron diffraction method with having connection with the sub-committee activity in the society of material science Japan.

Residual stress was determined in longitudinal (parallel to the weld line), transverse (perpendicular to the weld line) and normal to the surface directions. Measurements were conducted at depths of 2 mm and 4 mm. For example, Fig.1 shows the residual stress distribution in longitudinal direction for both SM570 and SUS304. The trends of both measurements are similar.

(211) diffraction was used for SM570 with elastic constants of E_{220} = 224 GPa and ν_{220} = 0.28 calculated by the Kroner model. (220) diffraction was used for SUS304 with elastic constants of E_{220} = 211 GPa and ν_{220} = 0.27 calculated by the Kroner model. The error of each measurement was 30 MPa to 100 MPa, and hence, the accuracy of the measurement is acceptable.

The error of the measurements form the weld area is slightly larger than that from other areas. In the weld area, stress distribution in the depth direction was also observed.

These results will be compared with the results of X-ray residual stress measurements from round-robin tests and FEM analysis and stress relief method conducted by a subcommittee activity in the Society of Material Science Japan to establish a guideline for the residual stress measurement of the weld structure using the diffraction method.

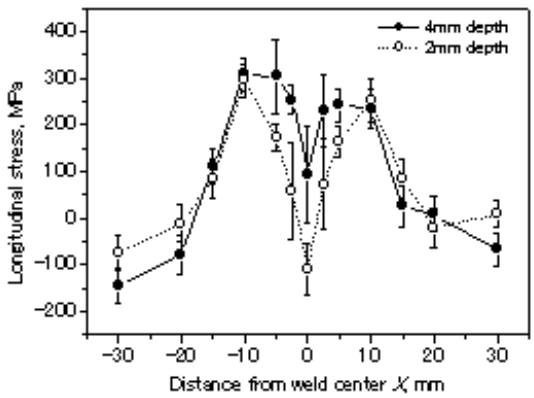

(a) SM570

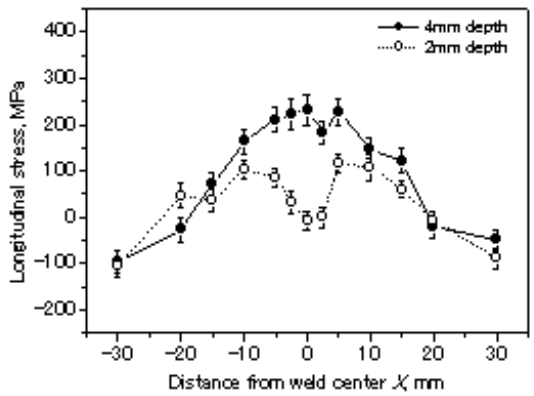

(b) SUS304

Figure 1: Residual stress measurement of butt weld structure.

† Common use program of JAEA

2.6.4

Ferroelectric Phonon Mode in Relaxor $K_{1-x}Li_xTaO_3$

S. Wakimoto, G. A. Samara[1], R. K. Grubbs[1], E. L. Venturini[1], L. A. Boatner[2], G. Xu[3] and G. Shirane[3]

Quantum Beam Science Directorate, JAEA, Tokai, Ibaraki 319-1195
[1]*Sandia National Laboratories, Albuquerque, New Mexico 87185, USA*
[2]*Oak Ridge National Laboratory, Oak Ridge, Tennessee 37831, USA*
[3]*Brookhaven National Laboratory, Upton, New York 11973, USA*
[4]*Department of Physics, University of Virginia, Charlottesville, Virginia 22904, USA*

Relaxor $K_{1-x}Li_xTaO_3$ (KLT) shows rich dielectric properties. The system is quantum paraelectric at $x = 0$. With substitution of a small amount of K^+ ions with Li^+ the system shows relaxor behavior, and then further substitution triggers ferroelectric transition. Although the relaxor behavior is expected to arise from the relaxational behavior of the off-center Li ions, the role of the zone-center transverse-optic ferroelectric (FE) mode is not well understood yet. Last year, we have studied the diffuse scattering and the FE mode in the relaxor KLT with $x = 0.05$ and found atomic displacements arising from the condensation of the FE mode superimposed on the uniform phase shift, same as the case of $Pb(Mg_{1/3}Nb_{2/3})O_3$ (PMN), indicating the contribution of the ferroelectric mode.

We have performed neutron scattering experiments at the TAS-2 triple axis spectrometer to study the FE mode in the KLT ($x = 0.10$) sample which shows the ferroelectric transition at 110 K with an intent to confirm the phonon contribution to the dielectric behavior in KLT.

Dielectric measurements indicate the ferroelectric transition of the $x = 0.10$ sample at $T_c = 110$ K. This has been confirmed by the neutron scattering measurements showing that the nuclear Bragg peak width and intensity increase rapidly below 110 K, suggesting a transformation of the lattice into a lower symmetry due to the ferroelectric transition. However, the crystal structure probed by the neutron scattering with a tight collimation sequence, 15'-10'-20'-10', is cubic in average even below T_c, implying that only a small portion of the sample is ferroelectrically transformed.

The FE mode has been measured with the collimation sequence of 15'-80'-80'-open. Figure 1 shows the phonon the energy squared as a function of temperature for KLT $x = 0.10$ and 0.05. We have found that the $x = 0.10$ sample exhibits an additional phonon mode which hardens below T_c as shown by the open squares. We assign this as an FE mode originating from the ferroelectrically ordered region. Such hardening of the FE mode below T_c has been observed in the displacive ferroelectic materials such as $PbTiO_3$, and relaxors, PMN and $Pb(Zn_{1/3}Nb_{2/3})O_3$ (PZN).

We have detected the hardening of the FE mode below T_c in the relaxor KLT for the first time. Combined with similar results for the relaxors PMN and PZN, it is shown that the FE mode has an important role in the perovskite relaxors.

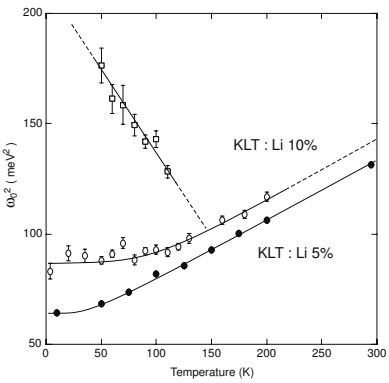

Figure 1: Squared phonon energy of the zone-center transverse optic phonon as a function of temperature for KLT10 % (open symbols) and KLT5 % (black circles).

2.6.5

Intergranular Strain Pole Figure Measurement for ECAPed Al by Neutron Diffraction

T. Suzuki[1], T. Ishibashi[1], Y. Tomota[1], H. Suzuki[2], T. Saito[2] and S. Ryufuku[3]
[1] *Ibaraki University,* [2] *JAEA,* [3] *VIC Inc.*

Texture and intergranular stresses are evolved in polycrystalline materials subjected to plastic deformation due to heterogeneous plastic flow. In general, pole figures are measured by X-ray diffraction to evaluate the anisotropic mechanical properties of plastically deformed materials, which is not sufficient. In this study, a neutron diffraction method has been developed to determine the texture as well as intergranular strains called "strain pole figure" for a bulky sample.

A 4N graded pure aluminum bar with 8 mm in diameter and 60 mm in length was ECAPed up to 8 cycles by rotating by 90 degrees at each extrusion. The (*hkl*) intergranular strains and texture were measured by using RESA at JAEA. The specimen was rotated by 10° steps for texture measurement and 45° steps for residual strain measurement. And measurements were conducted a gauge volume to measure diffractions from (111), (200) and (220) was adjusted completely inside the sample.

Figure 1 shows the results of texture and *hkl* intergranular strains. As shown, the ECAPed aluminum shows an asymmetric texture. Residual intergranular strains are observed depending on the texture, and different in the case of three (*hkl*) oriented family grains. Although the stacking fault energy of aluminum is high, the misfit plastic strains among grains, i.e., heterogeneous plastic flow, seem to be yielded resulting in the generation of internal stresses.

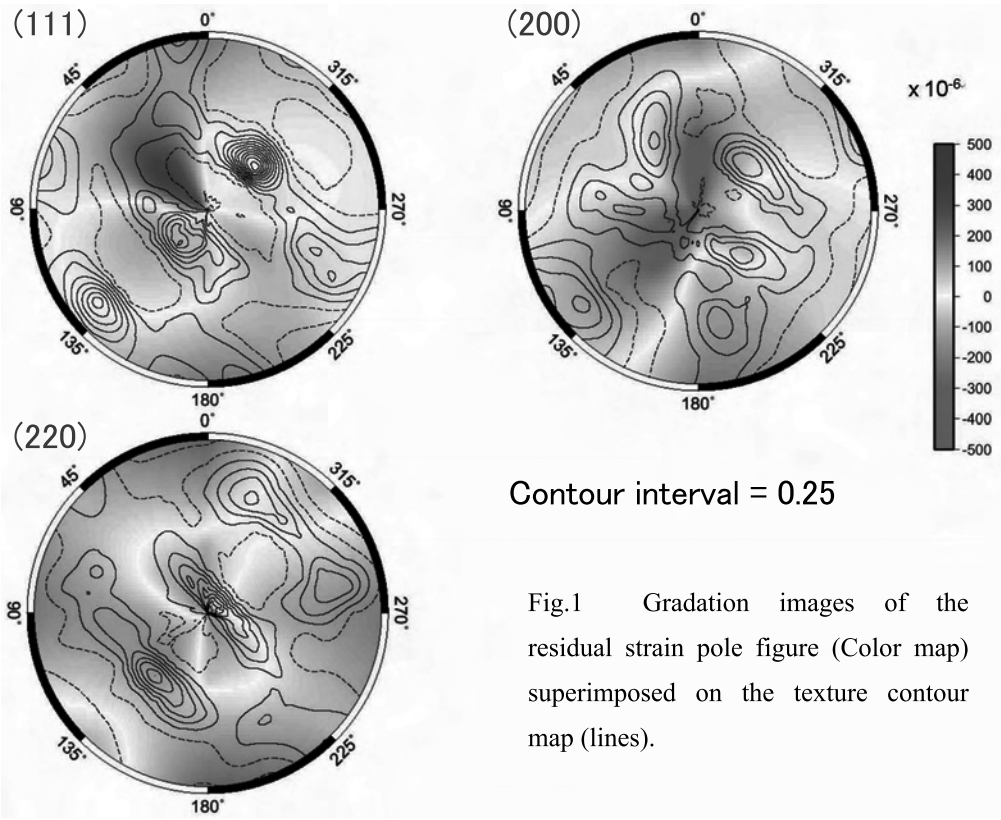

Fig.1 Gradation images of the residual strain pole figure (Color map) superimposed on the texture contour map (lines).

2.6.6

Assessment of Vanadium Alloys

A. Hoshikawa, S. Kakei[1], H. Yoshinaga[1], T. Ishigaki and T. Kamiyama[2]

J-PARC Center, Tokai, Ibaraki 319-1195
[1]*Ako Laboratory, Taiyo Koko Co., Ltd., Ako, Hyogo 678-0232*
[2]*Institute of Materials Structure Science, KEK, Tsukuba, Ibaraki 305-0801*

A sample holder is necessary for neutron powder diffraction measurements. Vanadium is usually used as the sample holder. Since the coherent scattering length of vanadium is not zero but a small negative value (-0.443 fm), Bragg peaks from the sample holder cannot be neglected in the future. In the Japan Proton Accelerator Research Complex (J-PARC) project, high-intensity neutron beams are going to be produced with MW-class high power pulsed proton beams. Therefore, it is important to develop materials for the sample holder. Recently, a metal with a positive coherent scattering length is mixed with vanadium and some new vanadium alloys are synthesized (V-Al, V-Cr, V-Fe and V-Ni alloys). It is necessary to check these vanadium alloys. Therefore, we investigated these vanadium alloys using a high resolution powder diffractometer (HRPD) at JRR-3.

Measured samples were V, V-Al, V-Cr, V-Fe, V-Ni and V-Nb alloys. For the control experiment, we prepared V, which is pure vanadium, and V-Nb alloy confirmed as a 'null alloy'. Here, 'null alloy' is an alloy whose coherent scattering length is zero. These samples were supplied by Taiyo Koko Co., Ltd. (Japan). We used bulk samples and typical sample dimensions were $23\times23\times5$ mm^3. These samples are rotated during measurement. The 1st collimator before the Ge monochromator was opened because of high intensity. Each sample was measured for a day and data were collected over the 2θ range of 2.5–160° because of ascertaining the presence of impurity phase.

Neutron powder diffraction patterns are shown in Fig.1. Tick marks in the figure show the peak positions of vanadium. Some Bragg peaks are clearly observed for V. In powder diffraction patterns except V, there is no vanadium peak and no other Bragg peak. Accordingly, we confirmed that these vanadium alloys were 'null alloy'. Next, we should investigate workability for the sample holder.

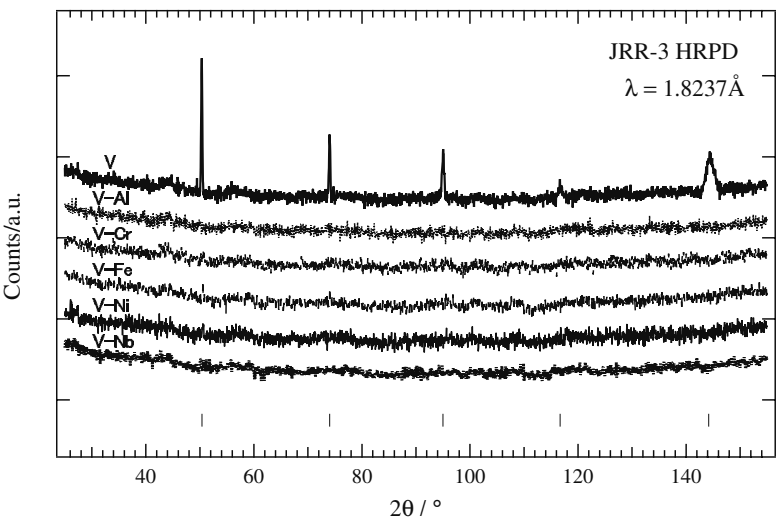

Figure 1: Neutron powder diffraction patterns of vanadium alloys.

2.6.7
Detection of Hydrogen Trapped by Nano-scale Carbide by SANS

M. Ohnuma, F.G. Wei*, K. Tsuzaki* and J. Suzuki[1]

*Quantum Beam Center and *Structural Metals Center, NIMS, Tsukuba 305-0047*
[1]*Quantum Beam Science Directorate, JAEA, Tokai 319-1195*

Even a trace amount of hydrogen (H) can cause a premature fracture in high strength steels through concentrating at microstructural heterogeneity. Suppressing a diffusive H-concentration is one of the approaches to reduce the susceptibility of hydrogen embrittlement by introducing a nano-carbide (VC, TiC, NbC, etc.) as a H-trap site. A quantitative correlation of the dimensions of nano-sized TiC to the amount of trapped H suggests that H is trapped at the TiC/matrix interface[1)]. However, due to the difficulty of detection of H and monoatomic layer segregation, no structural evidence has been obtained yet. SANS is one of the suitable techniques for detecting H-segregation in a nanoscale substance. Therefore, we measured SANS of 97.62Fe-0.23C-0.25Nb-1.90Ni(at%) alloy with and without H.

The alloy was annealed at 873 K for 10800 sec for forming coherent nano-size NbC. NbC was chosen since it has the same crystal structure as TiC while it gives a larger scattering contrast of H compared to the TiC. 20 × 20 mm^2 plate samples with 2 mm thickness were cathodically charged with H. The concentrations of H in charged samples after the SANS experiment were 0.03 at% (6 *wt* ppm). Two different SANS experiments were conducted to determine the effect of H and to confirm reproducibility. In the 1st experiment, two pieces of samples with and without H-charge were adopted. In the 2nd experiment, the sample with H-charge was measured and then annealed at 473 K for 6000 sec for desorbing H. After the heat treatment, the sample was re-measured as a H-free sample. Because the alloy is ferromagnetic, we applied the magnetic fields of 1 T (1st ex.) and 0.5 T (2nd ex.) for separating nuclear and magnetic components of the scattering.

Figure 1 shows the nuclear components of the SANS profiles obtained from parallel direction to the magnetic field. The difference between the alloys with and without H is detected as shown in Fig.1. In both experiments, the profiles of the alloys with H show higher intensity than those without H with good reproducibility. In the 2nd experiment, the H-charged sample shows same profiles with that of the 1st experiment, while the same sample shows weaker scattering intensity after annealing at 473 K. The possible origin of the change is only the difference of H-concentration. The difference of the intensity can be explained by both H-segregation at the interface of TiC/matrix and trapped H inside TiC precipitates. Although wider q-range measurements are required for determining which trap site is dominant, the results show the high potential of SANS to detect the trapped H even in the case that the total amount of H is in the *wt* ppm range.

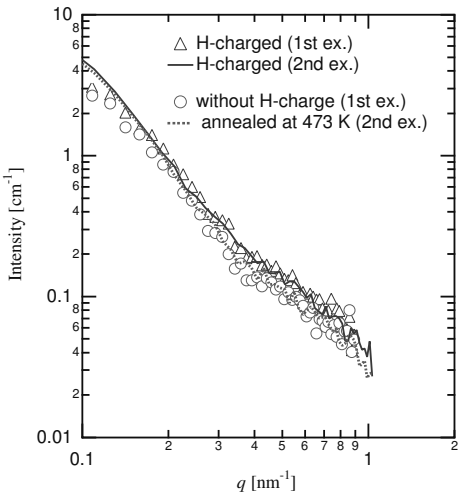

Figure 1: Nuclear components of SANS profiles. ◯ & dotted curve: without H, △ & solid curve : with H

References

1) F. G. Wei and K. Tsuzaki, Metal. Mater. Trans. A, 37, 331(2006).

2.6.8

Measurement of Inclusions in Steel by Small Angle Neutron Scattering †

S. Morooka[1], Y. Tomota[1], J. Suzuki[2], M. Ohnuma[3], K. Kikuchi[4] and T. Shiraga[4]

[1] *Ibaraki University,* [2] *JAEA,* [3] *NIMS,* [4] *JFE Bars Shapes Corporation.*

Improvement of fatigue resistance is a key issue to employ high strength steels safely, where the detection of inclusions is of importance because fatigue crack is often initiated from an inclusion. Several methods to measure the size and amount of inclusion in steel have been developed so far, but these are time-consuming and have encountered difficulties in terms of reliability, bulky averaged information and non-destructive inspection. Small angle neutron scattering (SANS) seems to enable us to determine the size and amount of inclusion quantitatively by using a bulky sample non-destructively. Hence such a trial has been made in this study by employing commercially available steels.

Various kinds of steels were measured, in which elongated MnS and/or nearly spherical Al_2O_3 particles exist. The microstructure of the matrix is made of ferrite, ferrite-pearlite or pearlite. The small angle neutron scattering measurement was performed with SANS-J II at JAEA under a magnetic field of 1 T at RT. The size of the sample was 30 × mm × 20 mm × 2 mm (thickness).

Figure 1 presents the result obtained from the steel with 1.0 mass % carbon, containing Al_2O_3 particles. The scattering intensity obtained in the vertical direction of a two-dimensional detector consists of magnetic and nuclear scatterings. Since the steel is ferromagnetic, the microstructural information can be discussed from the nuclear scattering (horizontal data). As the Guinier region is clearly found around q^{-1}=0.001 A^{-1} in Fig.1, the lnI(q)-q^2 plot gives the inclusion diameter of approximately 0.1 μm which is comparable with optical microstructure observations. However, the curve fitting taking a size distribution around 0.1 μm into account suggests that there exists much larger particles, the scattering from which must be overlapped. The influence of the matrix microstructure, i.e., cementite, is also observed. In the case of elongated MnS with a size of larger than 1 μm, further improvements in the measuring system are needed. Commercially available steel is too complicate, and hence it must be possible to determine the size distribution of inclusion if the suitable calibration data for simple standard specimens are prepared. Nevertheless, the present results indicate a high potency to evaluate the reliability of structural steels by SANS measurements.

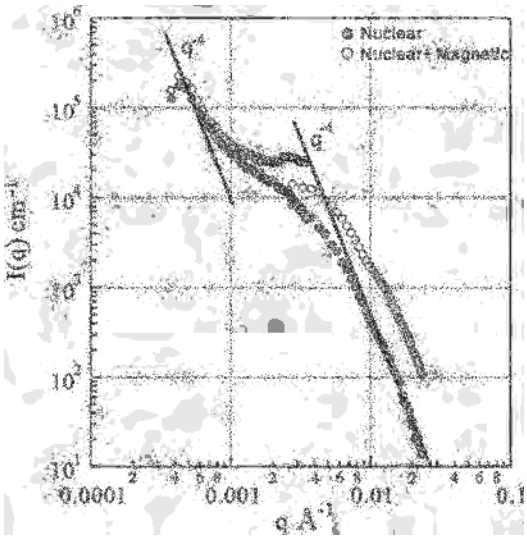

Figure 1: An obtained example of SANS profile.

† Common use program of JAEA

2.6.9

Evaluation of Magnetization on $Fe_{16}N_2$ Nanoparticles by Polarized Neutrons Diffraction

Y. Ishii[1,2], M. Takeda[1], K. Kakurai[1], T. Kikuchi[1,2], T. Shinohara[1], T. Oku[1], J. Suzuki[1], Y. Sasaki[3], M. Kishimoto[3], M. Yokoyama[2] and Y. Nishihara[2]

[1] *Quantum Beam Science Directorate, JAEA, Tokai, Ibaraki 319-1195*
[2] *Department of Science, Ibaraki University, Mito, Ibaraki 310-8512*
[3] *Hitachi Maxell, Ltd., Koizumi, Oyamazaki-Cho, Otokuni-Gun, Kyoto 618-8525, Japan*

Needle-shaped ferromagnetic metals are often used for magnetic recording tapes. It is, however necessary to make small and spherical shape to increase the recording capacity and density. Recently, $Fe_{16}N_2$ round nanoparticles with a diameter of 20 nm were produced by Hitachi Maxell, Ltd.. But it is difficult to obtain exact magnitude by a conventional magnetometer due to the laminated layer around $Fe_{16}N_2$. We performed polarized neutron diffraction measurements to determine net magnetization.

The averaged diameters of samples used in these experiments are approximately 19 and 17 nm. The triple-axis neutron spectrometer, TAS-1, installed at JRR-3 was used in this experiment. The neutron energy was fixed at 14.7 and 80 meV. A magnetic field of 10 kOe was applied to the samples during measurements to saturate the magnetization. The direction of neutron spin was turned for a parallel or anti-parallel state to the saturated magnetization vector by a spin flipper, and the number of neutrons were recorded in each case (I_+ and I_-). The magnitude of ferromagnetic moments appear as a difference $\Delta I = I_+ - I_-$. The magnetic form factor was determined using known crystal structure factors and ΔI. The magnitude of magnetic moments was determined from the magnetic form factor and flipping ratios, $fr = I_+/I_-$

Figure 1 shows the ΔI of the sample with a diameter of 19 nm. This measurement was performed with 80 meV neutrons. The simulation in Fig.1 drawn by a solid line, it is assumed that the magnetic form factor of Fe in $Fe_{16}N_2$ is the same as that in α-Fe. The experimental data are well reproduced by the simulated curve. Thus, it is concluded that the magnetic form factor is very similar to α-Fe.

Figure 2 shows I_+ and I_- in the vicinity of (202) and (220) Bragg peaks of the sample with the diameter of 19 nm. This diffraction pattern was obtained using 14.7 meV neutrons. The flipping ratios were calculated using the height of each Bragg peak. The magnitude of magnetic moments of $Fe_{16}N_2$ can be deduced without any information on the laminated layer from the results of Fig1 and 2. The same measurements were performed for the sample with a diameter of 17 nm. The magnetization measurements using the magnetometer had given different values of saturation magnetization for these two samples. The polarized neutron diffraction measurements, however, revealed that both $Fe_{16}N_2$ nanoparticles have the same magnitude of the magnetic moments of 2.0 μ_B.

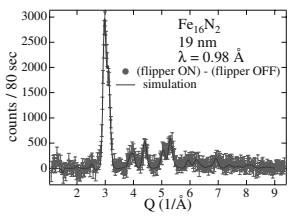

Figure 1: Difference $\Delta I = I_+ - I_-$ and simulation.

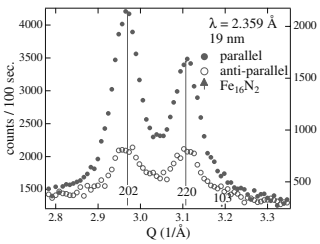

Figure 2: Experiment by polarized neutrons difraction at $\lambda = 2.37$Å.

2.6.10
Magnetic Structure of Fe-N Nanoparticles for Magnetic Recording Tape Studied by Small-angle Polarized Neutron Scattering

T. Kikuchi[1,2], T. Oku[1], T. Shinohara[1], J. Suzuki[1], Y. Ishii[1,2], M. Takeda[1], K. Kakurai[1], Y. Sasaki[3], M. Kishimoto[3], M. Yokoyama[2] and Y. Nishihara[2]

[1] *Quantum Beam Science Directorate, JAEA, Tokai Ibaraki 319-1195*
[2] *Department of Science, Ibaraki University, Mito Ibaraki 310-8512*
[3] *Hitachi Maxell, Ltd., Koizumi, Oyamazaki-Cho, Otokuni-Gun Kyoto 618-8525, Japan*

$Fe_{16}N_2$-based spherical Fe-N nanoparticle has attracted considerable attention as new material for magnetic recording tapes owing to its large magnetic anisotropy and the possibility of the emergence of large magnetic moment. However, evaluation of the local magnetic moment is difficult by magnetization measurement, because the surface of the Fe-N nanoparticle is covered with structurally unknown non-magnetic laminate layer for the oxidation prevention. In order to evaluate the inner magnetic structure of the nanoparticle precisely, we have performed small-angle polarized neutron scattering experiments using the SANS-J-II instrument of JRR-3. We applied a magnetic field of 1 T to samples and measured SANS intensities of I^+ and I^- in the cases that the spin polarity of incident neutrons is positive and negative, respectively. Fig.1 shows scattering profiles $I_\perp^+$ and $I_\perp^-$ along the direction perpendicular to the applied magnetic field, respectively We analyzed these scattering profiles using a model of spherical nanoparticles with a core-shell structure under the assumption of the magnetic moment of 2.1 μ_B/Fe atom. We evaluated the mean radius $\bar{r}$, non-magnetic layer's thickness Δr, and magnetization of the nanoparticles m and compared them with the results obtained by TEM and magnetization measurements as shown in Fig.2. These characteristic parameters were analyzed as a function of the effective polarization degree of the incident neutrons P_{eff} with the accuracy χ^2 of the profile fitting, because there was the possibility that the spin of the incident neutrons was depolarized by the local magnetic field produced in the sample. χ^2 was minimized at P_{eff} of 50 %, and evaluated $\bar{r}$ and m are consistent with the results of macroscopic measurements. Analytical accuracy of the internal magnetic structure of the nanoparticles will improve by determining the depolarization correctly in the future.

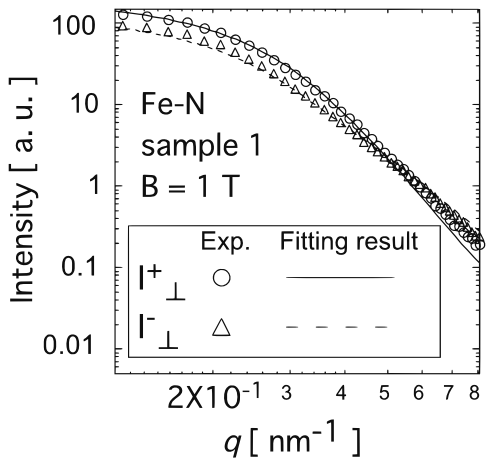

Figure 1: Sans intensities vs. q.

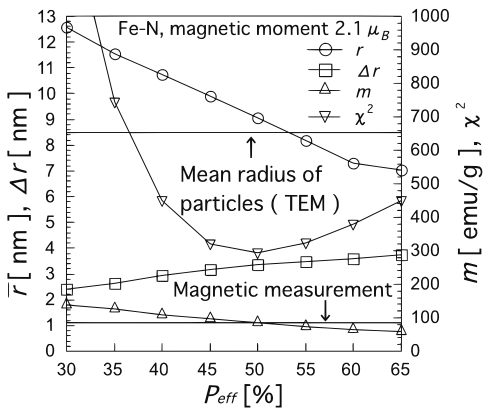

Figure 2: Evaluated $\bar{r}$, Δr, and m as a function of P_{eff}.

2.6.11
Quantitative Evaluations of Microstructural Factors by Neutron Diffraction for Cold Rolled austenitic Stainless Steels

H. Suzuki, T. Saito, J. Y. Tomota[1], T. Suzuki[1], P.-G. Xu[1] and S. Ryufuku[2]

Quantum Beam Science Directorate, JAEA, Tokai, Ibaraki 319-1195
[1]*Ibaraki University, Hitachi, Ibaraki 316-8511*
[2]*VIC, Inc, Tokai, Ibaraki 319-1112*

Cold rolled stainless steels show anisotropic mechanical properties which are dependent on texture, substructure (dislocation structure and density) and intergranular stresses, and hence, it is expected to determine these microstructural factors as macroscopically averaged values. Neutron diffraction enables us to measure these values for cm-ordered bulky specimens. In this study, texture measurements and profile analysis were simultaneously performed to determine the above microstructural factors by an angler dispersion neutron diffraction method for two stainless steels.

The samples used in this study were a 316 type stainless steel without N addition, 316SS, and a 0.325 mass% N bearing 310 type stainless steel, 310SS. After solution treatments to obtain a single austenitic phase, the specimens were subjected to 25% cold rolling. The diffraction profiles of (111), (200) and (220) reflections were measured using the neutron diffractometer for residual stress analysis (RESA) located in JRR-3 at Japan Atomic Energy Agency in Japan. Texture and residual strains were determined by the conventional method, and the dislocation density and the block size were analyzed for the diffraction profiles of (111) reflection using a profile analysis software developed by Ryufuku et al.

Figure 1 shows the gradation images of the intergranular strain pole figure superimposed on the texture contour map for (200) reflections. The textures obtained for 316SS and 310SS are the typical rolling texture of austenitic stainless steels showing little difference. A significant difference between 316SS and 310SS is found in the intergranular strain pole figure; the strain of 310SS is higher than that of 316SS. This large difference in the intergranular stain must be explained by the difference in substructure which is mainly caused by nitrogen addition. That is, the planer dislocation array and network including Lomer-Cottrell immobile dislocations reaction has been observed in 310SS while dislocation cell structure in 316SS. Being consistent with Ikeda et al.'s work of in situ neutron diffraction study for 310SS with different N contents, higher intergranular stresses evolve in a higher N bearing steel. Although the dislocation structure is different in the present two steels, the dislocation density determined from the profile analysis was almost the same, i.e., approximately $2.0 \times 10^{15}/\mathrm{m}^2$, and it gradually decreased with increase in angle from normal direction. To be noted is the comparison of the crystal orientation pole figure and the strain pole figure, where the compressive and tensile residual strains are closely related to the crystal orientation density.

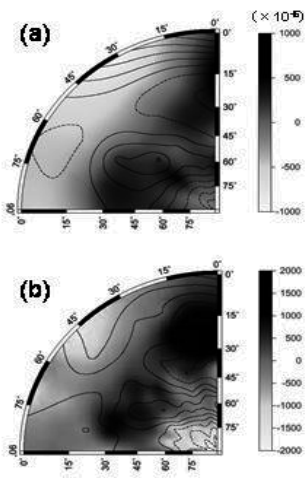

Figure 1: Gradation images of the intergranular strain pole figure superimposed on the texture contour map for (200) reflections of (a) 316SS and (b) 310SS.

This is a blank page

2.7 Fundamental Physics Interferometry

This is a blank page

2.7.1
A Development of the Neutron Beta Decay Experiment with Superconducting Tunnel Junction (STJ)s

K. Mishima, H. Sato, S. Yamada[1], T. Shinohara[1], T. Oku[1], J. Suzuki[1] and H. M. Shimizu[2]

RIKEN, Nishina Center, Wako, Saitama 351-0198
[1]*Quantum Beam Science Directorate, JAEA, Tokai, Ibaraki 319-1195*
[2]*KEK, Tsukuba, Ibaraki 305-0801*

Neutron beta decay is the best reaction to determine the coupling constant of a weak interaction, because the decay is independent of any nuclear structure and is then the simplest and only semileptonic reaction through the weak interaction. From the decay parameters such as lifetime or energy spectra of decay products, we can obtain V_{ud}, a matrix element of Cabbibo-Kobayashi-Maskawa (CKM) matrix, which describes the mixing between quark mass eigenstates and weak eigenstates. A CKM matrix obeys unitarity in the standard model of particle physics[1)]. Our research goal is to determine V_{ud} by a precise spectroscopy of recoil proton and electron from neutron beta decay.

However, the spectroscopy of a recoil proton is difficult because its kinetic energy is very small, whose maximum energy is 752 eV, so that it is hardly detected by semiconductive detectors like SSD. Thus, we are trying to apply a superconducting detector for the spectroscopy of the recoil proton. We apply superconducting tunnel junction[2)] (STJ) for proton spectroscopy. Generally, STJs are working at 300 - 400 mK, and have an energy resolution of less than a hundred eV. These STJs are working without a dead layer so that the recoil proton deposits full kinetic energy on the detector. For this purpose, we made STJ array with a large area (500 μm $\times$ 500 μm) at RIKEN in order to cover a large detection area. Eight STJs from 3 $\times$ 3 array provide reasonable uniformity.

We installed an apparatus for the neutron beta decay measurement with STJs at LCE (T1-4-1A). Note that we have already succeeded in measuring the neutron beta decay with conventional detectors consist of CEM and PMTs with plastic scintillators for the recoil proton and electron detection, respectively[3)]. The new apparatus is analogous with the conventional one, though it consists of STJs in the cryostat instead of CEM and a PMT. For the STJ experiment, a cryogen-free refrigerator was introduced to realize a long measurement time. The refrigerator was working about 20 hours continuously.

The pulseheight spectra of a STJ are shown in Fig.1. Because of a large background caused by neutrons, the beta decay event could not be identified. The resolution of STJ was worse due to electrical noise. By reducing the background rate and electrical noise, we will establish an experimental environment for low-energy proton detection.

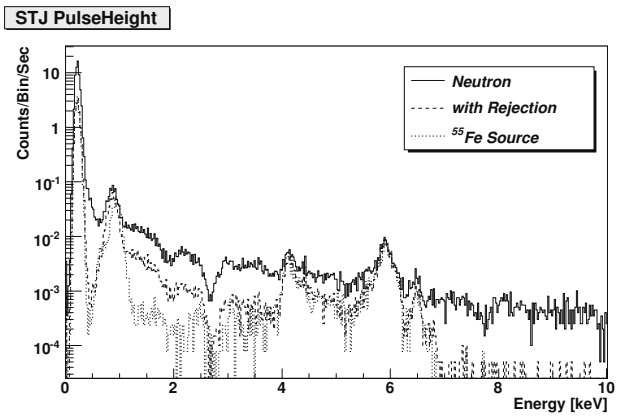

Figure 1: The pulseheight spectrum of a STJ. The solid and dashed lines are the spectrum of neutron beam and that without coincidense event. The dotted line is the spectrum by a checking source of ^{55}Fe.

References

1) H. Abele, Nucl. Instr. and Meth. A, 106, 499(2000).
2) H. Sato, et al., Jpn. J. Appl. Phys., 39, 5090(2000).
3) K. Mishima, et al., Physica B, 385-386 1219(2006).

This is a blank page

2.8 Instrumentation and Methods

Extreme Conditions, Beam Handling, Detectors and Data Treatments

This is a blank page

2.8.1

Development of High Performance Neutron Supermirrors with Ion Beam Sputtering Technique

R. Maruyama, D. Yamazaki, T. Ebisawa, M. Hino[1] and K. Soyama

J-PARC Center, Tokai, Ibaraki 319-1195

[1]*Research Reactor Institute, Kyoto University, Kumatori, Osaka 590-0494*

Neutron scattering is a useful source of information about the positions, motions, and magnetic properties of condensed matter. Neutron scattering is important because it provides valuable information that can not be obtained using other techniques such as X-ray scattering. In order to study a wide range of problems in material and life science with a much higher neutron intensity, a new spallation neutron source (Japan Proton Accelerator Research Complex, J-PARC) is now under construction. The development of neutron supermirrors with high reflectivity and large m, the ratio of the critical angle of the supermirror to that of natural nickel, is important for the J-PARC project since it greatly increases the available neutron intensity. For example, a m-supermirror guide would bring about a gain factor of m^2 in the neutron flux at the end of the guide when it is used instead of the Ni guide. Neutron supermirrors consist of alternating layers of two materials with different refractive indices for neutrons.

We have developed neutron supermirrors by employing the ion beam sputtering (IBS) technique because it enables the production of layers with a high density and small grain size. We have also demonstrated the efficiency of the ion beam polishing technique combined with the IBS deposition to suppress the interface roughness, which is an important problem in the fabrication of supermirrors with large m[1,2]. Although the IBS technique produces high quality layers, its disadvantage is that the deposition area and rate are relatively small. Based on the results of our development, a new IBS system with a large deposition area of 0.2 m^2 (diameter of 500 mm) has been designed and installed in JAEA. The difference in the deposition rate over the entire deposition area has been confirmed to be less than 4% [3].

Ni/Ti supermirrors with $m = 3$ and 4, for use as neutron guides in the J-PARC project, have been fabricated using the IBS system. The total number of layers is 403 and 1201, respectively. The neutron reflectivities of mirrors with $m = 3$ and 4 at their critical angles are 82 and 66%, respectively. Ni/Ti supermirror with $m = 6.7$, which is a record breaking critical angle, has also been fabricated. The total number of the layers is 8000. The neutron reflectivity at the critical angle is 23% [4]. Thus, we can contribute to the J-PARC project in which the production of neutron guides, benders and other devices using supermirrors is planned.

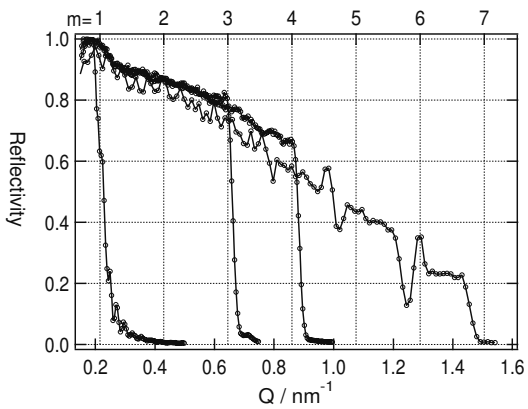

Figure 1: Reflectivity profiles of Ni/Ti supermirrors with $m = 3$, 4, and 6.7.

References

1) K. Soyama, W. Ishikawa and K. Murakami, J. Phys. Chem. Solids, 60, 1587(1999).
2) K. Soyama, H. Tsunoda and K. Murakami, Nucl. Instrum. Methods Phys. Res. A, 529, 73(2004).
3) R. Maruyama, D. Yamazaki, T. Ebisawa, M. Hino and K. Soyama, Physica B, 385-386, 1256(2006).
4) R. Maruyama, D. Yamazaki, T. Ebisawa, M. Hino and K. Soyama, Thin Solid Films, 515, 5704(2007).

2.8.2
Feasibility Tests on the Pressure-transmitting Media for Single-crystal Magnetic Neutron Diffraction Experiments

T. Osakabe

Quantum Beam Science Directorate, JAEA, Tokai, Ibaraki 319-1195

Pressure transmitting-mediums have extremely important roles in single-crystal diffraction experiments. Low hydrostaticity of the mediums under pressure highly depraves the crystallinity of the sample. As a result, the diffraction intensity lowers further. In order to investigate the hydrostaticity of the mediums, we measured the mosaic spread of NaCl single-crystal under pressure at room temperature. The investigated mediums are graphite powder, a (1:1) mixture of Fluorinert FC77 and FC70 (Sumitomo 3M, Inc.), Fomblin oil (Y140/13, Solvay Solexis Inc.), Si oil (KF96-50CS, Shin-Etsu Chemical Co., Ltd.), Daphne7373 oil (Idemitsu Co., Ltd.) [1] and glycerin. The measurements were performed using TAS-1 spectrometer. The pressure was applied by using an anvil-type high-pressure device and monitored by a standard ruby-fluorescence method.

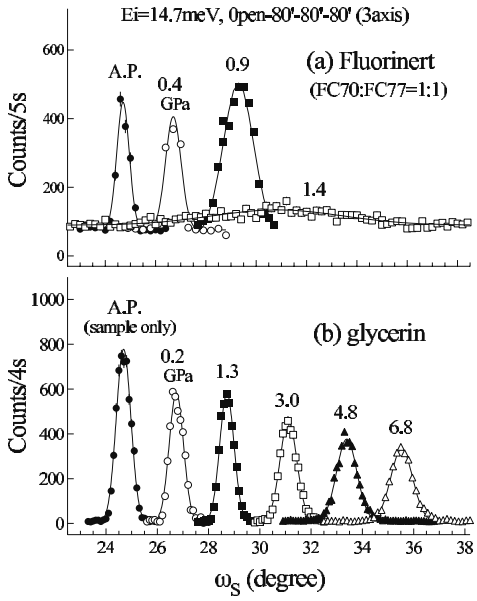

Figure 1: Rocking curves of the (200) reflections of the NaCl crystal at the selected pressures for the mediums of (a) Fluorinert and (b) glycerin.

Fig. 1(a) and (b) show the rocking curves of the (200) Bragg reflections of the NaCl single-crystal under pressure with the mediums of Fluorinert mixture and glycerin. In Fluorinert mixture, the clear peaks are observed at ambient pressure, 0.4 GPa and 0.9 GPa. At 1.4 GPa, the peak suddenly extends over more than 10 degree and the peak intensity goes down further. This indicates that Fluorinert mixture solidifies at around 1 GPa. On the other hand, in glycerin, the width of the diffraction peak increases very gently with increasing pressure and is only 1.1 times at 3 GPa and 1.5 times even at about 7 GPa. This shows that the glycerin medium transmits nearly hydrostatic pressure at least up to 7 GPa. Fig. 2 summarizes the experimental results on the hydrostaticity of the mediums. Upper limitations of the available pressures of the mediums in the diffraction experiments are also summarized in the figure.

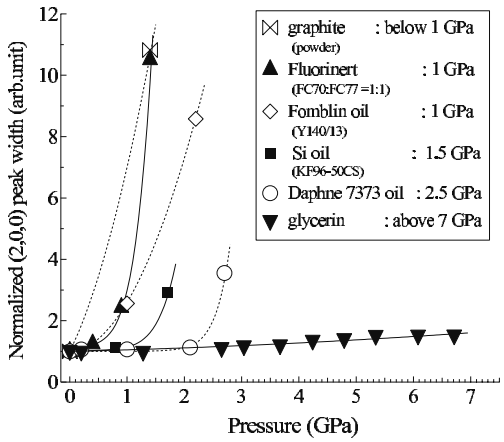

Figure 2: Pressure dependence of the (200) peak width of NaCl crystal. Each value of the width is normalized by that at ambient pressure.

References

1) K. Murata, et al., Rev. Sci. Instrum., 68, 2490(1997).

2.8.3

Performance Test of Neutron Detector for Engineering Diffractometer in J-PARC

K. Sakasai, T. Nakamura, M. Katagiri, A. Birumachi, T. Hosoya, K. Soyama, S. Satoh[1], E. Shooneveld[2] and N. Rhodes[2]

J-PARC Center, Tokai, Ibaraki 319-1195
[1]*Institute of Materials Structure Science, KEK,Tsukuba, Ibaraki 305-0801*
[2]*ISIS Science Diffraction and Muon Division, RAL, Didcot, OX11 0QX, UK*

A prototype linear scintillation neutron detector originally developed in RAL was fabricated for the engineering diffractometer in J-PARC. In this paper, some results of the performance test of the detector are described.

The fabricated detector was designed to have a small detection pixel with a spatial resolution of 3 mm. The detector had 120 pixels to establish a large neutron sensitive area. Scattered neutrons were detected based on the nuclear reaction of ^{6}Li(n,α) in ZnS/LiF scintillators in the pixel. Incident neutron position was determined by a $_2C_n$ coding method. The applied voltages of PMTs are individually set to have a gain of 3×10^7. The PG monochromator was used for the experiments. A collimated neutron beam was irradiated to the detector for the measurement of a spatial response. Neutron count linearity was also measured by changing the neutron intensity with a disperser.

Fig.1 shows the results of the measurement of the spatial response. The beam size of an incident neutron was 2×1 mm^2. Since a scintillator in a detector pixel was optically isolated from the other pixels, the spatial resolution is the pixel width of 3 mm, in principle. One can recognize that an intense signal was generated from only one pixel. It can be confirmed that the detector had a spatial resolution of about 3 mm and that there was no coding misses and no remarkable crosstalk between the pixels.

Fig.2 shows the results of the linearity measurement. Neutron counts were calibrated with a ^{3}He gas neutron detector. As can be seen in the figure, neutron counts of both the fabricated detector and the ^{3}He detector were almost the same up to 3×10^3 cps.

In summary, the fundamental performance of spatial resolution and the neutron count linearity of the fabricated detector were confirmed. Other performance such as neutron detection efficiency and uniformity are under investigation.

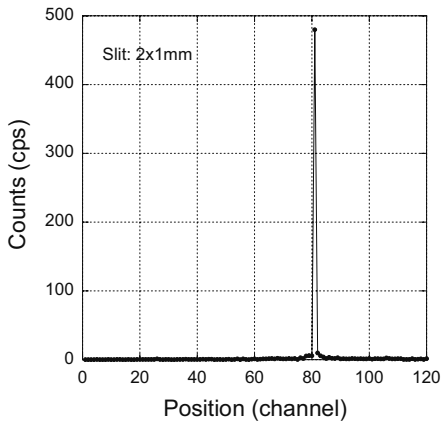

Figure 1: Results of spatial response.

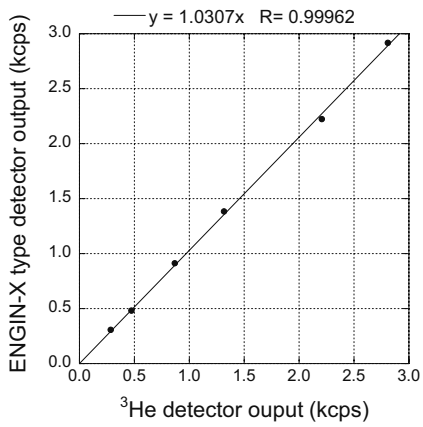

Figure 2: Linearity of neutron counts.

2.8.4
Measurement of Energy Spectrum of Neutron Beam at MUSASI Port

K. Sakasai, N. Metoki[1] and H. Matsue[2]

J-PARC Center, Tokai, Ibaraki 319-1195
[1]*Advanced Science Research Center, JAEA, Tokai, Ibaraki 319-1195*
[2]*Quantum Beam Science Directorate, JAEA, Tokai, Ibaraki 319-1195*

The high-angle MUSASI beam port provides a neutron beam with a scattering angle of 82 degrees. When PG is used as a monochromator, however, neutrons with higher harmonic ones will be generated because of the intrinsic characteristics of PG. To provide neutron energy information to users who adopt PG as a monochromator, neutron energy spectrum was measured by a TOF method.

The experimental setup is schematically shown in Fig. 1. An neutron beam was chopped by a chopper and the chopped neutrons were detected by a ^{3}He detector with a flight path of 1.27 m. Logical pulses generated by a discriminator were measured by a multi-channel scalar with a dwell time of 2 μs.

The measured neutron spectrum is shown in Fig. 2. The TOF time was converted to neutron wavelength according to the relationship between TOF time and the flight path. One can observe four peaks corresponding to neutron wavelengths of 4.48 Å, 2.24 Å, 1.49 Å and 1.12 Å, respectively. No noticeable peaks was observed above 5 Å. Table 1 lists the peak ratios calculated by fitting each peak with a Gaussian function. The most intense component was 2.24 Å-neutrons that made up 53 % of the total beam. Note that the data were not corrected by the neutron detection efficiency of the ^{3}He counter.

Table 1: The intensity ratios of detected peaks

λ(Å)	1.12	1.49	2.24	4.48
ratios	0.028	0.190	0.534	0.248

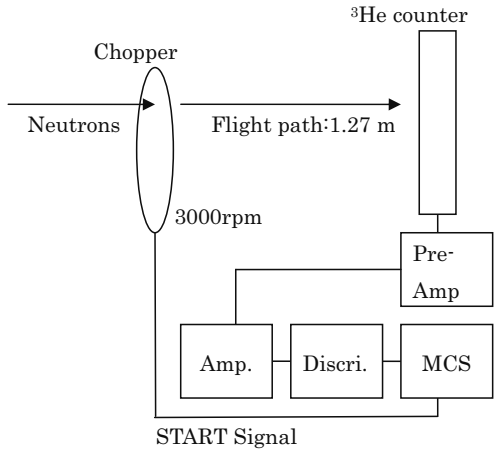

Figure 1: Experimental setup.

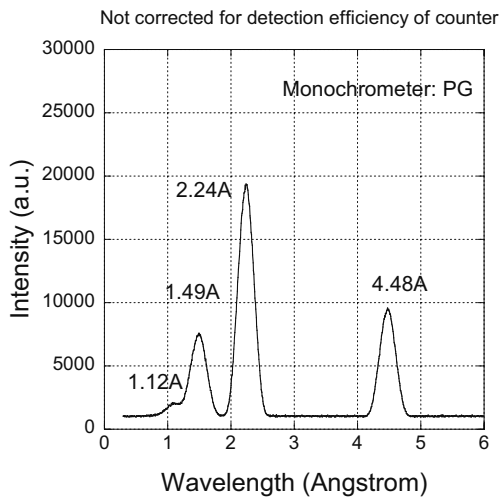

Figure 2: Neutron energy spectrum.

2.8.5

Development of High Quality Neutron Mirrors with Upgrading Cold Neutron Bender System

I. Tamura, D. Yamazaki[1], R. Maruyama[1], K. Yamamoto, K. Nakamura and K. Soyama[1]

Department of Research Reactor and Tandem Accelerator Nuclear Science Research Institute, JAEA, Tokai, Ibaraki 319-1195

[1]*Quantum Beam Science Directorate, JAEA, Tokai, Ibaraki 319-1195*

A cold neutron bender system has been installed in the JRR-3 beam hall to increase the number of beam ports. In 2006, the neutron beam transportation ability of the system was upgraded by using high quality neutron mirrors. These mirrors have high quality Ni/Ti multilayers with m = 3 on both side of silicon substrate and Boron float glass substrate. The ion beam sputtering (IBS) technique enables the production of layers with a high quality and density. A large silicon substrate, which is 40 mm in width, 105 mm in length and 0.2 mm in thickness, was selected in order to improve the installation accuracy. Neutron mirrors on silicon substrates were installed as curved neutron guides. Neutron mirrors on glass substrates were installed as straight neutron guides in the cold neutron bender system. In this report, we report the neutron reflectivity of mirrors with silicon substrates and with glass substrates using the cold neutron bender system.

The measurements of neutron reflectivity of a newly producted neutron mirror were carried out at SUIREN in the JRR-3 beam hall. The incident neutron wavelength is 3.83A.

Neutron reflectivity of a Ni/Ti supermirror on both sides of silicon substrate are shown in Fig.1 and Fig.2, respectively. Figure 1 shows the neutron reflectivity of a Ni/Ti supermirror on one side of the silicon substrate and Fig.2 shows the neutron reflectivity on the back side of it. The reflectivities at the effective critical momentum transfer were 0.9 and 0.9 respectively. It was found that the features of the reflectivities of mirrors on one side of substrate are almost the same as that of the other side. It was also found that the reflectivity at the effective critical momentum transfer of the glass substrate was 0.8.

We succeeded in manufacturing of a high reflectivity (90%) Ni/Ti supermirror with m = 3 on the silicon substrate.

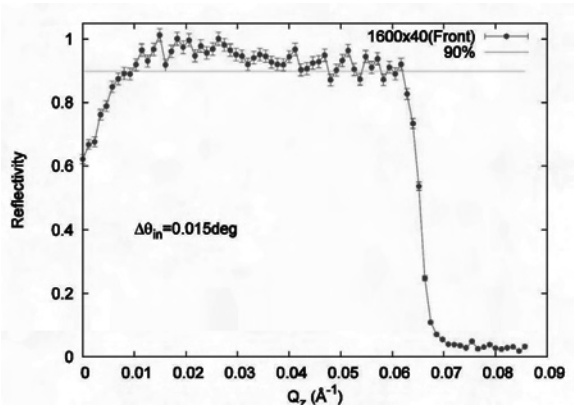

Figure 1: Neutron reflectivity on the front side of a Ni/Ti multilayer supermirror carried out at SUIREN.

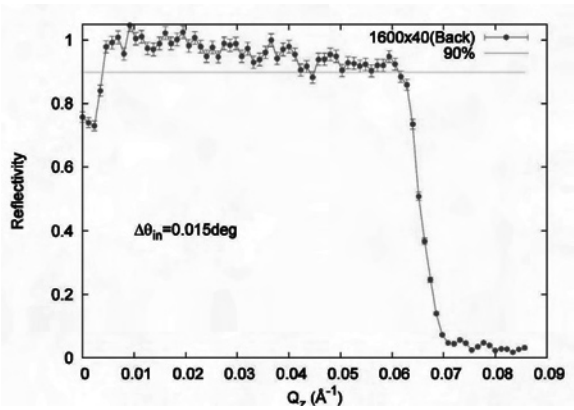

Figure 2: Neutron reflectivity on the back side of a Ni/Ti multilayer supermirror carried out at SUIREN.

References

1) D. Yamazaki, et al., JAEA-Technology, 2007-030, (2007).

2.8.6

Upgrading Cold Neutron Bender System

I. Tamura, R. Maruyama[1], K. Yamamoto, K. Nakamura, K. Aizawa[1] and K. Soyama[1]

Department of Research Reactor and Tandem Accelerator Nuclear Science Research Institute, JAEA, Tokai, Ibaraki 319-1195

[1]*Quantum Beam Science Directorate, JAEA, Tokai, Ibaraki 319-1195*

In order to effectively utilize neutron beam, we plan to increase the numbers of cold neutron beam ports that are able to install neutron beam instruments. A cold neutron bender system has been installed in the JRR-3 beam hall. The cold neutron bender system divides a cold neutron beam line into three beam lines. One is a straight beam line called C2-3-1, and the other two beam lines, C2-3-2 and C2-3-3, are bend from the straight beam line. C2-3-2 beam line bend 10 degree from the straight beam line and C2-3-3 beam line bend 20 degree from the straight.

However, the intensity of neutron beams at the ends of divided neutron guides was much lower than calculated one. Therefore, the neutron beam transportation ability of the cold neutron bender system have been upgraded using newly developed neutron mirrors .

In this paper, we report the measured spectrum at the end of C2-3-3 beam line using a chopper spectrometer because Ni monolayer mirrors were replaced with Ni/Ti multilayer supermirrors of the straight neutron guide section in the bender system.

Neutron spectrum was measured at the end of the C2-3-3 beam line by the time-of-flight method. The neutron chopper has a slit of 10 mm, a disk diameter of 1400 mm and rotation speed of 5000 rev/min. The flight path length between the end of C2-3-3 beam line and the chopper was 1.7 m, and the length between the chopper and detector was 1.3 m.

The conversion factor from the time channel to the wavelength was calibrated on a dip formed by a monochromator in the spectrum.

Figure 1 shows the neutron spectrum measured by the chopper spectrometer. The characteristic wavelength of the C2-3-3 beam line is 5.4 A for improvement.

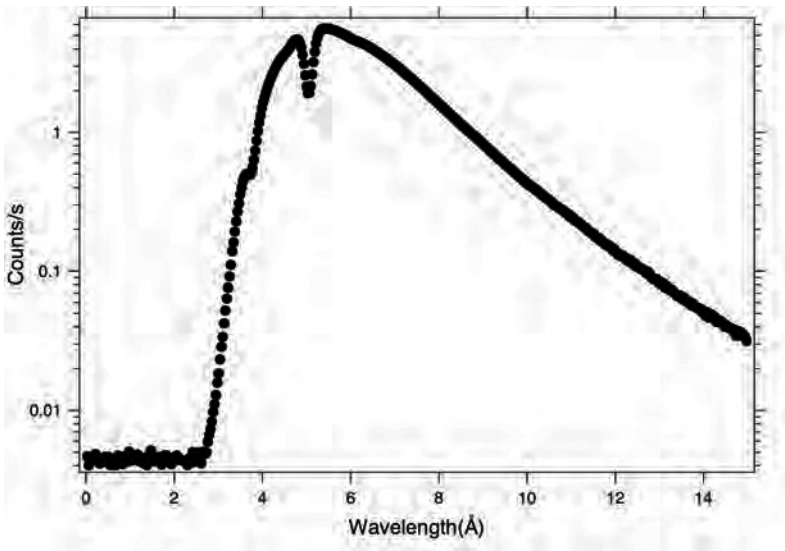

Figure 1: Neutron spectrum measured at C2-3-3 beam line by the time-of-flight method.

2.8.7

Attempt of Residual Stress Measurements in Multi-Purpose Thermal Neutron Application and Science (MUSASI)

S. Machiya[1], A. Moriai[1], H. Suzuki[1], N. Metoki[2], Y. Akiniwa[3] and Y. Morii[1]

[1] *Quantum Beam Science Directorate, JAEA, 2-4 Shirakata-Shirane Tokai, Naka, Ibaraki 319-1115*
[2] *Advanced Science Research Center, JAEA, 2-4 Shirakata-Shirane Tokai, Naka, Ibaraki 319-1115*
[3] *Department of Mechanical Science and Engineering, Nagoya University, Furo-cho, Chikusa-ku, Nagoya 464-8601*

Recently in Japan, the residual stress measurement and strain measurement for industrial use have been increasing. We feel a growing need for a secondary residual stress analysis port other than RESA. Therefore, the residual stress measurement that using MUSASI was examined.

The standard specimen was a shrink-fitted ring and pulg made of aluminum alloy A7075. The already-known residual stress can be introduced into the specimen by a shrink-fitted ring and plug method, and it has used for round-robin tests of VAMAS. The monochromator was using the bending silicon crystal, and the wavelength was 0.2203 nm.

It is possible to measure the three directions of strain using neutron diffraction. In the cartesian coordinate system, the relation between the lattice spacing d and the strain ε is as follows.

$$\varepsilon_{(h,k,l)x,y,z} = \frac{d_{(h,k,l)x,y,z} - d_{0(h,k,l)}}{d_{0(h,k,l)}}$$

Where d_0 is lattice spacing for the stress free state, and hkl is Miller's indices for stress measurement.

Next, the strain and stress in the cartesian coordinate system can be expressed as follows.

$$\sigma_x = \frac{E}{(1+\nu)(1-\nu)}\left[(1-\nu)\varepsilon_x + \nu(\varepsilon_y + \varepsilon_z)\right]$$
$$\sigma_y = \frac{E}{(1+\nu)(1-\nu)}\left[(1-\nu)\varepsilon_y + \nu(\varepsilon_x + \varepsilon_z)\right]$$
$$\sigma_z = \frac{E}{(1+\nu)(1-\nu)}\left[(1-\nu)\varepsilon_z + \nu(\varepsilon_x + \varepsilon_y)\right]$$

Figures 1 and 2 show the results of the measured residual stress. The solid line in the figure indicates the theoretical value. The measurement stress and the theoretical value are corresponding, however it opens to dispute about the resolution. In the future, improvements of the beam intensity are scheduled, and MUSASI high angle port is scheduled to operate as RESA-II.

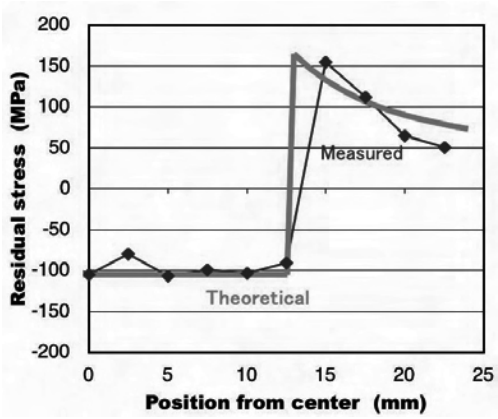

Figure 1: Hoop stress of specimen.

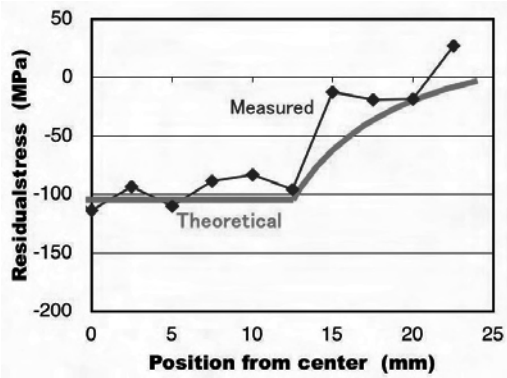

Figure 2: Radial stress of specimen.

2.8.8

Performance Test of Radial Collimator Basic Performance Test

S. Harjo, S. Torii, A. Moriai[1] and K. Shirakihara[2]

J-PARC Center, Tokai, Ibaraki 319-1195

[1]*Quantum Beam Science Directorate, JAEA, Tokai, Ibaraki 319-1195*

[2]*Department of Mechanical Engineering, Suzuka National College of Technology*

An engineering materials diffractometer TAKUMI with time-of-flight method is recently proposed to build in Japan high intensity proton accelerator project (J-PARC). TAKUMI needs radial collimators located between the sample position and detectors, to define gauge sizes precisely and to control divergences of the scattered neutrons, i.e., to limit scattered neutrons from parts except the gauge size. Since TAKUMI has a large detector solid angle surrounding the sample position, radial collimators that enable all of detector elements with different positions to observe the same gauge size are needed. However, there was not a clear description showing a relation between gauge size and collimator design parameters. Therefore, we firstly derive both relational expressions, and then to produce a prototype radial collimator to confirm the expression. Here, we report the derivation process of the relational expression and a performance evaluation test result of the prototype collimator.

The basic design concept of a radial collimator is shown in Fig.1[1)]. Here, we ignore the thickness of the blade for simplification and think a collimator with just twin blade. In general, the radial collimator design parameters are: sample-collimator path length l_1, collimator blade length l_2, sample-detector path length L_2, collimator blade intervals at the entrance s_1 and the exit s_2, and angular aperture of blade α. Here, we adopted other parameters to explain the effective widths of gauge W_g and detector W_d, geometrical maximum widths of gauge W_{gmax} and detector W_{dmax}. In our radial collimator design, the following conditions were applied for the definitions of W_g and W_{gmax}. (1) The scattered neutron from the sample shows a normal distribution

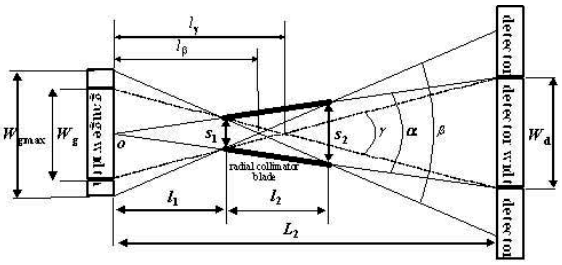

Figure 1: Definitions of radial collimator parameters

curve, and W_g is FWHM when W_{gmax} is assumed to have 95 % confidence interval of $\pm$ 2 σ, and (2) α is assumed to be a solid angle of the detector width seen from the sample center. First of all, equation (1) consists of W_{gmax}.

$$W_{gmax} = \frac{(l_1 + l_2)s_1 + l_1 s_2}{l_2} \tag{1}$$

By using a constant R, s_1 and s_2 are expressed as equations (2) .

$$R = \frac{W_d}{L_2} = \frac{s_1}{l_1} = \frac{s_2}{l_1 + l_2}$$
$$\therefore \begin{cases} s_1 &= Rl_1 \\ s_2 &= R(l_1 + l_2) \end{cases} \tag{2}$$

By substituting s_1 and s_2 in equation (1) with equations (2) l_1 is obtained as follows.

$$W_{gmax} = \frac{(l_1 + l_2)Rl_1 + l_1 R(l_1 + l_2)}{l_2}$$
$$\therefore l_1^2 + l_1 l_2 - \frac{W_{gmax} l_2}{2R} = 0$$
$$\therefore l_1 = \frac{\sqrt{l_2^2 + \frac{2}{R} W_{gmax} l_2} - l_2}{2} \quad (\because l_1 > 0) \tag{3}$$

Next, the following expressions comprise be-

cause W_{gmax} has 95 % confidence interval of the normal distribution, the FWHM value becomes W_g.

$$\mathrm{FWHM} = W_g = 2\sigma\sqrt{2\ln 2} = \frac{W_{gmax}}{2}\sqrt{2\ln 2}$$
$$\therefore W_{gmax} = \frac{2}{\sqrt{2\ln 2}} W_g \quad (4)$$

When W_g, W_d, L_2 and l_2 are set to be 1 mm, 3 mm, 2 m and 350 mm, respectively, the calculated l_1, s_1 and s_2 are 303.331 mm, 0.455 mm and 0.98 mm, respectively.

A prototype of radial collimator with the parameters shown above was made to have a total angular coverage of about 5° considering the cost balance. Mylar films coated by the gadolinium oxides (total thickness is 50μm) are used for the blades. The performance tests of this radial collimator were carried out at RESA of JRR-3. In this measurement, the sample position of RESA was matched to a focal point of the radial collimator, and the scattered neutron intensities from the sample moving along the incident beam (x) direction were observed. The used sample was a nylon fiber of 1 mm in diameter, and the displacements with a range of $x = \pm$ 2 mm from the focal point were given. An incident beam slit with enough size was chosen not to give any influences during sample movements.

Figure 2 shows the experimental result, average scattered intensities of the sample are plotted as the function of the displacement along x direction. The focal point position is around zero. The dotted line shows the result of the McStas simulation using the same collimator parameters. In this simulation, since statistics of the scattered neutrons were too low, the neutron source with the width equivalent to the sample size of nylon was placed at the sample position, and again was moved along the x direction. Similarly, the simulated curve is a plot of the average intensity versus the displacement. It can be seen that the plotted data indicates a normal distribution function of the intensity and displacement. The FWHM of the experimental data fitted by the Gauss function is 1.04 (1) mm, while that of the simulated one is 1.070 (9) mm. These values are very close to the design value of FWHM = 1 mm. Therefore, it can be concluded that the validity of the derived relational expressions and the performance of the prototype collimator have high reliabilities. The peak position of the experimental data shifts from the focal point by 0.1 mm. It may be due to the miss-alignment of the collimator or the sample. Since we positioned the collimator and the sample using a theodolite, such an alignment error might have appeared.

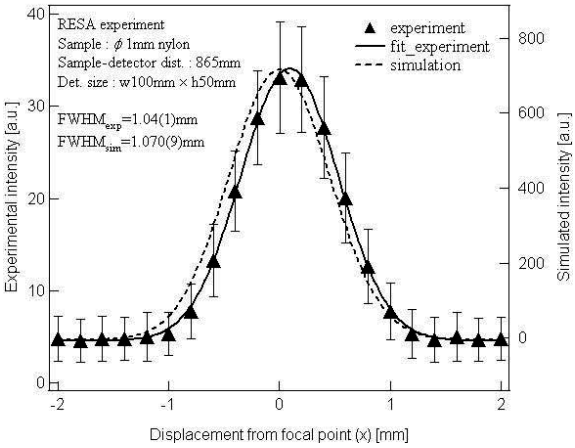

Figure 2: Intensity distribution of incoherent scattering from nylon with 1.0 mm diameter as a function of displacement along the incident beam direction. The solid line is a fitting line by Gauss function. The calculation result by McStas is shown in the dotted line.

Transmission experiments were performed by measuring the peak intensities of (110) reflection of iron wire with ϕ 1 mm for the cases with and without radial collimator prototype. The ratio of intensitiy with and without radial collimator, for (110) reflection of iron wire was 65.6 %. It seems that this value is mostly due to the normal distribution of beam that goes through the radial collimator.

References

1) S. Torii and A. Moriai, Physica B: Condensed Matter, 385-386, 1287(2006).

2.8.9

Performance Test of Radial Collimator Application Test on PSZ Material

K. Shirakihara, S. Harjo[1] and A. Moriai[2]

Department of Mechanical Engineering, Suzuka National College of Technology
[1] *J-PARC Center, JAEA, Tokai, Ibaraki 319-1195*
[2] *Quantum Beam Science Directorate, JAEA, Tokai, Ibaraki 319-1195*

A relational expression between the design parameters of radial collimators and the defined gauge sizes, which are needed to develop radial collimators, has been established, and from the basic performances tests using a radial collimator prototype at RESA, the reliability of the expression were confirmed[1)]. Now, this radial collimator prototype was tried to use on the real applications. As an example of the application, mapping measurement on poled/unpoled PZT ($Pb(Ti,Zr)O_3$) was performed at RESA. PZT is a conventional piezoelectric ceramic containing a large amount of Pb. Developments of new Pb-free materials having piezoelectric (domain switching) properties as excellent as PZT are necessary from the environmental issues. Here, establishing materials design including piezoelectric properties will help to design microstructures of materials in a short time and will lead to the production of new materials with high troughput and multi functions. The domain switching properties of PZT are usually measured by means of X-ray diffraction (XRD) which measures only the near surface and needs a polished surface. On the contrary, we can measure the domain switching properties as a whole sample or in a defined gauge volume, by means of neutron diffraction (ND).

A tetragonal PZT (sintered at 1503 K) was used as samples. The lattice constants a and c are 0.40401 nm and 0.41087 nm, respectively, and the spontaneous polarization direction is [100]. Block specimens with 4 mm width were cut from the sintered sample and polarization treatments on the width direction with 1.9 kV/mm at 373 K were conducted for 10 min. The poled and the unpoled specimens were serialised (layered) as shown in Fig.1. The specimens were set on the sample table in such a way that the scattering vector is parallel to the polarization (width) direction. The incident beam slit with 1 mm width and the radial collimator prototype for 1 mm width were used in the neutron diffraction experiment. The neutron diffraction scanning measurements were performed with 1 mm steps.

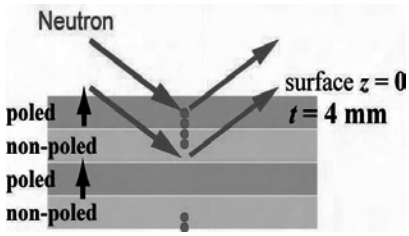

Figure 1: Specimen arrangement for ND measurement.

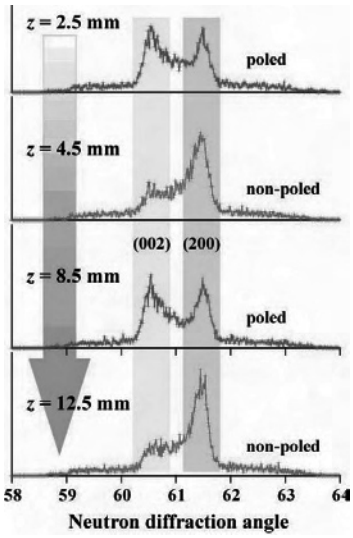

Figure 2: Typical (002) and (200) diffraction patterns of poled/unpoled PZT layered specimen shown in Fig.1.

Typical (002) and (200) diffraction patterns

measured at depths of 2.5, 4.5, 8.5 and 12.5 mm are shown in Fig.2, in which the profiles were obtained from poled, unpoled, poled and unpoled specimen, respectively. The peak intensities of (002) reflection in the poled specimens are larger than those in the unpoled specimens, showing that the spontaneous polarization direction is parallel to the [002] direction. Therefore, the domain switching properties can be estimated from the difference between the diffraction profile of a poled specimen and that of an unpoled one. The (002) and (200) diffraction intensity distribution with respect to scattering angle and penetration depth is plotted in Fig.3. The lowest intensity (zero) is shown by black (dark) color, and the color becomes brighter with increasing the intensity. As shown, the first two layers are profiles from the poled specimen, the next four layers are those from the unpoled one followed by four layers from the poled one, and the last three layers are those from the unpoled one. The profiles were fitted by a convolution of Gauss and Lorenzt functions and integrated peak intensities of both reflections were evaluated. Domain switching properties can be estimated from the integrated peak intensity ratio between (002) and (200) reflections, i.e., I_{002}/I_{200}. Figure 4 shows the I_{002}/I_{200} value in a function of penetration depth. The I_{002}/I_{200} values are higher than 1 for the poled specimen, and approximately 0.5 for the unpoled specimen. The I_{002}/I_{200} value of the unpoled specimen is in a good agreement with the theoretical I_{002}/I_{200} value, demonstrating that the neutron diffraction results have good reliability. The I_{002}/I_{200} values are almost constant for different penetration depths. This is due to the fact that there was no treatment applied to the specimen, and then the degree of polarization in a whole specimen is almost uniform. On the contrary, the I_{002}/I_{200} values have fluctuations that may show the inhomogeneities of polarization in the specimen, induced during the polarization treatments. The results described above are difficult to measure by the means of XRD that only measure surface part. A combination of neutrons having high penetration ability and a fine radial collimator can realize this kind of measurement.

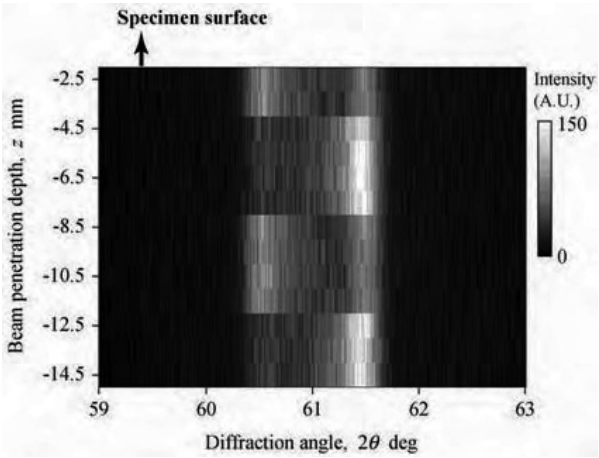

Figure 3: (002) and (200) diffraction intensity distribution with respect to scattering angle and penetration depth.

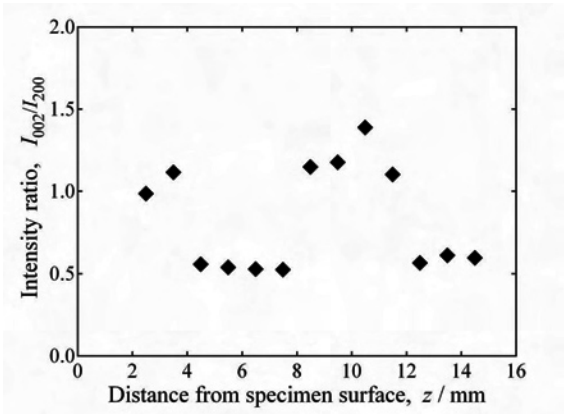

Figure 4: Integrated peak intensity ratio (I_{002}/I_{200} value) as a function of penetration depth.

References

1) S. Harjo, S. Torii, A. Moriai and K. Shirakihara, JAEA-Review (2.8.8 in this reports).

2.8.10
Test of Prototype ^{3}He PSDs and Related Electronics for New Spectrometers at J-PARC

K. Nakajima[1], T. Yokoo[1,2], S. Satoh[1,2], M. Nakamura[1], N. Kaneko[1,2], Y. Kobayashi[1,2] and R. Kajimoto[1]

[1] *J-PARC Center, Tokai, Ibaraki 319-1195*
[2] *Institute of Materials Structure Science, KEK, Tsukuba, Ibaraki 305-0801*

At MUSASI port, we have tested prototypes of detectors and related electronics, which will be employed by spectrometers for J-PARC. For neutron scattering instruments planned for the new spallation neutron source at Materials and Life science experimental Facility (MLF) at J-PARC, various novel types of ^{3}He position sensitive detectors (PSDs) are considered to be used. Since the detector is one of the most important key components, it is indispensable to evaluate the feasibility and the performance of these new detectors and related electronics prior to actual construction of the instruments.

One of the new types of the PSD is a long tube PSD for 2 chopper spectrometers, AMATERAS and 4SEASONS. The length of these detectors are $l = 3$ m and 2.5 m to minimize gaps between detectors (see Fig. 1). They will be accommodated in the scattering chamber under the high vacuum condition ($\sim 10^{-6}$ Torr) to reduce the background. Therefore, new long PSDs are equipped with newly designed vacuum couplings with SHV connectors at the ends. A number of long PSDs, which are deferent in lengths (l), diameters (ϕ), gas pressures (p), have been prepared by two different detector venders. The detectors were set on the testing stand, and we have examined them using neutron beam.

A typical result of performance tests is shown in Fig. 2. The linearity of the position sensitivity is confirmed within the error of 3 mm for all tested detectors. The resolution is less than 19 mm in FWHM. These performances are almost equivalent to those of conventional short PSDs commonly used at KENS. We have found slight differences in the performance between the detectors provided by different venders, which are, however, completely acceptable to us.

According to the present results, we have fixed the final specifications of detectors for 2 chopper spectrometers, that is, $l = 3$ m, $\phi = 1$ inch, $p = 10$ atm PSDs for AMATERAS and $l = 2.5$ m, $\phi = 3/4$ inch, $p = 20$ atm PSDs for 4SEASONS.

Figure 1: A 3 m length ^{3}He PSD on the testing stand at MUSASI.

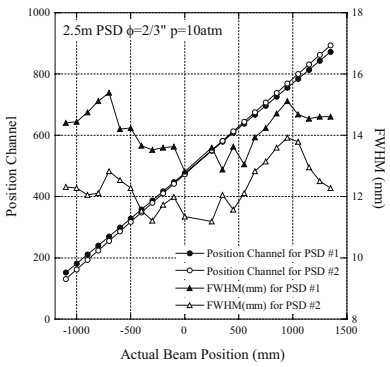

Figure 2: Position dependence of output position (position channel) and peak width of 2.5 m length, ^{3}He PSDs ($\phi = 2/3$ inch, $p = 10$ atm) provided by different vendors.

2.8.11
Development of a Neutron Polarizing Device Based on a Quadrupole Magnet and Evaluation of Its Polarizing Power

T. Oku, S. Yamada, T. Shinohara, J. Suzuki and H. M. Shimizu[1]

Quantum Beam Science Directorate, JAEA, Tokai, Ibaraki 319-1195
[1]*KEK, Tsukuba, Ibaraki 305-0801*

So far, we have developed a Halbach-type permanent quadrupole magnet (HQM) composed of a strong permanent magnet NdFeB with an effective aperture size of 3.5 mm in diameter and a length of 600 mm as a neutron polarizing device[1)]. As a result of the cold neutron beam polarization experiment, a very high neutron polarization degree of $P = 0.9993 \pm 0.0025$ was obtained[1)]. The polarizing device based on the HQM is considered to be a suitable polarizer for a focusing geometry small-angle polarized neutron scattering instrument using a magnetic neutron lens because of its high polarization efficiency and high polarized neutron transmission[2)]. However, for the practical application to the neutron scattering experiments, an HQM with a larger aperture size is demanded. Therefore, we have developed the HQM with a larger aperture of 7 mm in diameter and length of the 700 mm (Fig.1). According to the magnetic field measurement, the magnetic field gradient was obtained to be $\partial |\mathbf{B}| / \partial r = 515.8 \pm 1.4$ T/m inside the HQM aperture. Neutron-absorbing cadmium (Cd) slits with an inner diameter of 5 mm were inserted between the HQM units in every 100 mm interval along the magnet length to prevent neutrons from hitting the inner surface of the HQM. Therefore, the effective aperture of the HQM is 5 mm in diameter.

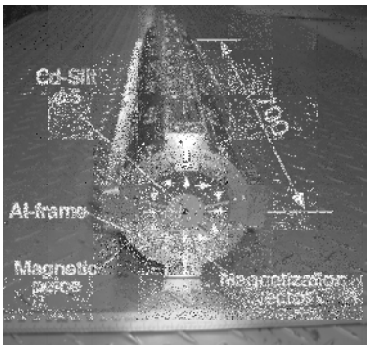

Figure 1: The Halbach-type permanent quadrupole magnet.

We have performed a cold neutron polarization experiment using the HQM at the beamline of C3-1-2-1(NOP) of JRR-3 in Japan Atomic Energy Agency. The experimental setup is shown in Fig.2. The neutron wavelength was $\lambda = 8.07$ Å. The neutrons, which passed through the HQM, were focused and defocused by the magnetic neutron lens depending on their spin polarity[3,4)], and were detected by the 2d-detector. Figures 3 (a) and (b) show the two-dimensional intensity distributions on the detector, when the spin flipper (SF) is off and on. The radial averages of the intensity distributions are shown in Fig.[4].*Thepeaksappearinginthebothcasesareproducedbythepo*
Thus, the peak height ratio $\Delta I_{\mathrm{SF\ off}}/\Delta \mathrm{I}_{\mathrm{SF\ on}}$ corresponds to the so-called flipping ratio R. Therefore, we get the relation[5)]

$$R = \frac{\Delta I_{\mathrm{SF\ off}}}{\Delta I_{\mathrm{SF\ on}}} = \frac{1 + P_i P_a (1 - D)}{1 + P_i P_a (1 - D)(1 - 2f)}, \tag{1}$$

where P_i and P_a are the polarization efficiencies of the polarizer and analyzer, respectively. In this study, the magnetic neutron lens corresponds to the analyzer. f is the flipping efficiency of the SF, D is the depolarization factor. By assuming $P_a = 1$, $f = 1$ and $D = 0$, we obtain

$$P_i = \frac{(\Delta I_{\mathrm{SF\ off}} - 1)}{(\Delta I_{\mathrm{SF\ off}} + 1)}. \tag{2}$$

Based on Eq.(2), we calculated the neutron polarization P_i of the neutrons which passed

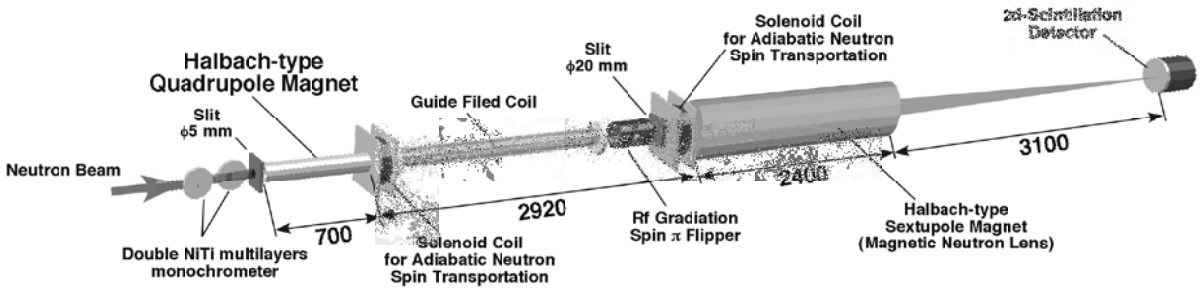

Figure 2: The experimental setup.

through the HQM, and obtained $P_i \sim 0.999$.

In conclusion, we have developed the HQM with an aperture of 7 mm in diameter and a length of 700 mm, and performed the cold neutron beam polarization experiment. As the result, we obtained the highly polarized neutron beam with a polarization degree of $P_i \sim 0.999$.

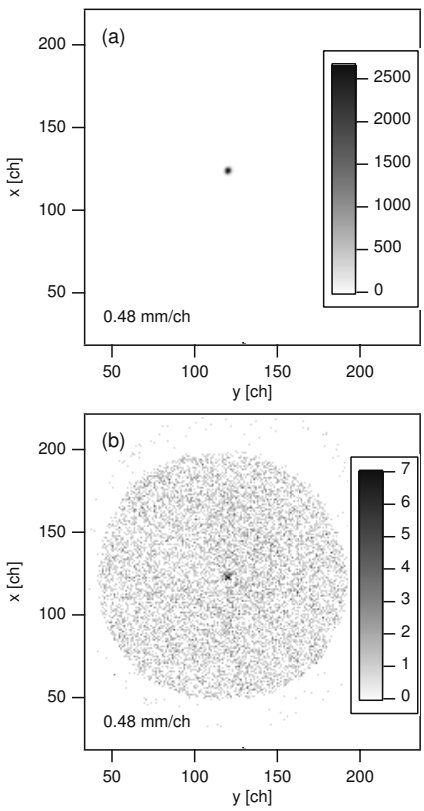

Figure 3: Two-dimensional intensity distributions. (a) SF is off, (b) SF is on.

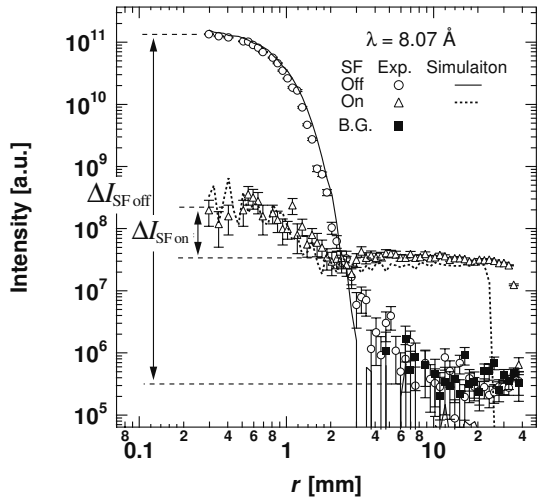

Figure 4: The radial averages of the intensity distribution, when the spin flipper is on and off.

References

1) T. Oku, et al., Physica B, 397, 188(2007).
2) T. Oku, et al., J. Appl. Cryst., 40, s408(2007).
3) H.M. Shimizu, et al., NIM-A, 430, 423(1999).
4) J. Suzuki, et al., J. Appl. Cryst., 36, 795(2003).
5) T.J. Jones and W.G. Williams., NIM, 152, 463(1978).

2.8.12

Profile of a Neutron Reflectometer SUIREN at C2-2, JRR-3

D. Yamazaki[1,2], A. Moriai[2], I. Tamura[3], R. Maruyama[1], T. Ebisawa[1], K. Soyama[1,2], M. Takeda[2] and M. Hino[4]

[1] *J-PARC Center, Tokai, Ibaraki 319-1195*
[2] *Quantum Beam Science Directorate, JAEA, Tokai, Ibaraki 319-1195*
[3] *Department of Research Reactor and Tandem Accelerator, JAEA, Tokai, Ibaraki 319-1195*
[4] *Research Reactor Institute, Kyoto University, Kumatori, Osaka 590-0494*

A new neutron reflectometer "SUIREN" has been in operation at the C2-2 port of the JRR-3 of JAEA since 2006. JAEA accepts proposals from academic and industrial researchers. JAEA hase already provided 26 days for outside researchers in 2006 and will provide about 60 days in 2007. This instrument has vertical-sample geometry and is going to be used for studies on supermirrors[1)], polymers, magnetic thin films and other materials with solid surfaces.

Specifications of the SUIREN reflectometer are collectively shown in Table 1. The intensity (* in the table) depends on the status of the LTAS instrument operating at the C2-1 port, but can be normalized by monitoring incident neutron counts. The back-ground level (4.5×10^{-3} n/s) was measured when the local beam shutter was closed and the detector window was covered with a B_4C rubber sheet.

Test measurements were performed before starting operation for users. Fig. 1 shows a specular reflectivity of a silicon wafer (3 inches in diameter) with a fit curve for a Si wafer with surface oxidization of 5 Å. It was found that reflectivity down to 10^{-6} ($Q_z \lesssim 0.22$ Å^{-1}) can be measured unless sample itself causes significant background. The measuring time was about 32 hours. The reflectivity of a Ni/Ti multilayer was also measured down to 10^{-6}($\lesssim 0.42$ Å^{-1}), and Bragg peaks up to the sixth one were identified. It took 59 hours for the measurement.

In conclusion, the neutron reflectometer SUIREN showed a high performance in test measurements and has been used by industrial and academic researchers. As for future plans, polarization analysis will be available in 2007. Fe/Ge multilayer monochromators[2)] (coated at KUR) will be installed as a polarizing filter and an analyzer. A 1 T sample magnet and a refrigerator (10 K $\sim$ RT) will also be available.

Table 1: Specifications of the SUIREN reflectometer. The intensity(*) is not fixed as described in the text.

Wavelength λ	3.8 Å
$\Delta\lambda$ / λ	1.3 %
Maximum Beam Size	$80^H \times 20^W$ mm^2
Slit1-Slit2 Distance	1450 mm
Sample-Detector Distance	1100 mm
Incident Angle Resolution	$\geq$ 0.004 deg
Scattered Angle Resolution	$\geq$ 0.015 deg
Intensity*($\Delta\theta_{in} = \pm$ 0.04 deg)	2.3×10^4 n/s/cm^2
Back Ground	4.5×10^{-3} n/s
Measurable Reflectivity	$\gtrsim 10^{-6}$

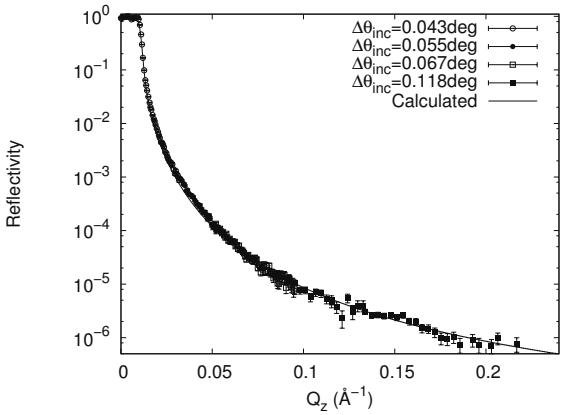

Figure 1: Measured Reflectivity from a silicon wafer.

References

1) R. Maruyama, et al., Physica B, 385-386, 1256(2006).
R. Maruyama, et al., Thin Solid Films, 515, 5704(2007).
2) M. Hino, et al., Physica B, 385-386, 1187(2006).

This is a blank page

2.9 Neutron Radiography

This is a blank page

2.9.1

Neutron Tomography Analysis of Metal Hydride Canister with/without Hydrogen Charging and Discharging Cycle

Y. Fujita, T. Ebisawa[1], H. Iikura[2] and M. Matsubayashi[2]

Muroran Research Laboratory, The Japan Steel Works, Ltd., Muroran, Hokkaido 051-8505
[1]*Machinery Research Laboratory Yokohama branch, JSW, Yokohama, Kanagawa 236-0004*
[2]*Quantum Beam Science Directorate, JAEA, Tokai, Ibaraki 319-1195*

Hydrogen is expected as an ideal clean energy medium in the future, but it is difficult to store hydrogen compactly, lightly and safely. Metal hydride (MH) is one of the practical hydrogen storage methods, which can absorb and desorb a large amount of hydrogen atoms in the interstitial sites at ordinary temperatures and low pressure. MH is commonly manufactured by vacuum induction melting, and crushed into grain for expanding the reactive area with hydrogen. The MH grain becomes a fine powder with hydrogen charge/discharge cycle, because the lattice volume change with the cycle makes many cracks on MH grains. This pulverizing phenomenon makes the apparent MH volume larger and changes the internal structure of a MH tank. Because such structural change may cause performance degradation, the authors tried to visualize the internal structure of MH tanks by neutron tomography analysis.

Two MH canisters, MH-1 and MH-2, were prepared for neutron tomography analysis. Both canisters' rated hydrogen amount was 50 NL (normal liter). The dimension was O.D. 50 mm × H 132 mm and the weight is about 700 g. Each canister contained 330 g MH grain (composition: La-Ce-Ni-Mn-Co) and six tubular glass sleeves (O.D. 2.8 mm) for improving hydrogen ventilation. MH-1 had been charged and discharged hydrogen once. On the other hand, MH-2 had undergone 1000 cycles. Both canister were discharged almost hydrogen and filled with 0.2 MPaG argon gas.

Figure 1 is the neutron tomography analysis result. The upside of Fig.1 shows the partially integrated images of the vertical cross-sections of MH-1 (left) and MH-2 (right) and the downside shows the horizontal slice images at dashed line. It is easy to distinguish the six glass sleeves in MH-1 as dark straight lines in the vertical cross-section image and dark circles in the horizontal slice image, respectively. But the sleeve shapes become unclear after 1000 cycles test. The volume expansion of MH might collapse the tubular structure of the glass sleeves. The rising of the MH filling level also proves the MH volume expansion.

The neutron tomography analysis was carried out on 1-cycle and 1000-cycle MH canisters. The analysis revealed the filled MH expands its volume by the charge/discharge cycle, and collapsed the glass sleeves by hydrogen ventilation.

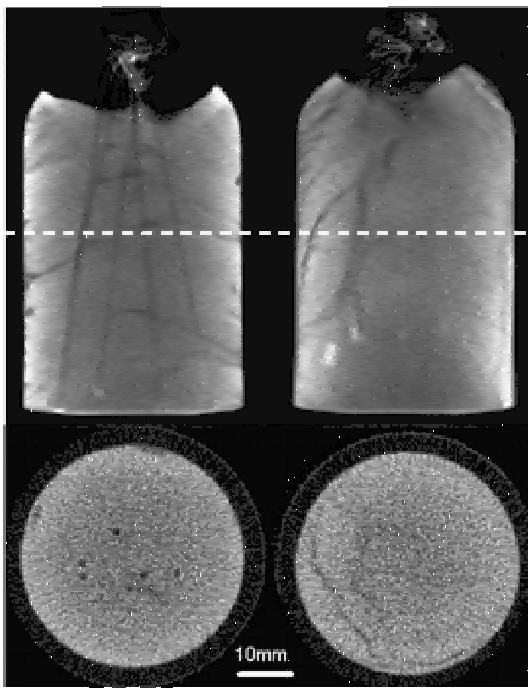

Figure 1: Neutron tomography analysis result of 1-cycle (MH-1, left) and 1000-cycle (MH-2, right) canister.

2.9.2
Development of Neutron Imaging Techniques for PEM Fuel Cells (II)

M. Matsubayashi, H. Iikura and R. Yasuda
Quantum Beam Science Directorate, JAEA, Tokai, Ibaraki 319-1195

The proton exchange membrane fuel cell (PEMFC) is a promising power source for transportation and consumer electronics because of its efficient energy conversion. The Japan Automobile Research Institute (JARI) standard type PEMFC was modified for this study such as replacements of stainless steel made fastening bolts and nuts with duralumin made ones.

Neutron images of the non-operated JARI standard type PEMFC for computed tomography (CT) were captured by a cooled CCD camera system. Projection images were obtained for three conditions: 1) dried condition, 2) anode side flow channel filled with water condition("one-side-wet") and 3) anode/cathode side flow channels filled with water condition("both-sides-wet"). Two types of reconstruction calculation were applied such as: 1) conventional FBP(filtered back projection) method, and 2) FBP method using specialized shading images as projection images for dried condition (specialized-FBP).

All figures are 2-D vertical slices reconstructed from CT images and aligned such as left: specialized-FBP, right: conventional FBP. Figures 1 and 2 show the results for "one-side-wet" condition. The left image of Fig.1 shows no water in the flow chnnel but the right image shows residual water. This is due to the insufficient dried-condition of the cell. Both images in Fig. 2 show water existence in the flow channel. As clearly understood, the quality of left image is better than that of the right one. Similar images are also obtained in Fig. 3 and 4 for "both-sides-wet". The left images clearly show water condition in both flow channels as compared to the right ones.

In this study, it was confirmed that the specialized-FBP method is superior to the convetional-FBP method and is useful for the visualization of water existence in a PEMFC.

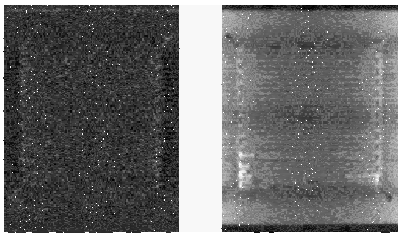

Figure 1: 2-D vertical slice reconstruction at the cathode side carbon separator under anode side flow channel filled with water condition.

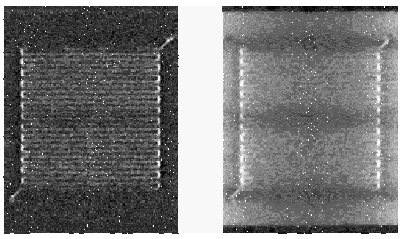

Figure 2: 2-D vertical slice reconstruction at the anode side carbon separator under anode side flow channel filled with water-condition.

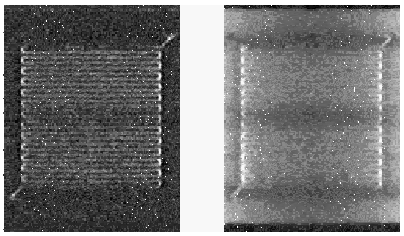

Figure 3: 2-D vertical slice reconstruction at the cathode side carbon separator under anode/cathode side flow channels filled with water condition.

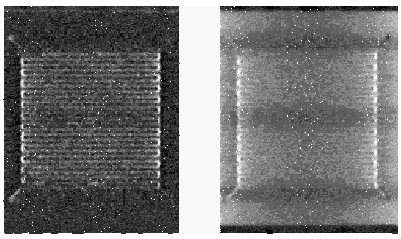

Figure 4: 2-D vertical slice reconstruction at the anode side carbon separator under anode/cathode side flow channels filled with water condition.

2.9.3

Evaluation Research for Long Term Stability of Metal

M. Matsubayashi, H. Iikura and H. Yishikawa[1]

Quantum Beam Science Directorate, JAEA, Tokai, Ibaraki 319-1195

[1]*Geological Isolation Research and Development Directorate, JAEA, Tokai, Ibaraki 319-1194*

Neutron imaging technique was applied to improve the estimation of the amount of corrosion in an iron-remainder left underground for geologic isolation research and development.

Carbon steel (SM400B, 30 × 30 × 2 mm thick) was macerated in simulated seawater under atmospheric conditions for almost 5 years, and its surface was corroded as shown in Fig.1 (left). It was used as a corroded carbon steel sample for neutron computed tomography (neutron CT). Copper plate (pure copper 30 × 30 × 2 mm thick) was macerated in H_2S-contained dilute NaS solution for 3 days, and its surface was corroded as shown in Fig.1(right). It was used as a corroded copper plate sample for neutron imaging. The neutron CT of the corroded carbon steel sample was obtained by half rotation projection images with even angle increment. A filtered back projection method was applied as the reconstruction calculation algorithm.

Fig.2 shows projection images of the corroed carbon steel sample and computed tomograms. Horizontal lines in the projection image indicate the cut position of computed tomograms. Reduction of base metal of the carbon steel plate was clearly observed in the computed tomograms. Meanwhile, significant differences were not observed for the corroded copper plate sample as shown in Fig.3 except boundary of flaking. Because the corrosion layer was very thin, then the thickness of the base metal did not change. Experimental results show the effectiveness of neutron imaging to corrosion evaluation for carbon steel but not for copper.

This study was conducted as a collaborative study between Quantum Beam Science Directorate and Geological Isolation Research and Development Directorate.

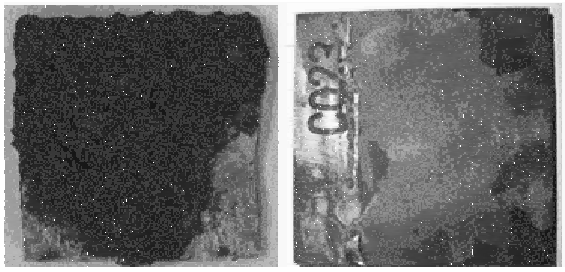

Figure 1: Sample photograph: corroded carbon steel sample (left), corroded copper plate sample (right).

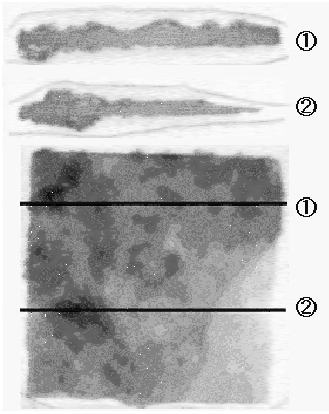

Figure 2: Projection image of corroed carbon steel sample (upper) and computed tomograms (lower) at the cutlines indicated in the projection image.

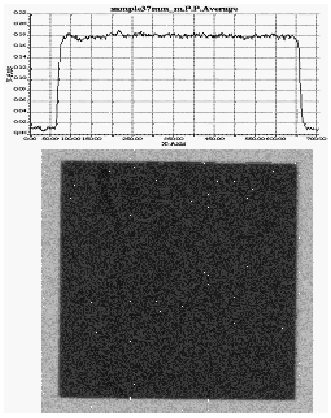

Figure 3: Projection image of corroded copper sample (upper) and vertically averaged plofile (lower).

This is a blank page

2.10 Prompt Gamma-ray Analysis

2.10.1
Determination of Cadmium in Polymer Samples by MPGA

Y. Toh, M. Oshima, M. Koizumi, A. Kimura, K. Sushida[1] and M. Sato[1]

Department of Research Reactor and Tandem Accelerator Nuclear Science and Energy Directorate, Japan Atomic Energy Agency, Ibaraki 319-1112

[1]*Inorganic Analysis Laboratory, Toray Research Center, Inc., Otsu 520-8567*

Prompt gamma ray analysis (PGA) is a high-sensitive, high-precision, multi-element and non destructive method[1)]. The method is used in various fields, such as geology, archaeology, earth science, industry and environmental science. However, the difficulty of quantification arises when the gamma-ray intensity from the trace element of interest is not strong enough in comparison with the background gamma rays from the large amount of other elements in the sample. In order to improve the sensitivity of PGA, we proposed to introduce multiple gamma ray detection method to the PGA, and constructed a neutron beam line for multiple prompt gamma ray Analysis (MPGA)[2–4)].

In summer 2000, the EU commission approved drafts of the guidelines for waste electrical and electronic equipment (WEEE) and the guidelines for the restriction of the use of certain hazardous substances in electrical and electronic equipment (RoHS). The guidelines establish that users can return waste electrical and electronic equipment to the manufacturers free of charge. This regulation applies to electrical household equipment, electrical tools, consumer electronics, IT and telecommunication equipment, lamps and lights, toys, medical equipment, monitoring and control instruments as well as slot or vending machines. Lead, mercury, cadmium, chromium (VI), polybrominated biphenyls (PBB) and polybrominated diphenyl ethers (PBDE) are prohibited. The following experimental work on the investigation of cadmium containing polymers demonstrates the efficiency of the MGPA technique as a screening method according to the RoHS guidelines. Cadmium as a toxic heavy metal shows the most intensive gamma ray signal at 558 and 651 keV. A cadmium standard sample provided by the Institute for Reference Materials and Measurements (IRMM) was measured for about 10 minutes at the JRR-3 reactor (C2-3-2). The total event rate was about 1.7 k count/sec. Figure 1 shows a typical signal profile of the gamma ray of cadmium in IRMM B6 sample on two dimensional spectrum. The IRMM B6 sample contains 54 ppm cadmium. From the experiment, we estimated the quantification limit of cadmium in a polymer sample to be about 0.1 ppm with a new MPGA detector system which consists of 8 clover Ge detectors, 4 coaxial Ge detectors and 2 twin Ge detectors. MPGA does not require any sample preparation. Therefore, MPGA may be used as a screening analysis for RoHS related samples.

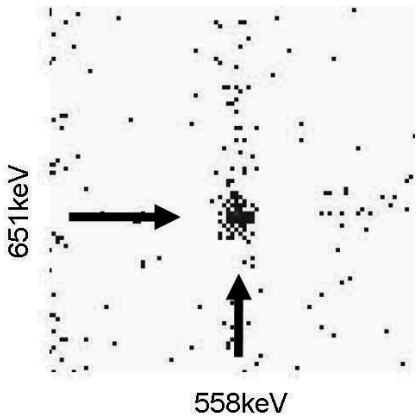

Figure 1: Cadmium gamma ray peak of IRMM B6 sample on two dimensional spectrum. Cadmium emits strong gamma ray pair of 558 and 651 keV.

References

1) B.J. Allen, et al.: "Neutron Radiative Capture", Pergamon Oxford, (1984).
2) Y.Toh, et al., Appl. Radiat. Isotopes, 64, 751(2006).
3) M.Oshima, et al., Proc. J. Radioanal. Nucl. Chem., 271, 317(2007).
4) A.Kimura, et al., AIP conf., 769, 792(2004).

This is a blank page

Appendixes

This is a blank page

Appendix A

Program Committee for Neutron Beam Utilization in the JFY 2006
of the Advisory Council for JAEA's Research Facilities

The term of office : April, 2006- March, 2007

(Chairman)	Hideki	Yoshizawa	Professor, The Institute for Solid State Physics, The University of Tokyo
(Vice-Chairman)	Mitsuru	Ebihara	Professor, Graduate School of Science, Tokyo Metropolitan University
	Toshiji	Kanaya	Professor, Institute for Chemical Research, Kyoto University
	Makoto	Hayashi	Senior Director for Neutron Promotion Planning Division, Ibaraki Prefectural Government
	Haruki	Madarame	Professor, Research Center for Nuclear Science and Technology, The University of Tokyo
	Akira	Matsumura	Professor, Graduate School of Comprehersive Human Sciences, Tsukuba University
	Kazuyoshi	Yamada	Professor, Institute for Materials Research, Tohoku University
	Kazuhisa	Kakurai	Units Manager, Quantum Beam Science Directorate, JAEA
	Ryouta	Kuroki	Units Manager, Quantum Beam Science Directorate, JAEA
	Yukio	Morii	Units Manager, Quantum Beam Science Directorate, JAEA
	Naoto	Metoki	Principal Scientist, Advanced Science Research Center, JAEA
	Kiyonobu	Yamashita	Deputy Director, Department of Research Reactor and Tandem Acceleractor, JAEA
(Secretary)	Yoshinobu	Ishii	Group Leader, Quantum Beam Science Directorate, JAEA
(Secretary)	Tsuyoshi	Kusunoki	General Manager, Research Reactor Utilization Section, Department of Research Reactor and Tandem Acceleractor, JAEA
(Secretary)	Sigeru	Mori	General Manager, Administration Section, Department of Research Reactor and Tandem Acceleractor, JAEA
(Secretary)	Fumio	Sasajima	Deputy General Manager, Research Reactor Utilization Section, Department of Research Reactor and Tandem Acceleractor, JAEA
(Secretary)	Kiyoshi	Nakamura	Chief, Assistant Principal Engineer, Research Reactor Utilization Section, Department of Research Reactor and Tandem Acceleractor, JAEA
(Secretary)	Hiroko	Koakutsu	Administration Section, Department of Research Reactor and Tandem Acceleractor, JAEA
(Observer)	Hidefumi	Takeshita	General Manager, Administration Section, Industrial Collaboration Promotion Department, JAEA
(Observer)	Yusuke	Uehara	General Manager, Facilities Utilization Promotion Section, Industrial Collaboration Promotion Department, JAEA
(Observer)	Yasuhiko	Fujii	Deputy Director General, Quantum Beam Science Directorate, JAEA
(Observer)	Teruo	Inabe	Deputy Director, Division of Collaborative Activities, Office of Planning, JAERI

Appendix B

Publication List in the Period of the JFY 2006

1. Neutron Powder Diffraction Study on the Crystal and Magnetic Structures of $BiCoO_3$.
   A.A. Belik, S. Iikubo, K. Kodama, N. Igawa, S. Shamoto, S. Niitaka, M. Azuma, Y. Shimakawa, M. Takano, F. Izumi and E. Takayama-Muromachi
   Chem. Mater. **18** (2006) pp. 798-803.

2. Two-dimensional Sodium Fluctuation at High Temperatures in a High-temperature Thermoelectric Material γ-$Na_{0.7}CoO_2$.
   S. Shamoto, Y. Hasegawa and T. Kajitani
   Jpn. J. Appl. Phys. **45**, No. 8A (2006) pp. 6395-6397.

3. Local Crystal Structures of $Ge_2Sb_2Te_5$ Revealed by the Atomic Pair Distribution Function Analysis.
   S. Shamoto, K. Kodama, S. Iikubo, T. Taguchi, N. Yamada and T. Proffen
   Jpn. J. Appl. Phys. **45**, No. 11 (2006) pp. 8789-8794.

4. Finite Size Effects of Nanoparticles on the Atomic Pair Distribution Functions.
   K. Kodama, S. Iikubo, T. Taguchi and S. Shamoto
   Acta Cryst. A **62** (2006) pp. 444-453.

5. Structural Study on Optical Recording Materials $Ge_2Sb_{2+x}Te_5$ and $GeBi_2Te_4$.
   S. Shamoto, N. Yamada, T. Matsunaga and T. Proffen
   Physica B **385-386** (2006) pp. 574-577.

6. High Intensity Chopper Spectrometer 4SEASONS at J-PARC.
   R. Kajimoto, T. Yokoo, K. Nakajima, M. Nakamura, K. Soyama, T. Ino, S. Shamoto, M. Fujita, K. Ohoyama, H. Hiraka, K. Yamada and M. Arai
   J. Neutron Research **15-1** (2007) pp. 5-12.

7. Origin of the Monoclinic-to-Monoclinic Phase Transition and Evidence for the Centrosymmetric Crystal Structure of $BiMnO_3$.
   A.A. Belik, S. Iikubo, T. Yokosawa, K. Kodama, N. Igawa, S. Shamoto, M. Azuma, M. Takano, K. Kimoto, Y. Matsui and E. Takayama-Muromachi
   J. Am. Chem. Soc. **129** (4) (2007) pp. 971-977.

8. Analysis of Boron in Wood Trested with Boric Acid Solutions Using Doppler Broadening Method of Prompt Gamma-Rays.
   S. Yamauchi, Y. Sakai, Y. Watanabe, M. K. Kubo and H. Matsue
   J. Wood Sci **52** (2006) pp. 279-281.

9. Observation of a $\pi h_{9/2} \otimes \nu i_{13/2}$ oblate band in ^{188}Tl.
X.Y. Zhou, L. Ma Y.B. Xing, Y.H. Zhang, Y.X. Guo, X.G. Lei, C.Y. Xie, M. Oshima, Y. Toh, M. Koizumi, A. Osa, Y. Hatsukawa, M. Sugawara and M.M. Ndontchueng
Eur. Phys. J. A **28** No. 3 (2006) pp. 271-275.

10. Evaluation of Reliability of Neutron Activation Analysis Using k_0-Standardization and Application to Environmental Aerosol Samples.
S. Miyata, A. Tanji, H. Imura, H. Matsue and C. Yonezawa
BUNSEKI KAGAKU **55** (2006) pp. 689-699.

11. Characterisation of Sythetic Multi-Element Standards (SMELS) Used for the k_0-NAA.
P. Vermaercke, P. Robouch, M. Egusliza, F.De. Corte, G. Kennedy, B. Smodis, R. Jacimovic, C. Yonezawa, H. Matsue, X. Lin, M. Blaauw and J. Kucera
Nucl. Instr. Meth. Phys. Res. **A564** (2006) p. 675.

12. Neutron In-Beam Mössbauer Spectroscopic Studyof Iron Disulfide at Room Temperature.
M.K. Kubo, Y. Kobayashi, H. Nonaka, Y. Yamada, Y. Sakai, H. Shoji and H. Matsue
Hyperfine Interact, **166** (2006) pp. 425-428.

13. Determination of Trace Elements Using Multi-Parameter Coincidence Spectrometry.
Y. Hatsukawa. Y. Toh, M. Oshima, A. Kimura and M. Hosein Mahmudy Gharaie
J. Radioanalyt. Nucl. Chem. **271** (2007) pp. 43-45.

14. Correction of k_0-Factors for non-1/v Elements Based on Neutron Spectrum Measurements.
H. Matsue and C. Yonezawa
J. Radioanal. Nucl. Chem. **271** (2007) pp. 425-429.

15. Mössbauer Spectroscopic Study of ^{57}Fe Species Produced by ^{56}Fe(n,γ)^{57}Fe Reaction in Iron Disulfide.
Y. Kobayashi, Y. Tsuruoka, M. K. Kubo, H. Nonaka, Y. Yamada, Y. Sakai, H. Shoji, W. Sato, A. Shinohara, Y. Watanabe and H. Matsue
J. Radioanal. Nucl. Chem. **272** (2007) pp. 623-626.

16. High Sensitive Elemental Analysis Using Multi-parameter Coincidence Spectrometr; GEMINI-II.
Y. Hatsukawa, Y. Miyamoto, Y. Toh, M. Oshima, M. Gharaie, K. Goto and K. Toyota
J. Radioanalytical Nucl. Chem. **272** (2007) pp. 273-276.

17. Determination of As and Sb in Iron and Steel by Neutron Activation Analysis with Multiple Gamma-Ray Detection.
A. Kimura, Y. Toh, M. Oshima, Y. Hatsukawa and J. Goto
J. Radioanalytical Nucl. **271** No. 2 (2007) pp. 323-327.

18. Neutron Scattering Study of $LiNiO_3$.
K. Basar, Xianglian, H. Honda, T. Sakuma, H. Takahashi, O. Abe, N. Igawa and Y. Ishii
Proc. 10th Asian Conference on Solid State Ionics (2006) pp. 121-128.

19. Diffuse X-ray and Neutron Scattering from Powder PbS.
Xianglian, K. Basar, H. Honda, T. Hojo, T. Sakuma, H. Takahashi, N. Igawa and Y. Ishii
Proc. 10th Asian Conference on Solid State Ionics (2006) pp. 185-192.

20. Crystal Structure and Heat Capacity of $Ba_3Ca_{1.18}Nb_{1.82}O_{8.73}$.
T. Shimoyama, J. Sagiya, T. Tojo, H. Kawaji, T. Atake, N. Igawa and Y. Ishii
Proc. 10th Asian Conference on Solid State Ionics (2006) pp. 201-205.

21. Crystal and Magnetic Structures and their Temperature Dependence of Co_2Z-type Hexaferrite $(Ba,Sr)_2Co_2Fe_{24}O_{41}$ by High-temperautre Neutron Diffraction.
Y. Takada, T. Nakagawa, M. Tokunaga, Y. Fukuta, T. Tanaka, T.A. Yamamoto, T. Tachibana, Y. Ishii and N. Igawa
Journal of Applied Physics **100** (2006) pp. 043904-1-043904-7.

22. The Determination of Deuteron Site in $SrZr_{0.95}Sc_{0.05}O_{3-a}$ by Neutron Powder Diffraction.
T. Ito, T. Nagasaki, K. Iwasaki, M. Yoshino, T. Matsui, N. Igawa and Y. Ishii
Solid State Ionics **177** No.26-32 (2006) pp. 2353-2356.

23. Existence of Ferroelectric Ice in the Universe.
H. Fukazawa, A. Hoshikawa, Y. Ishii, B.C. Chakoumakos and J.A. Fernandez-Baca
The Astrophysical Journal **652** (2006) pp. 57-60.

24. Methane Molecular Motion in Clathrate Hydrate Host Framework.
T. Kamiyama, N. Seki, H. Iwasa, T. Uchida, T. Ebinuma, H. Narita, N. Igawa, Y. Ishii, S.M. Bennington and Y. Kiyanagi
Physica B **385-386** (2006) pp. 202-204.

25. Deuteron Ordering in Ice Containing Impurities: A Neutron Diffraction Study.
H. Fukazawa, A. Hoshikawa, H. Yamauchi, Y. Yamaguchi, N. Igawa and Y. Ishii
Physica B **385-386** (2006) pp. 113-115.

26. Location of Deuterium Atoms in $BaSn_{0.5}In_{0.5}O_{2.75+\alpha}$ by Neutron Powder Diffraction at 10 K.
T. Ito, T. Nagasaki, K. Iwasaki, M. Yoshino, T. Matsui, N. Igawa and Y. Ishii
Solid State Ionics **178** No.1-2 (2007) pp. 13-17.

27. Magnetic Structural Characterization of Mg-Co-Cr Ferrite by Neutron Diffraction.
S.M. Yunus, H. Yamauchi, A.K.M. Zakaria, N. Igawa, A. Hoshikawa and Y. Ishii
J. Magn. Magn. Mater. **310** No.2 (2007) pp. 2722-2724.

28. Special Issue: Physics of Ices and a New Frontier of Planetary Science Existence of Ferroelectric Ice in the Universe. -a Neutron Diffraction Study-
H. Fukazawa
Planetary People, The Japanese Society for Planetary Science **16** (2007) pp. 7-12.

29. A New Photoisomerization Process of the 4-Cyanobutyl Group in a Cobaloxime Complex Crystal Observed by Neutron Diffraction.
T. Hosoya, H. Uekusa, Y. Ohashi, T. Ohhara and R. Kuroki
Bull. Chem. Soc. Jpn. **79** (5) (2006) pp. 692-701.

30. Measurements of Small Organic Molecules on the Single Crystal Neutron Diffractometers for Biomolecules at JAERI.
T. Ohhara, K. Kurihara, T. Tamada, I. Tanaka, N. Niimura and R. Kuroki
Physica B, **385-386** (2006) pp. 1049-1051.

31. Crystallization of Porcine Pancreatic Elastase and a Preliminary Neutron Diffraction Experiment.
T. Kinoshita, T. Tamada, K. Imai, K. Kurihara, T. Ohhara, T. Tada and R. Kuroki
Acta Crystallogr. Sect F **63** (2007) pp. 315-317.

32. Effects of High Molecular Weight Component on Crystallization of Polyethylene Under Shear Flow.
Y. Ogino, H. Fukushima, G. Matsuba, N. Takahashi, K. Nishida and T. Kanaya
Polymer **47** (2006) pp. 5669-5677.

33. High-Efficiency Improvement for High Energy Resolution Experimental Mode of DIANA Spectrometer at Materials and Life Science Facility (MLF) of J-PARC.
N. Takahashi, K. Shibata, T.J. Sato and M. Arai
JAEA Research **2006-062** (2006).

34. Crystallization of Isotactic Polypropylene Under Shear Flow Observed in a Wide Spatial Scale.
Y. Ogino, H. Fukushima, N. Takahashi, G. Matsuba, K. Nishida and T. Kanaya
Macromolecules **39** (2006) pp. 7617-7625.

35. Rheo-SANS Study on Gelation of Poly (vinyl alcohol).
N. Takahashi, T. Kanaya, K. Nishida, Y. Takahashi and M. Arai
Physica B **385-386** (2006) pp. 810-813.

36. Dynamic and Static Fluctuations in Polymer Gels Studied by Neutron Spin-Echo.
T. Kanaya, N. Takahashi, K. Nishida, H. Seto, M. Nagao and Y. Takeda
Physica B **385-386** (2006) pp. 676-681.

37. Repetition Rate Multiplication Capability for a High Energy Resolution Mode of DIANA at J-PARC.
N. Takahashi, K. Shibata, T.J. Sato and M. Arai
Journal of Neutron Research **15** (2007) pp. 61-67.

38. Low-Energy Dynamics of Superionic Glass: Evidence for a Direct Relation ewith Ionic Conductivity.
M. Nakamura, M. Arai and E. Kartini
Quasi-Elastic Neutron Scattering Conference 2006, Materials Research Society (2007) pp. 169-176.

39. Utilization of Multiple Incident Energies on Cold-Neutron Disk-Chopper Spectrometer at J-PARC.
M. Nakamura, K. Nakajima, R. Kajimoto and M. Arai
Journal of Neutron Research **15** No.1 (2007) pp. 31-37.

40. Cold-Neutron Disk-Chopper Spectrometer at J-PARC.
K. Nakajima, M. Nakamura, R. Kajimoto, T. Osakabe, K. Kakurai, M. Matsuda, M. Metoki, S. Wakimoto, T.J. Sato, S. Itoh, M. Arai, K. Yoshida and K. Niita
Journal of Neutron Research **15** No.1 (2007) pp. 13-21.

41. Design of Engineering Diffractometer at J-PARC.
S. Harjo, A. Moriai, S. Torii, H. Suzuki, K. Suzuya, Y. Morii, M. Arai, Y. Tomota, K. Akita and Y. Akiniwa
Materials Science Forum **524-525** (2006) pp. 199-204.

42. Report on a 20th Anniversary Symposium on High-Tc Superconductors.
M. Arai, Y. Ando, H. Oyanagi, H. Kamimura, M. Takashige and Y. Maeno
Solid State Physics **41** No.8 (2006) pp. 537-547.

43. Unique Vibrational Excitations in Superionic Conducting Glass.
M. Nakamura, M. Arai, E. Kartini, J.W. Taylor and M. Russina
"Flow Dynamics: The Second Inernational Conference on Flow Dynamics", Eds. M. Tokuyama and S. Maruyama, AIP (2006) pp. 504-507.

44. Relation between High Ionic Conductivity and Boson Peak in Superionic Glass.
M. Arai, H. Iwase, M. Nakamura, T. Otomo, E. Kartini, K. Itoh, S.J. Levett and S.M. Bennington
"Flow Dynamics: The Second Inernational Conference on Flow Dynamics", Eds. M. Tokuyama and S. Maruyama, AIP (2006) pp. 504-507.

45. Introduction to the Neutron Sceince.
Y. Morimoto, Y. Morii, S. Ikeda and M. Arai
J. Cryst. Soc. Jpn. (2006) pp. 1-7.

46. Magnetic and Transport Properties of $Gd_3Ir_4Sn_{13}$ with Unique Crystal Structure.
C. Nagoshi, R. Yamamoto, K. Kuwahara, H. Sagayama, D. Kawana, M. Kohgi, H. Sugawara, Y. Aoki, H. Sato, T. Yokoo and M. Arai
J. Phys. Soc. Jpn. **75** No.4 (2006) p. 044710.

47. Neutron Science in the Materials Life Sciences Facility in J-PARC.
M. Arai
Genshikaku Kenkyu **50** No.5 (2006) pp. 59-67.

48. State-of-the-Art Neutron Instrument Suite for J-PARC
From Basic Science to Industrial Applications.
M. Arai
Gekkan Energy, special issue **1** (2006) pp. 14-19.

49. Prototype of Network Distributed Control System for MLF/J-PARC.
T. Nakatani, K. Nakajima, S. Torii, Bharoto, W. Higemoto, S. Sato, T. Otomo and M. Arai
Physica B **385-386** (2006) pp. 1327-1329.

50. Study of Converging Neutron Guides for the Cold Neutron Double-Chopper Spectrometer at J-PARC.
R. Kajimoto, M. Nakamura, T. Osakabe, T.J. Sato, K. Nakajima and M. Arai
Physica B **385-386** (2006) pp. 1236-1239.

51. Inelastic Scattering Measurement Option of TOF-USANS Instrument at J-PARC.
K. Aizawa and M. Arai
Physica B **385-386** (2006) pp. 1114-1117.

52. Peak Overlapping and Its De-Convolution in TOF Diffraction Data From Neutron Biological Diffractometer in J-PARC.
K. Kusaka, T. Ohhara, I. Tanaka, N. Niimura, T. Ozeki, K. Kurihara, K. Aizawa, Y. Morii, M. Arai, K. Ebata and Y. Takano
Physica B **385-386** (2006) pp. 1062-1065.

53. Development of Engineering Diffractometer at J-PARC.
A. Moriai, S. Torii, H. Suzuki, S. Harjo, Y. Morii, M. Arai, Y. Tomota, T. Suzuki, Y. Akiniwa, H. Kimura and K. Akita
Physica B **385-386** (2006) pp. 1043-1045.

54. IBARAKI Materials Design Diffractometer for J-PARC.
T. Ishigaki, S. Harjo, M. Yonemura, T. Kamaiyama, K. Aizawa, K. Oikawa, T. Sakuma, Y. Morii, M. Arai, K. Ebata, Y. Takano and T. Kasao
Physica B **385-386** (2006) pp. 1022-1024.

55. Low Energy Vibrational Excitations Characteristic of Superionic Glass.
M. Nakamura, H. Iwase, M. Arai, E. Kartini, M. Russina, T. Yokoo and J.W. Taylor
Physica B **385-386** (2006) pp. 552-554.

56. Mobile Cation Motion in Superionic Glasses.
M. Russina, M. Arai, E. Kartini, F. Mezei and M. Nakamura
Physica B **385-386** (2006) pp. 240-242.

57. Structure and Dynamics on Superionic Conducting Phosphate Glasses by Neutron Scattering.
E. Kartini, M. Arai, F. Mezei, M. Nakamura and M. Russina
Physica B **385-386** (2006) pp. 236-239.

58. Dynamics Structure of a Room-Temperature Ionic Liquid bmimCl.
Y. Inamura, O. Yamamura, S. Hayashi and H. Hamaguchi
Physica B **385-360** (2006) p. 732.

59. Fractal Structure and Critical Scattering in the Three-Dimensional Percolating Antiferromagnet, $RbMn_{0.31}Mg_{0.69}F_3$.
S. Itoh, R. Kajimoto, K. Iwasa, N. Aso, M.J. Bull, M.A. Adams, T. Takeuchi and H. Yoshizawa
Physica B **385-386** (2006) pp. 441-443.

60. Fractal Dimension in Percolating Heisenberg Antiferromagnets.
S. Itoh, R. Kajimoto, M.A. Adams, M.J. Bull, K. Iwasa, N. Aso, H. Yoshizawa and T. Takeuchi
J. Magn. Magn. Mater. **310** (2007) pp. 1549-1551.

61. Dynamical Heterogeneity of Protein Dynamics Studied by Elastic Incoherent Neutron Scattering and Molecular Simulations.
H. Nakagawa, A. Tokuhisa, H. Kamikubo, Y. Joti, A. Kitao and M. Kataoka
Mater. Sci. Eng. A **442** (2006) pp. 356-360.

62. Hydration-Coupled Protein Boson Peak Measured by Incoherent Neutron Scattering.
H. Nakagawa, M. Kataoka, Y. Joti, A. Kitao, K. Shibata, A. Tokuhisa, I. Tsukushi and N. Go
Physica B **385-386** (2006) pp. 871-873.

63. Orientational Information of Troponin C Within the Thin Filaments Obtained by Neutron Fiber Diffraction.
S. Fujiwara and F. Matsumoto
J. Mol. Biol. **367** (2007) pp. 16-24.

64. Preparation of Large Crystals of Photoactive Yellow Protein for Neutron Diffraction and High Resolution Crystal Structure Analysis.
S. Yamaguchi, H. Kamikubo, N. Shimizu, Y. Yamazaki, Y. Imamoto and M. Kataoka
Photochem. Photobiol. **83** (2007) pp. 336-338.

65. Search for Magnetic Excitation Spectra of $Na_xCoO_2{\cdot}yD_2O$.
- Neutron scattering -
T. Moyoshi, Y. Yasui, M. Soda, Y. Kobayashi, M. Sato and K. Kakurai
J. Phys. Soc. Jpn **75** (2006) pp. 074705-074710.

66. Successive Magnetic Phase Transitions in α-Tb_2S_3 Studied by Neutron Diffraction Technique.
M. Matsuda, K. Kakurai, S. Ebisu and S. Nagata
J. Phys. Soc. Jpn **75** (2006) pp. 074710-074713.

67. Polarized Neutron Inelastic Scattering Study of the Anisotropic Magnetic Fluctuations in the Quasi-1D Ising-Like Antiferromagnet $TlCoCl_3$.
A. Oosawa, K. Kakurai, Y. Nishiwaki and T. Kato
J. Phys. Soc. Jpn **75** (2006) pp. 074719-074722.

68. Magnetic and Metal-Insulator Transitions in β-$Na_{0.5}CoO_2$ and γ-$K_{0.5}CoO_2$.
- NMR and Neutron Diffraction Studies -
H. Watanabe, Y. Mori, M. Yokoi, T. Moyoshi, M. Soda, Y. Yasui, Y. Kobayashi, M. Sato, N. Igawa and K. Kakurai
J. Phys. Soc. Jpn **75** (2006) pp. 034716-034723.

69. Pressure-Induced Magnetic Quantum Phase Transition in Gapped Spin System $KCuCl_3$.
K. Goto, M. Fujisawa, H. Tanaka, Y. Uwatoko, A. Oosawa, T. Osakabe and K. Kakurai
J. Phys. Soc. Jpn **75** (2006) pp. 064703-064709.

70. Structural Studies of Pyrochlore-Related Spin-1/2 System $Ag_2Cu_2O_3$.
D. Uematsu, M. Soda, Y. Kobayashi, M. Sato, N. Igawa and K. Kakurai
J. Phys. Soc. Jpn **75** (2006) pp. 124601-124604.

71. Replica Symmetry Bresking of the Isin Glass in the Bethe and Cluster Approximations.
T. Yokota
Physics Letters A **363** (2006) pp. 161-170.

72. Structural Transformation on the Pressure-Induced Metal-Insulator Transition in $PrFe_4P_{12}$.
D. Kawana, K. Kuwahara, M. Sato, M. Takagi, Y. Aoki, M. Kohgi, H. Sato, H. Sagayama, T. Osakabe, K. Iwasa and H. Sugawara
J. Phys. Soc. Jpn **75** (2006) pp. 113602-113605.

73. Impurity Effect on the Diagonal Incommensurate Spin Correlations in $La_{2-x}Sr_xCuO_4$.
M. Matsuda, M. Fujita and K. Yamada
Phys. Rev. B **73** (2006) pp. 140503-140506.

74. Magnetic Field-Induced Quasiparticle Excitation in Nb_3Sn: Evidence for Anisotropic S-Wave Pairing.
R. Kadono, K.H. Satoh, A. Koda, T. Nagata, H. Kawano-Furukawa, J. Suzuki, M. Matsuda, K. Ohishi, W. Higemoto, S. Kuroiwa, H. Takagiwa and J. Akimitsu
Phys. Rev. B **74** (2006) pp. 024513-024517.

75. Incommensurate Lattice Distortion in the High Temperature Tetragonal Phase of $La_{2-x}(Sr,Ba)_xCuO_4$.
S. Wakimoto, H. Kimura, M. Fujita, K. Yamada, Y. Noda, G. Shirane, G. Gu, H. Kim and R.J. Birgeneau
J. Phys. Soc. Jpn **75** (2006) pp. 074714-074719.

76. Dielectric Properties and Lattice Dynamics of Ca-doped $K_{0.95}Li_{0.05}TaO_3$.
S. Wakimoto, G.A. Samara, R.K. Grubbs, E.L. Venturini, L.A. Boatner, G. Xu, G. Shirane and S.-H. Lee
Phys. Rev. B **74** (2006) pp. 054101-054112.

77. Neutron and X-ray Scattering Studies of Relaxors.
K. Hirota, S. Wakimoto and David E. Cox
J. Phys. Soc. Jpn **75** (2006) pp. 111006-111018.

78. Study of Converging Guides for the Cold Neutron Double-Chopper Spectrometer at J-PARC.
R. Kajimot, M. Nakamura, T. Osakabe, T.J. Sat, K. Nakajima and M. Arai
Physica B **385-386** (2006) pp. 1236-1239.

79. Pressure-Induced Magnetic Ordering in $KCuCl_3$.
K. Kakurai, T. Osakabe, K. Goto, A. Oosawa, M. Fujisawa and H. Tanaka
Physica B **385-386** (2006) pp. 450-452.

80. Photoemission Study of Excess Oxygen-doped $La_2CuO_{4.10}$.
M. Hashimoto, T. Yoshida, K. Tanaka, A. Fujimori, D.H. Lu, Z.-X. Shen, S. Wakimoto, M. Okusawa and K. Yamada
Physica C **445-448** (2006) pp. 80-81.

81. Magnetic Excitations in the Quasi-1D Ising-like Antiferromagnet $TlCoCl_3$.
A. Oosawa, Y. Nishiwaki, T. Kato and K. Kakurai
J Phys. Soc. Jpn. **75** (2006) pp. 015002-015003.

82. Studies of Anomalous Hall Effect and Magnetic Structure of $Nd_2Mo_2O_7$.
- Test of Chirality Mechanism -
Y. Yasui, T. Kageyama, T. Moyoshi, M. Soda, M. Sato and K. Kakurai
J Phys. Soc. Jpn. **75** (2006) pp. 084711-1-084711-11.

83. Magnetic Structure of $YBaCo_4O_7$ with Kagome- and Triangular-Lattices.
M. Soda, Y. Yasui, M. Taketo, M. Sato, N. Igawa and K. Kakurai
J Phys. Soc. Jpn. **75** (2006) pp. 054707-1-054707-6.

84. Existence of Co^{3+} Low-Spin State in $TbBaCo_2O_{5.5}$.
M. Soda, Y. Yasui, Y. Kobayashi, T. Fujita, M. Sato and K. Kakurai
J. Phys. Soc. Jpn. **75** (2006) pp. 104708-1-104708-7.

85. A Quantum Multi-Critical Point in $CeCu_{6-x}Au_x$.
R.A. Robinson, D.J. Goossens, M.S. Torikachvili, K. Kakurai and H. Okumura
Physica B **385-386** (2006) pp. 38-40.

86. Polarized Neutron Reflectometry as a Non-Destructive Tool for Studies on the Buried Interfaces in Magnetic Thin Films.
M. Takeda
Trans. MRS-J, **32** (2007) pp. 199-202.

87. Replica Symmetry Breaking in the Ising Spin Glass Model on Bethe-like Lattices with Loop.
T. Yokota
Physica A **379** (2007) pp. 534-544.

88. Development of a Hhybrid-Anvil Type High-Pressure Device and Its Application to Magnetic Neutron Scattering Studies.
T. Osakabe, K. Kakurai, D. Kawana and K. Kuwahara
J. Magn. Magn. Mater. **310** (2007) pp. 2725-2727.

89. Spin-Lattice Instability to a Fractional Magnetization State in the Spinel $HgCr_2O_4$.
M. Matsuda, H. Ueda, A. Kikkawa, Y. Tanaka, K. Katsumata, Y. Narumi, T. Inami, Y. Ueda and S.-H. Lee
Nature Physics **3** (2007) pp. 397-400.

90. Magnetic Excitations from the Singlet Dimerized State in $Na_2Co_2(C_2O_4)3(H_2O)_2$.
M. Matsuda, S. Wakimoto, K. Kakurai, Z. Honda and K. Yamada
Phys. Rev. B **75** (2007) pp. 012405-012408.

91. Spiral Spin Structure in a Heisenberg Pyrochlore Magnet $CdCr_2O_4$.
M. Matsuda, M. Takeda, M. Nakamura, K. Kakurai, A. Oosawa, E. Lelièvre-Berna, J.-H. Chung, H. Ueda, H. Takagi and S.-H. Lee
Phys. Rev. B **75** (2007) pp. 104415-104420.

92. Characterization of Multimetric Variants of Ubiquitin Carboxyl-Terminal Hydrolase L1 in Water by Small-Angle Neutron Scattering.
S. Naito, H. Mochizuki, T. Yasuda, Y. Mizuno, M. Furusaka, S. Ikeda, T. Adachi, H.M. Shimizu, J. Suzuki, S. Fujiwara, T. Okada, K. Nishikawa, S. Aoki and K. Wada
Biochemical and Biophysical Research Communications **339** (2006) pp. 717-725.

93. Study on Microstructures of Advanced Metallic Materials by Small-Angle X-Ray and Neutron Scattering.
M. Ohnuma and J. Suzuki
BUNSEKI KAGAKU **55** (2006) pp. 381-390.

94. Quantitative Analysis of Microstructure by Small-Angle Neutron and X-Ray Scattering.
M. Ohnuma and J. Suzuki
Bulletin of The Iron and Steel Institute of Japan, **11** (2006) pp. 631-640.

95. A Magnetic Neutron Lens Based on an Extended Halbach-Type Permanent Sextupole Magnet.
T. Oku, S. Yamada, H. Sasao, J. Suzuki, T. Shinohara, K. Hirota, K. Ikeda, T. Tsuzaki, Y. Kiyanagi, M. Furusaka and H.M. Shimizu
Physica B **385-386** (2006) pp. 1225-1228.

96. Development of Multichannel Parabolic Guide for Thermal Neutron Beam Focusing.
S. Yamada, T. Shinohara, H. Sasao, T. Oku, J. Suzuki, H. Matsue and H.M. Shimizu
Physica B **385-386** (2006) pp. 1243-1246.

97. Thermal Neutron Refraction by Material Prism.
T. Shinohara, K. Hirota, T. Adachi, K. Ikeda, H.M. Shimizu, J. Suzuki and T. Oku
Physica B **385-386** (2006) pp. 1232-1235.

98. Focusing and Polarized Neutron Ultra-Small-Angle Scattering Spectrometer (SANS-J-II) at Research Reactor JRR-3, Japan.
S. Koizumi, H. Iwase, J. Suzuki, T. Oku, R. Motokawa, H. Sasao, H. Tanaka, D. Yamaguchi, H.M. Shimizu and T. Hashimoto
Physica B **385-386** (2006) pp. 1000-1006.

99. Development of Neutron Anger-Camera Detector Based on Flatpanel PMT.
K. Hirota, S. Satoh, K. Sakai, T. Shinohara, K. Ikeda, K. Mishima, S. Yamada, T. Oku, J. Suzuki, M. Furusaka and H.M. Shimizu
Physica B **385-386** (2006) pp. 1297-1299.

100. Development of Measurement System of Neutron b Decay.
K. Mishima, S. Yamada, H. Sato, K. Hirota, T. Shinohara, T. Morishima, J. Suzuki, T. Oku and H.M. Shimizu
Physica B **385-386** (2006) pp. 1219-1221.

101. Simulation Study of Neutron Focusing Effect on a Pulsed Sextupole Magnetic Lens Using PHITS Code.
I. Mitsutake, Y. Kiyanagi, T. Kamiyama, K. Niita, J. Suzuki, T. Oku and H.M. Shimizu
Physica B **385-386** (2006) pp. 1229-1231.

102. A Neutron Scattering Study on Microstructure and Deformation Behavior in Nitrogen Bearing Austenitic Steels.
Y. Tomota, K. Ikeda, M. Ojima, J. Suzuki and T. Kamiyama
Materials Science Forum **539-543** (2007) pp. 234-241.

103. Stress Measurements in Welds: Problem Areas.
T.M. Holden, H. Suzuki, D.G. Carr, M.I. Ripley, D.W. Brown, S.C. Vogel and B. Clausen
Mater. Sci. Eng. A **437** (2006) pp. 33-37.

104. Neutron Diffraction Measurements of Stress in an Austenitic Butt Weld.
H. Suzuki and T. Holden
J. Strain Analysis for Engineering Design **41** (2006) pp. 575-582.

105. Neutron Diffraction Measurement of Thermal Residual Stresses Caused by Solution Treatment for a SUS 304 Stainless Steel Mechanical Part.
M. Matsushima1, X.J. Jin, Y. Shiota, Y. Tomota, H. Suzuki and A. Moriai
Solid State Phenomena **118** (2006) pp. 425-429.

106. Evaluation of Subsurface Distribution of Residual Stress in Austenitic Stainless Steel using Strain Scanning Method.
T. Shobu, H. Konishi, J. Mizuki, K. Suzuki, H. Suzuki, Y. Akiniwa and K. Tanaka
Materials Science Forum **524-525** (2006) pp. 691-696.

107. Residual Stress Evaluation of Ni Based Weld Metal Using Neutron Diffraction Method.
S. Okido, K. Saito and H. Suzuki
Materials Science Forum **524-525** (2006) pp. 697-702.

108. Stress Measurement Near Surface Region by Strain Scanning Method Using Neutron Diffraction.
S. Machiya, Y. Akiniwa, H. Kimura, K. Tanaka, H. Suzuki, A. Moriai and Y. Morii
J. Soc. Mater. Sci. Japan **55** (2006) pp. 654-660.

109. Application of Strain Scanning Method to Stress Measurement of Austenitic Stainless Steel.
T. Shobu, J. Mizuki, K. Suzuki, H. Suzuki, Y. Akiniwa and K. Tanaka
J. Soc. Mater. Sci. Japan **55** (2006) pp. 647-653.

110. Macroscopic Stress Measurements by Neutron Diffraction and the Part Played by the "Stress-free" Reference.
T.M. Holden, H. Suzuki and D.G. Carr
ISIJ Int. **46** (2006) pp. 959-965.

111. Constructuion and Application of T2-3 Thermal Neutron Beam Port in JRR-3.
N. Metoki and K. Kaneko
Hamon **16** (2) (2006) pp. 120-122.

112. Probing the Coulomb Interaction of the Unconventional Superconductor $PuCoGa_5$ by Phonon Spectroscopy.
S. Raymond, P. Piekarz, J.P. Sanchez, J. Serrano, M. Krisch, B. Janousovà, J. Rebizant, N. Metoki, K. Kaneko, P.T. Jochym, A.M. Oles and K. Parlinski
Phys. Rev. Lett. **96** (2006) pp. 237003-1-234003-4.

113. Magnetic Phase Diagram and Change of 5f Electronic Sates in $NpNiGa_5$.
F. Honda, N. Metoki, K. Kaneko, S. Jonen, E. Yamamoto, D. Aoki, Y. Homma, Y. Shiokawa and Y. Onuki
Physica B **378-380** (2006) pp. 1009-1010.

114. Magnetic Structure and Successive Phase Transition in $NpRhGa_5$.
S. Jonen, N. Metoki, K. Kaneko, F. Honda, D. Aoki, Y. Homma, E. Yamamoto, Y. Haga, Y. Shiokawa and Y. Onuki
Physica B **378-380** (2006) pp. 1018-1020.

115. Phonons in $UCoGa_5$.
N. Metoki, K. Kaneko, S. Raymond, J.P. Sanchez, P. Pliekarz, K. Parlinski, A.M. Oles, S. Ikeda, T.D. Matsuda, Y. Haga, Y. Onuki and G.H. Lander
Physica B **378-380** (2006) pp. 1003-1004.

116. Field-Induced Antiferroquadrupolar Order in the Heavy Fermion Superconductor $PrOs_4Sb_{12}$.
K. Kaneko, N. Metoki, T.D. Matsuda, K. Kuwahara, M. Kohgi, R. Shiina, J-M. Mignot, A. Gukasov and N. Bernhoeft
Physica B **378-380** (2006) pp. 189-191.

117. Magnetisation Dynamics in the Normal and Superconducting Phases of UPd_2Al_3 :
I. Surveys in Reciprocal Space Using Neutron.
A. Hiess, N. Bernhoeft, N. Metoki, G.H. Lander, B. Roessli, N.K.Sato, N. Aso, Y. Haga, Y. Koike, T. Komatsubara and Y. Onuki
J. Phys. Condens. Matter **18** (2006) pp. 437-451.

118. Magnetization Dynamics in the Normal and Superconducting Phases of UPd_2Al_3 : II. Inferences on the Nodal Gap Symmetry.
N. Bernhoeft, A. Hiess, N. Metoki, G.H. Lander and B. Roessli
J. Phys. Condens. Matter **18** (2006) pp. 5961-5972.

119. Small-Angle Neutron Scattering.
-Experimental Method to Observe Living State-
S. Koizumi
KOBUNSHI **55** (2006) pp. 161-164.

120. Neutron Scattering Study on $UTGa_5$ and $NpTGa_5$.
N. Metoki
J. Phys. Soc. Jpn. **75** (2006) pp. 24-29.

121. A-Type Antiferromagnetic Ordering and the Transition of the *5f* Electronic State Accompanied by Unusual Moment Reorientation in NpRhGa5.
S. Jonen, N. Metoki, F. Honda, K. Kaneko, E. Yamamoto, Y. Haga, D. Aoki, Y. Homma, Y. Shiokawa and Y. Onuki
J. Phys. Soc. Jpn. **75** (2006) pp. 41-43.

122. Incommensurate Longitudinal SDW State with a Long Periodicity in UCu_2Si_2.
F. Honda, N. Metoki, T.D. Matsuda, Y. Haga and Y. Onuki
J. Phys. Soc. Jpn. **75** (2006) pp. 121-123.

123. Coexistence of Antiferromagnetism and Heavy-Fermion Superconductivity in $CePt_3Si$ Studied by Neutron Scattering.
K. Kaneko, N. Metoki, N. Bernhoeft, T.D. Matsuda, Y. Haga, T. Yasuda, T. Takeuchi, R. Settai and Y. Onuki
J. Phys. Soc. Jpn. **75** (2006) pp. 177-179.

124. Direct Observation of Polymerization-Reaction-Induced Molecular Self-Assembling Process : In-situ and Real-time SANS Measurements During Living Anionic Polymerization of Polysoprene-Block-Polystyrene.
K. Yamauchi, H. Hasegawa, T. Hashimoto, H. Tanaka, R. Motokawa and S. Koizumi
Macromolecules **39** (2006) pp. 4531-4539.

125. Effects of Shear Flow on a Semidilute Polymer Solution under Phase-separation Condition.
T. Hashimoto, M. Toyama and M. Takenaka
Polymer **47** (2006) pp. 7271-7281.

126. Computer Simulation of Reaction-induced Self-assembly of Cellulose Via Enzymatic Polymerization.
T. Kawakatsu, H. Tanaka, S. Koizumi and T. Hashimoto
J. Phys. Condens Matter **18** (2006) pp. S2499-S2512.

127. Self-Assembly of Block Copolymer thin Files Having a Half-Domain-Spacing Thickness : Nonequilibrium Pathways to Achieve Equilibrium Brush Layers Parallel to Substrate.
K. Fukunaga, A.E. Ribbe and T. Hashimoto
Macromolecules **39** (2006) pp. 6171-6179.

128. Chemical Reaction at Specific Sites and Reaction-Induced Self-Assembly as Observed by In Situ and Real Time SANS :
Enzymatic Polymerization to Synthetic Cellulose.
T. Hashimoto, H. Tanaka, S. Koizumi, K. Kurosaki, H. Ohmae and S. Kobayashi
Biomacromolecules **7** (2006) pp. 2479-2482.

129. Incorporation of Metal Nanoparticles into a Double Gyroid Network Texture.
M. Adachi, A. Okumura, E. Sivaniaf and T. Hashimoto
Macromolecules **39** (2006) pp. 7352-7357.

130. Ferroelectricity Induced by Incommensurate-Commensurate Magnetic Phase Transition in Multiferroic $HoMn_2O_5$.
H. Kimura, Y. Kamada, Y. Noda, K. Kaneko, N. Metoki and K. Kohn
J. Phys. Soc. Jpn. **75** (2006) pp. 113701-1-113701-4.

131. Neutron Spectrum from the Renewed Cold Neutron Source in JRR-3 and Expectation for the Future Upgrade Project.
K. Kaneko, N. Metoki, T. Hazawa, K. Nagahori and K. Nakamura
Hamon **16** (3) (2006) pp. 177-178.

132. Neutron Scattering Study of Magnetic Structure and Metamagnetic Transition between Low and High-Moment States of $NpNiGa_5$.
F. Honda, N. Metoki, K. Kaneko, S. Jonen, E. Yamamoto, D. Aoki, Y. Honma, Y. Haga, Y. Shiokawa and Y. Onuki
Phys. Rev. B **74** (2006) pp. 144413-1-144413-12.

133. Neutron Diffraction Study of Magnetic Structure and Successive 5f Electronic Transition in the Itinerant Antiferromagnet $NpRhGa_5$.
S. Jonen, N. Metoki, F. Honda, K. Kaneko, E. Yamamoto, Y. Haga, D. Aoki, Y. Honma, Y. Shiokawa and Y. Onuki
Phys. Rev. B **74** (2006) pp. 144412-1-144412-8.

134. Small-Angle Neutron Scattering Studies of Chemical Reaction and Reaction-Induced Self-Assembly.
H. Tanaka, S. Koizumi, T. Hashimoto, K. Kurosaki, H Omae and S. Kobayashi
Pysica B **385-386** (2006) pp. 814-817.

135. In Situ and Real-Time Small-Angle Neutron Scattering Studies of Living Anionic Polymerization Process and Polymerization-Induced Self-Assembly of Block Copolymers.
H. Tanaka, K. Yamauchi, H. Hasegawa, N. Miyamoto, S. Koizumi and T. Hashimoto
Pysica B **385-386** (2006) pp. 742-744.

136. Aggregation Behavior of Polyisoprene Chain Ends during Living Anionic Polymerization as Investigated by Time-resolved Small-angle Neutron Scattering.
N. Miyamoto, K. Yamauchi, H. Hasegawa, T. Hashimoto and S. Koizumi
Pysica B **385-386** (2006) pp. 752-755.

137. Phase Equilibria and Phase Separation Dynamics in a Polymer Composite Containing a Main-Chain Liquid Crystalline Polymer.
D. Kim, T. Kyu and T. Hashimoto
J. Polym. Sci. **44** (2006) pp. 3621-3630.

138. Three-Dimentional Small-Angle Neutron Scattering on Shear-Induced Phase Saparation in a Dynamically Asymmetric Polymer Mixture.
S. Koizumi and J. Suzuki
J. Appl. Crystallogr. **39** (2006) pp. 878-888.

139. Neutron Scattering Study on the Field-Induced O_{xy}-Type Antiferroquadrupolar Ordering of the Heavy-Fermion Superconductor $PrOs_4Sb_{12}$.
K. Kaneko, N. Metoki, R. Shiina, T.D. Matsuda, M. Kohgi, K. Kuwahara and N. Bernhoeft
Phys. Rev. B **75** (2007) pp. 094408-1-094408-7.

140. Existence of Fcc-Packed Spherical Micelles in Diblock Copolymer Melt.
Y.-Y. Hang, J.-Y. Hsu, H.-L. Chen and T. Hashimoto
Macromolecules **40** (2007) pp. 406-409.

141. Neutron Science and Technology on J-PARC.
Y. Fujii
Thin Solid Films **515** (2007) pp. 5696-5699.

142. Structural Relation between Ywo Ground States of NaV_2O_5 Under High Pressure.
K. Ohwada, Y. Fujii, J. Muraoka, H. Nakao, Y. Murakami, Y. Noda, H. Ohsumi, N. Ikeda, T. Shobu, M. Isoba and Y. Ueda
Phys. Rev. B **76** (2007) pp. 094113-1-094113-10.

143. Structural Investigations of Migration Pathways in Lithium Ion-Conducting $La_{2/3-x}Li_{3x}TiO_3$ Perovskites.
Y. Inaguma, T. Katsumata, M. Itoh, Y. Morii and T. Tsurui
Solid State Ionics **177** (2006) pp. 3037-3044.

144. DNA Deformability and Hydration Studied by Molecular Dynamics Simulation.
Y. Yonetani, H. Kono, S. Fujii, A. Sarai and N. Go
Molecular Simulation **33** (2007) pp. 103-107.

145. Non-Gaussian Behavior of Elastic Inchoherent Neutron Scattering Profile of Protein Studied by Molecular Dynamics Simulation.
A. Tokuhisa, Y. Joti, H. Nakagawa, A. Kitao and M. Kataoka
Phys. Rev. E **75** (2007) p. 041912.

146. Detection of Pockets on Protein Surfaces Using Small and Large Probe Spheres to Find Putative Ligand Binding Sites.
T. Kawabata and N. Go
Proteins **68** (2007) pp. 516-529.

147. Conformational Analysis of the Structure of Ribosome Fit Into Electron Microscopy Density Maps with Normal Mode Analyses and Molecular Dynamics Simulations.
H. Ishida, A. Matsumoto, Y. Tsutsumi and K. Yura
Proceedings of the16th International Microscopy Congress (2006) p. 242.

148. ReadOut: Structure-based Calculation of Direct and Indirect Readout Energies and Specificities for Protein-DNA Recognition.
S. Ahmad, H. Kono, M.J. Arauzo-Bravo and A. Sarai
Nucleic Acids Res. **34** (2006) pp. 124-127.

149. Amino Acid Residue Doublet Propensity in the Protein-RNA Interface and Its Application to RNA Interface Prediction.
O.T. Kim, K. Yura and N. Go
Nucleic Acids Res. **34** (2006) pp. 6450-6460.

This is a blank page

国際単位系（SI）

表１．SI 基本単位

基本量	SI 基本単位	
	名称	記号
長さ	メートル	m
質量	キログラム	kg
時間	秒	s
電流	アンペア	A
熱力学温度	ケルビン	K
物質量	モル	mol
光度	カンデラ	cd

表２．基本単位を用いて表されるSI組立単位の例

組立量	SI 基本単位	
	名称	記号
面積	平方メートル	m^2
体積	立法メートル	m^3
速さ，速度	メートル毎秒	m/s
加速度	メートル毎秒毎秒	m/s^2
波数	毎メートル	m-1
密度（質量密度）	キログラム毎立法メートル	kg/m^3
質量体積（比体積）	立法メートル毎キログラム	m^3/kg
電流密度	アンペア毎平方メートル	A/m^2
磁界の強さ	アンペア毎メートル	A/m
（物質量の）濃度	モル毎立方メートル	mol/m^3
輝度	カンデラ毎平方メートル	cd/m^2
屈折率	（数の）1	1

表５．SI 接頭語

乗数	接頭語	記号	乗数	接頭語	記号
10^{24}	ヨタ	Y	10^{-1}	デシ	d
10^{21}	ゼタ	Z	10^{-2}	センチ	c
10^{18}	エクサ	E	10^{-3}	ミリ	m
10^{15}	ペタ	P	10^{-6}	マイクロ	μ
10^{12}	テラ	T	10^{-9}	ナノ	n
10^{9}	ギガ	G	10^{-12}	ピコ	p
10^{6}	メガ	M	10^{-15}	フェムト	f
10^{3}	キロ	k	10^{-18}	アト	a
10^{2}	ヘクト	h	10^{-21}	ゼプト	z
10^{1}	デカ	da	10^{-24}	ヨクト	y

表３．固有の名称とその独自の記号で表されるSI組立単位

組立量	SI 組立単位			
	名称	記号	他のSI単位による表し方	SI基本単位による表し方
平面角	ラジアン[(a)]	rad		$m \cdot m^{-1}=1$[(b)]
立体角	ステラジアン[(a)]	sr[(c)]		$m^2 \cdot m^{-2}=1$[(b)]
周波数	ヘルツ	Hz		s^{-1}
力	ニュートン	N		$m \cdot kg \cdot s^{-2}$
圧力，応力	パスカル	Pa	N/m^2	$m^{-1} \cdot kg \cdot s^{-2}$
エネルギー，仕事，熱量	ジュール	J	N・m	$m^2 \cdot kg \cdot s^{-2}$
工率，放射束	ワット	W	J/s	$m^2 \cdot kg \cdot s^{-3}$
電荷，電気量	クーロン	C		s・A
電位差（電圧），起電力	ボルト	V	W/A	$m^2 \cdot kg \cdot s^{-3} \cdot A^{-1}$
静電容量	ファラド	F	C/V	$m^{-2} \cdot kg^{-1} \cdot s^4 \cdot A^2$
電気抵抗	オーム	Ω	V/A	$m^2 \cdot kg \cdot s^{-3} \cdot A^{-2}$
コンダクタンス	ジーメンス	S	A/V	$m^{-2} \cdot kg^{-1} \cdot s^3 \cdot A^2$
磁束	ウエーバ	Wb	V・s	$m^2 \cdot kg \cdot s^{-2} \cdot A^{-1}$
磁束密度	テスラ	T	Wb/m^2	$kg \cdot s^{-2} \cdot A^{-1}$
インダクタンス	ヘンリー	H	Wb/A	$m^2 \cdot kg \cdot s^{-2} \cdot A^{-2}$
セルシウス温度	セルシウス度[(d)]	℃		K
光束	ルーメン	lm	cd・sr[(c)]	$m^2 \cdot m^{-2} \cdot cd=cd$
照度	ルクス	lx	lm/m^2	$m^2 \cdot m^{-4} \cdot cd=m^{-2} \cdot cd$
（放射性核種の）放射能	ベクレル	Bq		s^{-1}
吸収線量，質量エネルギー分与，カーマ	グレイ	Gy	J/kg	$m^2 \cdot s^{-2}$
線量当量，周辺線量当量，方向性線量当量，個人線量当量，組織線量当量	シーベルト	Sv	J/kg	$m^2 \cdot s^{-2}$

(a)ラジアン及びステラジアンの使用は、同じ次元であっても異なった性質をもった量を区別するときの組立単位の表し方として利点がある。組立単位を形作るときのいくつかの用例は表４に示されている。
(b)実際には、使用する時には記号rad及びsrが用いられるが、習慣として組立単位としての記号“１”は明示されない。
(c)測光学では、ステラジアンの名称と記号srを単位の表し方の中にそのまま維持している。
(d)この単位は、例としてミリセルシウス度m℃のようにSI接頭語を伴って用いても良い。

表４．単位の中に固有の名称とその独自の記号を含むSI組立単位の例

組立量	SI 組立単位		
	名称	記号	SI 基本単位による表し方
粘度	パスカル秒	Pa・s	$m^{-1} \cdot kg \cdot s^{-1}$
力のモーメント	ニュートンメートル	N・m	$m^2 \cdot kg \cdot s^{-2}$
表面張力	ニュートン毎メートル	N/m	$kg \cdot s^{-2}$
角速度	ラジアン毎秒	rad/s	$m \cdot m^{-1} \cdot s^{-1}=s^{-1}$
角加速度	ラジアン毎平方秒	rad/s^2	$m \cdot m^{-1} \cdot s^{-2}=s^{-2}$
熱流密度，放射照度	ワット毎平方メートル	W/m^2	$kg \cdot s^{-3}$
熱容量，エントロピー	ジュール毎ケルビン	J/K	$m^2 \cdot kg \cdot s^{-2} \cdot K^{-1}$
質量熱容量（比熱容量），質量エントロピー	ジュール毎キログラム毎ケルビン	J/(kg・K)	$m^2 \cdot s^{-2} \cdot K^{-1}$
質量エネルギー（比エネルギー）	ジュール毎キログラム	J/kg	$m^2 \cdot s^{-2} \cdot K^{-1}$
熱伝導率	ワット毎メートル毎ケルビン	W/(m・K)	$m \cdot kg \cdot s^{-3} \cdot K^{-1}$
体積エネルギー	ジュール毎立方メートル	J/m^3	$m^{-1} \cdot kg \cdot s^{-2}$
電界の強さ	ボルト毎メートル	V/m	$m \cdot kg \cdot s^{-3} \cdot A^{-1}$
体積電荷	クーロン毎立方メートル	C/m^3	$m^{-3} \cdot s \cdot A$
電気変位	クーロン毎平方メートル	C/m^2	$m^{-2} \cdot s \cdot A$
誘電率	ファラド毎メートル	F/m	$m^{-3} \cdot kg^{-1} \cdot s^4 \cdot A^2$
透磁率	ヘンリー毎メートル	H/m	$m \cdot kg \cdot s^{-2} \cdot A^{-2}$
モルエネルギー	ジュール毎モル	J/mol	$m^2 \cdot kg \cdot s^{-2} \cdot mol^{-1}$
モルエントロピー，モル熱容量	ジュール毎モル毎ケルビン	J/(mol・K)	$m^2 \cdot kg \cdot s^{-2} \cdot K^{-1} \cdot mol^{-1}$
照射線量（Ｘ線及びγ線）	クーロン毎キログラム	C/kg	$kg^{-1} \cdot s \cdot A$
吸収線量率	グレイ毎秒	Gy/s	$m^2 \cdot s^{-3}$
放射強度	ワット毎ステラジアン	W/sr	$m^4 \cdot m^{-2} \cdot kg \cdot s^{-3}=m^2 \cdot kg \cdot s^{-3}$
放射輝度	ワット毎平方メートル毎ステラジアン	$W/(m^2 \cdot sr)$	$m^2 \cdot m^{-2} \cdot kg \cdot s^{-3}=kg \cdot s^{-3}$

表６．国際単位系と併用されるが国際単位系に属さない単位

名称	記号	SI 単位による値
分	min	1 min=60s
時	h	1h =60 min=3600 s
日	d	1 d=24 h=86400 s
度	°	1° =(π/180) rad
分	’	1’ =(1/60)° =(π/10800) rad
秒	”	1” =(1/60)’ =(π/648000) rad
リットル	l、L	$1l=1\ dm^3=10^{-3}m^3$
トン	t	$1t=10^3$ kg
ネーパ	Np	1Np=1
ベル	B	1B=(1/2)ln10(Np)

表７．国際単位系と併用されこれに属さない単位でSI単位で表される数値が実験的に得られるもの

名称	記号	SI 単位であらわされる数値
電子ボルト	eV	$1eV=1.60217733(49)\times10^{-19}J$
統一原子質量単位	u	$1u=1.6605402(10)\times10^{-27}kg$
天文単位	ua	$1ua=1.49597870691(30)\times10^{11}m$

表８．国際単位系に属さないが国際単位系と併用されるその他の単位

名称	記号	SI 単位であらわされる数値
海里		1海里=1852m
ノット		1ノット=1海里毎時=(1852/3600)m/s
アール	a	$1a=1\ dam^2=10^2m^2$
ヘクタール	ha	$1ha=1\ hm^2=10^4m^2$
バール	bar	$1bar=0.1MPa=100kPa=1000hPa=10^5Pa$
オングストローム	Å	$1Å=0.1nm=10^{-10}m$
バーン	b	$1b=100fm^2=10^{-28}m^2$

表９．固有の名称を含むCGS組立単位

名称	記号	SI 単位であらわされる数値
エルグ	erg	$1\ erg=10^{-7}\ J$
ダイン	dyn	$1\ dyn=10^{-5}N$
ポアズ	P	$1\ P=1\ dyn \cdot s/cm^2=0.1Pa \cdot s$
ストークス	St	$1\ St=1cm^2/s=10^{-4}m^2/s$
ガウス	G	$1\ G\ \hat{}\ 10^{-4}T$
エルステッド	Oe	$1\ Oe\ \hat{}\ (1000/4\pi)A/m$
マクスウェル	Mx	$1\ Mx\ \hat{}\ 10^{-8}Wb$
スチルブ	sb	$1\ sb=1cd/cm^2=10^4cd/m^2$
ホト	ph	$1\ ph=10^4lx$
ガル	Gal	$1\ Gal=1cm/s^2=10^{-2}m/s^2$

表10．国際単位に属さないその他の単位の例

名称	記号	SI 単位であらわされる数値
キュリー	Ci	$1\ Ci=3.7\times10^{10}Bq$
レントゲン	R	$1\ R=2.58\times10^{-4}C/kg$
ラド	rad	$1\ rad=1cGy=10^{-2}Gy$
レム	rem	$1\ rem=1\ cSv=10^{-2}Sv$
X線単位		$1X\ unit=1.002\times10^{-4}nm$
ガンマ	γ	$1\gamma=1\ nT=10^{-9}T$
ジャンスキー	Jy	$1\ Jy=10^{-26}W \cdot m^{-2} \cdot Hz^{-1}$
フェルミ		$1\ fermi=1\ fm=10^{-15}m$
メートル系カラット		$1\ metric\ carat=200\ mg=2\times10^{-4}kg$
トル	Torr	1 Torr = (101 325/760) Pa
標準大気圧	atm	1 atm = 101 325 Pa
カロリー	cal	
ミクロン	μ	$1\ \mu=1\mu m=10^{-6}m$

（第７版，1998年改訂）

この印刷物は再生紙を使用しています